CORA Cork Open Research Archive
Cartlann Taighde Oscailte Chorcaí

Title	Advancement of software in the loop system for current simulation in wave tanks
Authors	Frawley, Cillian
Publication date	2024
Original Citation	Frawley, C. 2024. Advancement of software in the loop system for current simulation in wave tanks. MRes Thesis, University College Cork.
Type of publication	Masters thesis (Research)
Rights	© 2024, Cillian Frawley. - https://creativecommons.org/licenses/by-nc-nd/4.0/
Download date	2026-11-08 15:10:25
Item downloaded from	https://hdl.handle.net/10468/17471



UCC
University College Cork, Ireland
Coláiste na hOllscoile Corcaigh



Advancement of software in the loop system for current simulation in wave tanks

Thesis presented by:

Cillian Frawley

for the degree of:

Masters by Research

University College Cork

Engineering

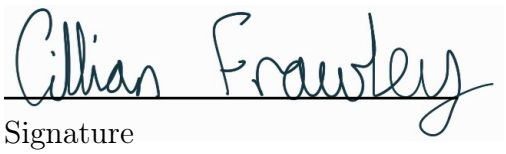
Head of School/Department: Dr Jorge Oliveira

Supervisor(s): Dr. Jimmy Murphy, Dr. Milad Zabihi Kooykheily, Dr. Mahdi Ebrahimi Salari

2024

Declaration

This is to certify that the work I am submitting is my own and has not been submitted for another degree, either at University College Cork or elsewhere. All external references and sources are clearly acknowledged and identified within the contents. I have read and understood the regulations of University College Cork concerning plagiarism and intellectual property.



Signature

27/6/2024

Date

Abstract

Model testing in wave tanks is a valuable asset in the preliminary design phase of offshore floating wind turbines. Challenges arise when applying combined wind, wave and current loads in a single test location due to the differing scaling laws of air and water. Hybrid testing overcomes this issue by substituting one working fluid with a real-time numerical simulation using mechanical actuators.

In hybrid testing in wave tanks, simulation of wind loads can be achieved using actuators such as cable winches or fans. Simulation of current loading is often overlooked. This thesis advances the Software-in-the-Loop (SIL) system for current simulation in wave tanks, building on the foundational work by Otter (2022). A comparison between tow testing and physical current testing to determine the hydrodynamic drag coefficient was conducted for both the 1/50 scale model of the INNWIND semi-submersible and the 1/30 scale model of the OE Buoy wave energy device. A broad scope of waves and current loads were tested to evaluate the SIL system for the INNWIND model.

A winch actuator simulates current loading on a semi-submersible floating wind platform, through real-time simulations, applying drag forces derived from Morison's equation. The winch actuation is determined by tension signals from a load cell, with motion-tracking cameras enabling dynamic adjustments based on platform velocity. Wave spectra are adjusted to account for wave-current interactions.

Though a dual-winch system was planned to simulate various current angles, only single-winch actuation was achieved due to time and logistical constraints. The design of the control system and layout for the dual-winch are presented.

Numerical simulations of the moored semi-submersible model in the Deep Ocean Basin (DOB) at the Lir National Ocean Test Facility (NOTF) were conducted in Ansys AQWA to validate the SIL system.

The winch control accurately responded to the demanded drag force across tested environmental loads. For current-only tests, a coefficient of variation (CV) difference between demanded and measured tensions was less than 0.15, with this difference reducing at higher current velocities. Average demanded and measured tensions are within 0.5 % of each other for all velocities. For wave and current tests, the CV of the demanded tension increases significantly due to the wave load, however, the difference in CV between the demanded and measured tension remains less than 0.15 which signifies the Qualisys-SIL (QSIL) system's ability to react dynamically to the environmental loads exerted on the platform in real-time.

Acknowledgements

I would like to thank my supervisor Dr. Jimmy Murphy for his shared expertise and aid throughout the project.

I am grateful for the guidance of Dr. Milad Zabihi Kooykheily for his input on the project surrounding tank testing, wave theory and FOWT dynamics.

I would also like to thank Dr. Mahdi Ebrahaimi Salari for his contributions to the LabVIEW code, dSPACE setup and winch design.

Thanks to Thomas Walsh for his aid with the test setups in the wave tanks and troubleshooting.

Thanks also to Ian Power for helping with software licensing and facilities requirements during my time in Ringaskiddy.

I would like to thank my family and friends for providing encouragement and support throughout my master's.

Finally, I'd like to thank my partner Eve for the unwavering kindness and support that she offers me every day.

Contents

Abstract i

Acknowledgements ii

Contents iii

Nomenclature v

List of figures viii

List of tables ix

Chapter 1 - Introduction 1
1.1 Objectives . . . 3

Chapter 2 - Literature Review 4
2.1 Floating Wind Turbine Technology . . . 4
2.2 Environmental Conditions . . . 5
2.2.1 Wind . . . 5
2.2.2 Waves . . . 7
2.2.3 Current . . . 8
2.2.4 Wave-Current Interactions . . . 9
2.3 Modelling of FOWTs . . . 11
2.3.1 Numerical Modelling . . . 11
2.3.2 Physical Modelling . . . 14
2.3.3 Hybrid Modelling . . . 15
2.4 Process Control . . . 20
2.5 Mooring Systems . . . 22
2.5.1 Overview of Mooring Systems . . . 22
2.5.2 Numerical Modelling of Mooring Systems . . . 25
2.5.3 Physical Modelling of Mooring Systems . . . 26

Chapter 3 - Test Setup 27
3.1 Lir National Ocean Test Facility . . . 27
3.2 Description of the INNWIND Semi-submersible Model . . . 27
3.3 SIL Test Setup . . . 28
3.3.1 SIL - Mooring Design . . . 29
3.3.2 SIL - Emulation of Current Loads . . . 29
3.3.3 SIL - Process Control Design . . . 30
3.3.4 SIL - Hardware Layout for Single- and Dual-Winch Systems . . . 32
3.4 Ansys AQWA Simulation Setup . . . 33
3.5 Test Plan . . . 36

Chapter 4 - Methodology **38**
4.1 Hydrodynamic Coefficient Test Methodology 38
4.2 SIL Testing Methodology 40
4.2.1 Spring Calibration 40
4.2.2 Decay Test 41
4.2.3 Response Amplitude Operator (RAO) Testing 42
4.2.4 Wave-Current Interaction Procedure 42
4.2.5 SIL Testing Procedure 43
4.2.6 Proposed Dual-Winch System Simulink Tuning Methodology 43
4.3 Assumptions, Simplifications and Sources of Error 44

Chapter 5 - Results & Discussion **46**
5.1 Hydrodynamic Coefficient Testing - DOB 46
5.2 Hydrodynamic Coefficient Testing - WCF 50
5.3 Decay Test Response 51
5.4 RAO Results 53
5.5 SIL - Current-Only Results 58
5.6 SIL - Wave and Current Results 62

Chapter 6 - Conclusions & Recommendations **70**
6.1 Conclusions 70
6.2 Recommendations For Future Work 71

References **72**

Appendices **78**

A MATLAB Code **78**

B LabVIEW Code **82**

Nomenclature

Vector Quantities

$\mathbf{C}$	Wave celerity	m/s
CFC	Current Force Coefficient	$\mathrm{N/(m/s)^2}$
$\mathbf{F_D}$	Drag Force	N
$\mathbf{U}$	Current velocity	m/s
$\mathbf{u}$	Platform velocity	m/s

Roman Symbols

A	Wave amplitude	m
CV	Coefficient of Variation	-
f_n	Natural period	Hz
H	Wave height	m
H_s	Significant wave height	m
h	Water depth	m
K_i	Integral gain	-
K_p	Proportional gain	-
k	Wave number	-
T_i	Integral time	s
T_p	Peak wave period	s
T_n	Natural period	s
T_o	Oscillating wave period	s

Greek Symbols

δ	Logarithmic decrement	-
γ	Peak Enhancement Factor	-
ζ	Damping ratio	-
λ	Wavelength	m
λ_L	Scale ratio	-
ρ	Fluid density	$\mathrm{kg/m^3}$
ω	Frequency	rad/s
ω_n	Natural frequency	rad/s

Dimensionless Numbers

Re	Reynolds Number	$\frac{\rho U c}{\mu}$
Fr	Froude Number	$\frac{U}{\sqrt{gL}}$

Acronyms

BEM	Blade Element Momentum
CDPM	Cable Driven Parallel Manipulators
CFD	Computational Fluid Dynamics
COG	Centre Of Gravity
DOB	Deep Ocean Basin
DOF	Degree Of Freedom
FEM	Finite Element Method
FOWT	Floating Offshore Wind Turbine
GM	Metacentric Height
HAWT	Horizontal Axis Wind Turbine
JONSWAP	Joint North Sea Wave Project
KG	COG above Keel
LCOE	Levelised Cost Of Energy
ME	Morison Equation
MIMO	Multiple Input Multiple Output
ML	Mooring Line
MPA	Multi-Propeller Actuator
NOTF	National Ocean Test Facility
NREL	National Renewable Energy Laboratory
PF	Potential Flow
PI	Proportional Integral
PID	Proportional Integral Derivative
QSIL	Qualisys Software in the Loop
QTF	Quadratic Transfer Function
RAO	Response Amplitude Operator
SIL	Software in the Loop
SISO	Single Input Single Output
SWL	Still Water Level
TI	Turbulence Intensity
TSIL	Tension Software in the Loop
TLP	Tension Leg Platform
WCF	Wave Current Flume

List of Figures

1.1 New and Total installations in offshore wind in 2022 (IRENA and GWEC, 2023). 1
2.2 Primary FOWT platform types (Shafiee, 2023). 4
2.3 Secondary platform designs 5
2.4 Vertical profile for a range of α (Atcheson et al., 2016). 6
2.5 Energy density spectrum from a wave record analysis (Journée and Massie, 2001). 8
2.6 Impact of wave-current interactions on wave height. H_0 refers to wave height values obtained without the presence of current (Draycott et al., 2018). . . . 10
2.7 Impact of wave-current interactions on spectral density (Draycott et al., 2018). 10
2.8 Models utilised during stages of FOWT production (Subbulakshmi et al., 2022). 12
2.9 HIL setup for the Politecnico Wind Tunnel with a 6-DOF HexaFloat (Bayati et al., 2018). 16
2.10 ReaTHM system mounted to INO WINDMOOR semi-submersible, adapted from (Berthelsen et al., 2022). 17
2.11 Single winch actuator in the WCF (Otter, 2022). 18
2.12 Winch actuation accuracy in still water (Otter, 2022). 19
2.13 Physical vs. SIL current in the WCF (Otter, 2022). 19
2.14 Block diagram of a MIMO system (Seborg et al., 2016). 21
2.15 Block diagram of a MIMO system with decoupling controllers (Seborg et al., 2016). 21
2.16 Decoupler effect on bulb process interactions (Ahmed et al., 2011). 22
2.17 (a) Catenary (b) Multi-catenary (c) Taut (d) Buoyant semi-taut, mooring systems (BVG Associates, 2023). 23
2.18 Anchor styles for general FOWT applications (Vryhof, 2015). 24
2.19 Range of components commonly connected to a mooring line (BVG Associates, 2023). 25
2.20 Truncated mooring system (Ma et al., 2019). 26
3.21 INNWIND Model Schematic adapted from (Sandner et al., 2015). 27
3.22 Moored INNWIND model in the DOB. 28
3.23 Hardware control layout of the current only system, adapted from Otter (2022). 30
3.24 Single winch, current-only Simulink model. 30
3.25 ControlDesk layout of the single winch system. 31
3.26 Double winch, current-only Simulink model. 32
3.27 W1 at the edge of the DOB. Note that P1 lower is submerged. 33
3.28 Schematic of the dual-winch system in the DOB. 33
3.29 Mesh of the INNWIND semi-submersible model in AQWA. 34
3.30 Model in the DOB basin with mooring lines, attachment points and wave probe location visible. 35
4.31 (a) INNWINDEU semi-sub in the DOB with tow rope attached at COG. (b) Instrument bridge with towrope attached, Futek 445 N Load cell (inset). . . 39
4.32 OE Buoy in the WCF with rope and load cell attached. 40
4.33 Force - displacement graphs of both Mooring (a) and Winch (b) springs. . . 41

5.34 C_d from DOB tow testing for (a) Semi-sub (b) OE Buoy 46
5.35 Comparison of Instrument Bridge and Qualisys surge velocities. 48
5.36 Qualisys roll, pitch and yaw results for the OE Buoy in the DOB. 49
5.37 WCF current velocity method comparison. 50
5.38 C_d from WCF resistance testing for (a) Semi-sub using Otter (2022) VCT results (b) OE Buoy. 50
5.39 Comparison between the WCF and DOB for the INNWINDEU semi-sub. . . 51
5.40 Experimental decay response using Qualisys (a) Surge (b) Sway (c) Heave (d) Roll (e) Pitch (f) Yaw. 52
5.41 RAO1 - RAO7 response for (a) Surge (b) Heave (c) Roll and (d) Pitch 54
5.42 Wave Elevation PSD comparison between AQWA, Experimental and Theory for JONSWAP1. 55
5.43 Spectral energy comparison between AQWA and Experimental JONSWAP2 for a range of H_s. 56
5.44 Wave PSD response to alteration of γ. 57
5.45 Spectral energy comparison between AQWA and Experimental JONSWAP2 for a range of γ. 57
5.46 Tension response to current D, simulated with winch 1 using torque control mode. 58
5.47 (a) Tension and (b) Torque response to current D, simulated with winch 1 using tension control mode. 59
5.48 (a) Tension and (b) Torque response to current D, highlighting time delay in the system. 59
5.49 (a) Tension and (b) Torque response for Test C1. 60
5.50 (a) Tension and (b) Torque response for Test C4. 60
5.51 (a) Current A and (b) Current D PI reaction. 61
5.52 (a) Current A and (b) Current D winch response to the mooring. 61
5.53 Comparison of Experimental and AQWA surge motion (a) C1 (b) C2 (c) C3 (d) C4. 62
5.54 PSD of altered and original JONSWAP1 spectra. 63
5.55 PSD of altered and original JONSWAP2 spectra. 64
5.56 Spectral energy comparison between AQWA and Experimental JONSWAP1 with QSIL. 65
5.57 Comparison between TSIL and QSIL for JONSWAP1 and Current C. 66
5.58 Comparison between TSIL and QSIL for JONSWAP2 and Currents A and C. 67
5.59 Winch tension comparison for QSIL. 69
5.60 Mooring Line 1 tension comparison. 69

B.1 GUI for the LabVIEW code. 82
B.2 LabVIEW code for TSIL single winch system. 83

List of Tables

2.6 Summary of software and methods used for the analysis of FOWTs (Otter et al., 2022b). . . . 12
2.7 Literature review of propeller actuators for FOWT testing. . . . 20
2.8 PID behaviour, adapted from (Li et al., 2006) . . . 22
3.9 Description of the INNWIND Semi-submersible Model, updated from Otter (2022). . . . 28
3.10 Specifications of the servo-drive systems (Schneider Electric, 2022). . . . 29
3.11 Two-winch system layout configurations. . . . 32
3.12 Hydrostatic results of the INNWIND model in AQWA . . . 35
3.13 Summary of primary environmental loads used during testing. . . . 36
3.14 Wave Conditions used in the RAO tests. T_p is the wave period, H_s is the significant wave height and γ is the peak enhancement factor. . . . 36
3.15 Current-only testing in the DOB. . . . 36
3.16 Wave and Current testing in the DOB. Note adapted JONSWAP waves used to account for wave-current interactions. . . . 37
4.17 Spring displacement test results for mooring springs. . . . 41
5.18 DOB repeatability tests of semi-sub. . . . 47
5.19 DOB repeatability tests of OE Buoy. . . . 47
5.20 Comparison of Instrument Bridge and Qualisys average surge velocities. . . . 47
5.21 Qualisys average roll, pitch and yaw results for the OE Buoy in the DOB. . . . 49
5.22 Maximum disturbances of coupled motions for each DOF test. Values in **bold** signify the initial disturbance for each test. . . . 53
5.23 Natural period results compared with Otter (2022) and AQWA. . . . 53
5.24 Tests C1 - C4. . . . 60
5.25 Altered JONSWAP spectra for the presence of current, subscript I indicates the presence of current. . . . 63
5.26 Coefficient of Variation (CV) of demanded and measured tension for TSIL v QSIL. . . . 68

Chapter 1 - Introduction

Offshore renewable energy generation is a crucial aid in meeting global carbon emissions targets. In 2020, the European Commission proposed a reduction of greenhouse gases by 55% compared with the values of 1990, by 2030 (European Commission, 2020). Energy Institute (2023) reported the primary energy consumption in 2022 increased by 1%. Other findings included a 1% growth of renewables' share of primary energy consumption to 7.5% and a steady fossil fuel share of 82%. Despite the increase in renewables' share, the increase in global primary energy consumption requires fossil fuel production to remain high to ensure energy security. To enable a reduction in fossil fuel market shares, an accelerated renewable energy deployment is required over the coming years.

Currently, offshore wind energy production in the EU is 12GW, while ocean energy devices are still in the demonstration and testing phases. The European Commission predicts an installed capacity of 60GW offshore wind energy and 1GW ocean energy by 2030, accelerating to 300GW and 40GW respectively, by 2050 (European Commission, 2020). IRENA and GWEC (2023) reported that in 2022, an additional 8.8GW of offshore wind energy was connected to the grid, bringing the cumulative global capacity to 64.3GW in 2022. Figure 2.2 highlights the dominant market share by China and the EU in new installations and cumulative offshore wind energy capacity as of 2022. Feed-in-tariffs in China, along with global attempts to reduce dependency on Russian fossil fuels amid the Russia-Ukraine war, have led to increased development of renewable energies in recent years.

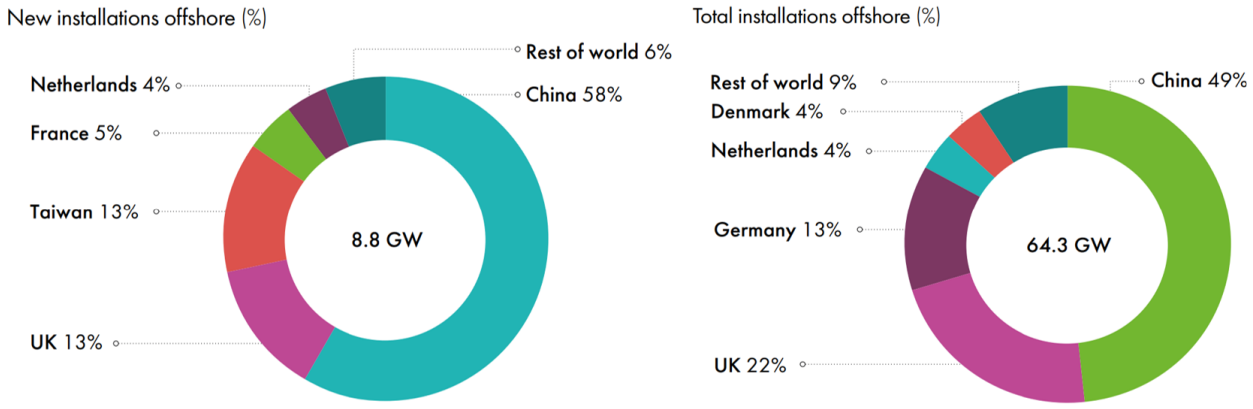


Figure 1.1: New and Total installations in offshore wind in 2022 (IRENA and GWEC, 2023).

Offshore wind installations date back to the 1990s, when a 220kW turbine positioned on a tripod structure was located in 6m of water in Sweden (Esteban et al., 2011). Since then, offshore wind installations have progressed, and the first floating offshore wind farm was connected to the grid in Scotland in 2017. Hywind Scotland demonstrated an average capacity factor of 54% compared to a UK average onshore wind farm capacity of 40% (Offshorewind.biz, 2021). Subsequently, three more floating offshore wind farms have been commissioned and connected to the grid, WindFloat Atlantic (2020, 25MW, Portugal), Kincardine (2021, 50MW, Scotland), and Hywind Tampen (2023, 88MW, Norway). Hywind Tampen is located 140km offshore, in depths of up to 300m and was installed to directly supply electricity to oil and gas field operational facilities at sea (CNBC, 2023).

Wind farms are located offshore due to the higher wind speeds, less physical interference of the wind due to land-based objects, and the efficiency benefits associated with larger

turbine blades. The energy capture capability of Horizontal Axis Wind Turbines (HAWT) is related to the swept area of the rotors. This area obeys a power law, where an increase in the blade radius enables an exponential energy capture, per turbine (Burton et al., 2011). The tower, nacelle, platform and sub-sea systems can remain relatively unchanged compared to shorter-bladed turbines, utilising the existing technologies from onshore turbines. Floating platforms offer the potential to locate turbines in deep waters, where large fixed-bottom foundations are impractical to manufacture and install, in addition to shallow waters with unsuitable seabed geology for monopiles. Floating platforms enable a standardised approach to platform design, where seabed geology is of importance for the mooring line anchors only (Henderson et al., 2016).

The estimated investment required to reach EU's 2030 offshore wind energy targets is €800 billion (JRC, 2020). Between 2010 and 2021, the Levelised Cost of Electricity (LCOE) for offshore wind decreased by 67%, with 2022 showing a further 8% decrease on 2020 figures (IRENA, 2022). While the Floating Offshore Wind Turbine (FOWT) industry has benefited from the research in the oil and gas industry, the aerodynamic loading experienced by FOWTs is often larger than risers and oil rigs. Similarly, ocean energy devices have a reduced above-water footprint, reducing their susceptibility to intense aerodynamic loading. FOWTs are ideal for studying the coupling between aerodynamic and hydrodynamic loading, and the subsequent response of the platform and its mooring lines (Otter, 2022). To reduce the LCOE further, testing of FOWTs is ongoing in laboratories to maximise the efficiency of the system. A mix of physical testing of scale models, numerical simulations and hybrid testing are being utilised to further these developments. For physical testing, wind, wave and current loading are often generated in wave tank facilities with wind generators.

Hybrid testing is an approach that combines physically generated loads with loads predicted by numerical simulations, in real time. Testing of FOWTs poses challenges when applying both aerodynamic and hydrodynamic loading in a laboratory setting. While combined wind, wave and current tanks exist (Atlar, 2011), most laboratories consist of a wave basin/flume with wind generators, or a wind tunnel with a platform rig to simulate hydrodynamic loads and platform response to aerodynamic forces. With a focus on wave basins, it is difficult to generate accurate wind and current at the correct scale and with accurate repeatability. Techniques to substitute the physical wind and current generation have been investigated at the Lir National Ocean Test Facility (NOTF) in recent years, to simplify and reduce costs of laboratory testing (Otter et al., 2020, Otter et al., 2022a).

The focus of this thesis is the advancement of current simulation in wave tanks using a Software-in-the-Loop (SIL) approach. While Otter (2022) combined current generation by use of a dynamic winch, with a Multi Propeller Actuator (MPA) to generate aerodynamic loads, this thesis focuses solely on the current generation aspect of the system. The physical experiments for this study have been carried out in the wave-current flume (WCF) and deep ocean basin (DOB) at the Lir NOTF, Cork, Ireland.

1.1 Objectives

1. Evaluate the hydrodynamic drag coefficient of the INNWIND semi-submersible FOWT platform and OE Buoy wave energy device through resistance tests in the wave-current flume and deep ocean basin. The coefficient is required for the actuation of the winch with the SIL system.

2. Finalise the development of the single winch system for various wave and current conditions.

3. Design a proposed SIL control system and layout for two winches to enable a broader range of platform testing.

This thesis is organized into six chapters, each addressing a specific aspect of the research on floating offshore wind turbines (FOWTs) and their testing methodologies. Chapter 1 provides an introduction to the topic of floating offshore wind turbines. It outlines the motivation behind the research, the significance of the study, and the primary objectives that the thesis aims to achieve. Chapter 2 is the Literature Review, discussing floating wind turbine technology, environmental conditions, modelling of FOWTs, process control and mooring system design. Chapter 3 details the Test Setup, with a description of the INNWIND Semi-submersible Model, procedures for Software-in-the-Loop (SIL) testing of the INNWIND model, numerical simulation setup and environmental loads used. Chapter 4 outlines the Methodology for hydrodynamic coefficient, spring calibration, RAO, decay and wave and current testing. It also includes the assumptions, simplifications and sources of error for the project. Chapter 5 displays and discusses the results while conclusions and recommendations for future work are outlined in Chapter 6.

Chapter 2 - Literature Review

2.1 Floating Wind Turbine Technology

Offshore wind energy technologies have advanced from traditional fixed-bottom turbine structures to floating platforms. Fixed-bottom turbines consist of a monopile, drilled into the seabed for positioning and stability. As well as being difficult to manoeuvre and install, the costs of manufacturing these monopiles for deep waters are uneconomic and therefore FOWTs have been designed to enable wind energy extraction from deep water locations. Locating FOWTs in deep offshore water enables greater energy capture in open seas with stronger winds due to the lack of obstacles and land masses. The vast areas enable the use of 'super-sized' turbines. Since the theoretical power generation of a wind turbine is proportional to its blade length squared, doubling the blade length could see power increase by a factor of four (Manwell et al., 2009). In June 2023, Chinese company Goldwind successfully installed the world's largest wind turbine, the GWH252-16MW fixed-bottom turbine, consisting of blades 123m long (Goldwind, 2023). WindFloat has displayed the potential for FOWT, with the installation of three 8.4MW Vestas V164 turbines mounted on semi-submersible platforms at the WindFloat Atlantic wind farm off the coast of Portugal (WindFloat, 2023).

Floating wind turbine platforms can be primarily categorized into 3 types: Spar, Semi-submersible and Tension Leg Platform (TLP) (Atcheson et al., 2016). Semi-spar (Figure 2.3a) and barge platforms (Figure 2.3b) are also used however are not primary designs. Spar platforms are ballast stabilised, through the use of a slender structure. These are towed horizontally to their installation location before being raised vertically using cranes. These are favoured for their low platform cost and stability in the event of mooring line failure. Semi-submersibles are buoyancy stabilised, with heave plates providing viscous damping and cylindrical columns providing suitable buoyancy. TLP platforms are mooring stabilised, through taut mooring lines anchored to the seabed. These lines are vertically loaded and commonly utilise gravity anchors to provide tension. Unlike the spar platform, these platforms can be utilised in very shallow and deep water. Tensioning of the cables and the platform's instability in the event of line failure are disadvantages of this system.

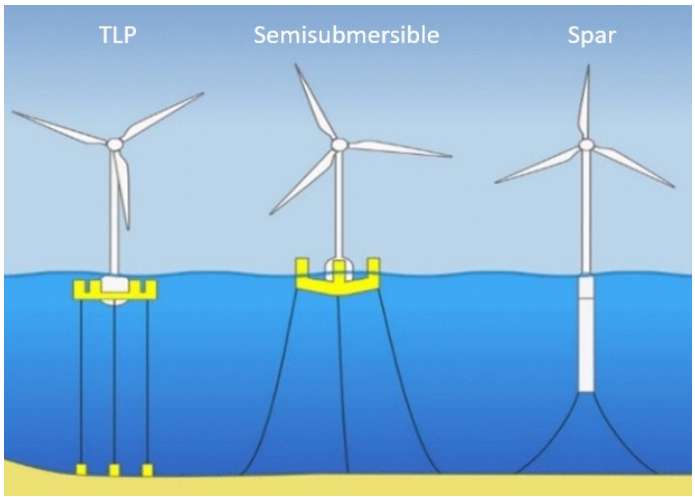
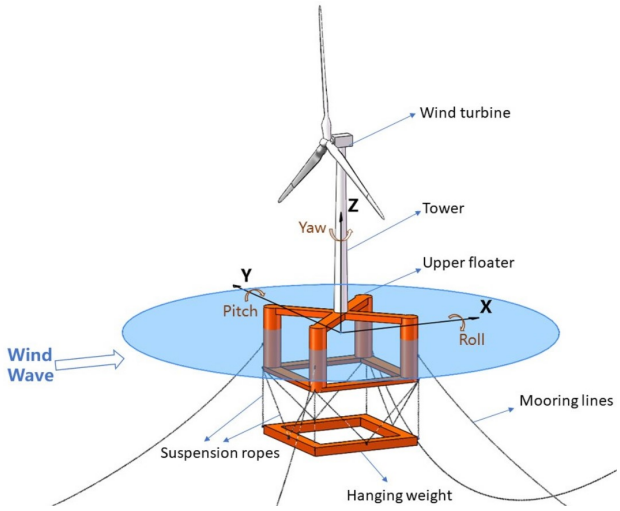


Figure 2.2: Primary FOWT platform types (Shafiee, 2023).



(a) Semi-spar (Cai et al., 2024).



(b) BW Ideol barge (BW Ideol, 2018).

Figure 2.3: Secondary platform designs

2.2 Environmental Conditions

FOWTs are exposed to three main elements when operational at sea: wind, waves and current. The interaction of these elements on the turbine and platform produces complex aero- and hydro-dynamic loading respectively. Detailed assessments of the meteorological, geological and oceanographic conditions of the proposed site are key to a suitable FOWT design (Atcheson et al., 2016). Numerical and model testing, using the expected site conditions, are commonly used to mitigate unforeseen design flaws in the development stage before full-scale deployment. Wind farms in the North and Baltic Sea can also experience ice, therefore the careful design of the structure to minimise sea spray and resulting icing on the platform surface is critical. Chemical coatings and actuation mechanisms have been employed in other industries to prevent icing however their application in the offshore wind industry is limited (Ryerson, 2011). Earthquakes can also disrupt the anchoring of mooring lines and damage electrical lines, therefore they must be considered when choosing suitable farm locations. However, while icing and earthquakes require consideration, wind, waves and currents are the focus of this thesis.

2.2.1 Wind

Wind energy occurs due to the temperature gradient across the earth's surface. Air flows from high-pressure areas to low-pressure areas in an aim to maintain equilibrium. Cold, high-pressure areas in the poles and warm, low-pressure regions around the equator are the driving force behind this gradient. Other contributors are the differing heat capacities of land masses and bodies of water, causing further gradients (Atcheson et al., 2016). As the earth rotates on its axis, the relative wind motion is changed, this is known as The Coriolis Effect.

While offshore wind turbines are driven by global wind patterns and are affected by The Coriolis Effect, other variations in the wind energy available to a wind turbine are the

turbine's height above the earth's surface, nearby obstacles and terrain. As land masses heat up quicker during the day than their surrounding water, an onshore wind occurs. This reverses at night when the air above the land mass sinks and is replaced by the rising air above the ocean, causing an offshore wind (Strahler, 2008). From a fluid mechanics approach, the available power from the wind, passing through a rotor disc of area A, is given by (Manwell et al., 2009):

$$P = \frac{1}{2}\rho A U^3 \tag{2.1}$$

Where ρ is the density of the air and U is the air velocity. Power is proportional to air density, which is a function of temperature and pressure, p. As temperature and pressure are a function of height, the turbine height can impact the power capability of a wind turbine. Wind speed also changes with height, this is due to the exponential wind shear profile (Figure 2.4). Manwell et al. (2009) discusses two laws for estimating wind speeds at various heights, the log law and the power law. The power law is a simple approach, based on a measured value of wind speed, U, at a given height, z:

$$\frac{U(z)}{U(z_r)} = \left(\frac{z}{z_r}\right)^{\alpha} \tag{2.2}$$

Subscript r indicates the reference values from the measurement and α is the power law exponent. Early work indicated α was equal to 1/7. It was later found that the value changes with time of day, terrain, wind speed along with other thermal properties. As a result, researchers often fit values of α to fit available wind data. The uncertainty in this value can affect the fatigue loading on a wind turbine as it passes through a range of heights between 50-250m for modern turbines (Manwell et al., 2009).

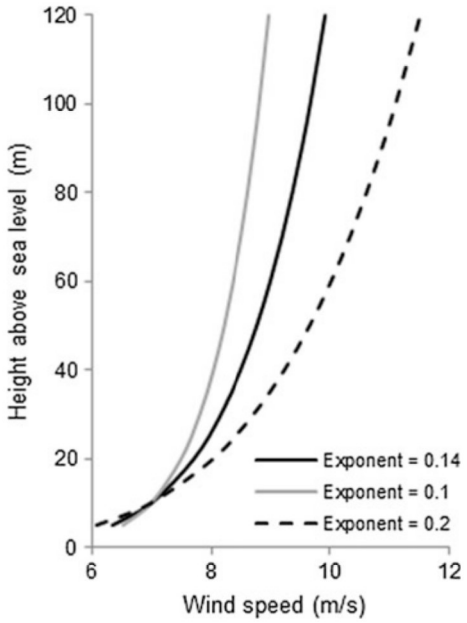


Figure 2.4: Vertical profile for a range of α (Atcheson et al., 2016).

Another variable of wind energy that can have detrimental effects on loading and power outputs is turbulence. Turbulence is generated from frictional and thermal effects, causing gradients in the wind flow and subsequent generation of eddies and gusts (Atcheson et al.,

2016). Over a long period of an hour or more, turbulent flow can display a constant mean value, however, it can be quite erratic in the minutes and seconds scale. Turbulence Intensity (TI) is the most basic description of the turbulence of a flow. TI is a ratio of the standard deviation of the wind speed, to the mean wind speed, as seen in equation (2.3). The standard deviation and mean wind speed are commonly taken over periods longer than the turbulence fluctuations. Manwell et al. (2009) noted the conventional period in wind energy engineering to be ten minutes.

$$TI = \frac{\sigma_u}{U} \tag{2.3}$$

Where σ_u is the standard deviation and U is the flow velocity. It can be seen that TI is prominent in low-speed conditions, where a high standard deviation can contribute to a high TI. Mücke et al. (2011) investigated the effect of turbulence on alternating wind loads of wind turbines. They concluded the gusty nature of turbulence produces intermittent torque loads on the turbine and that atmospheric measurements provide higher torque fluctuations than a Gaussian distribution, due to atmospheric inflow. Turbulence not only causes fatigue loading, but it can also lead to variations in power generation and thus an accurate turbulence model is required to replicate site-specific wind loads, in the design phase.

As discussed in section 2.1, both fixed bottom and floating offshore wind turbines are breaking records for the largest rotors and greatest capacity. This is partially due to the smoother wind flow due to the lack of obstructing terrain, and the greater wind speeds that are accessible when the turbines are placed higher above sea level, as seen with the vertical wind profile.

2.2.2 Waves

Ocean surface waves result from wind blowing over the sea and thus are indirectly linked to the thermal factors that generate wind. Unlike fixed-bottom offshore wind turbines, FOWT dynamics depend on the hydrodynamic interaction between the platform and water. Testing the platform using the expected sea states from the proposed site is important to predict mooring tensions and platform dynamics. A starting point is to obtain the significant wave height and peak wave period.

A regular wave can be defined by several factors, of which its height (H), amplitude (a), wavelength (λ), celerity (C) and period (T) are some of the main characteristics. Irregular waves are highly chaotic and thus instead of a time period description, a frequency domain is used to represent the sea surface as a sum of waves of different periods, wavelengths and directions (Figure 2.5).

A standard form of wave frequency spectrum was devised by the Joint North Sea Wave Project, commonly known as JONSWAP. Unlike other wave spectra such as the Pierson-Moskowitz, which represents a fully developed sea state produced by winds blowing steadily over a large distance for several days, JONSWAP describes a developing sea state, where waves grow with either distance or time. Analysis of the data produced a spectral formulation for coastal wind-generated seas. The mean JONSWAP wave spectrum is given by (Journée and Massie, 2001):

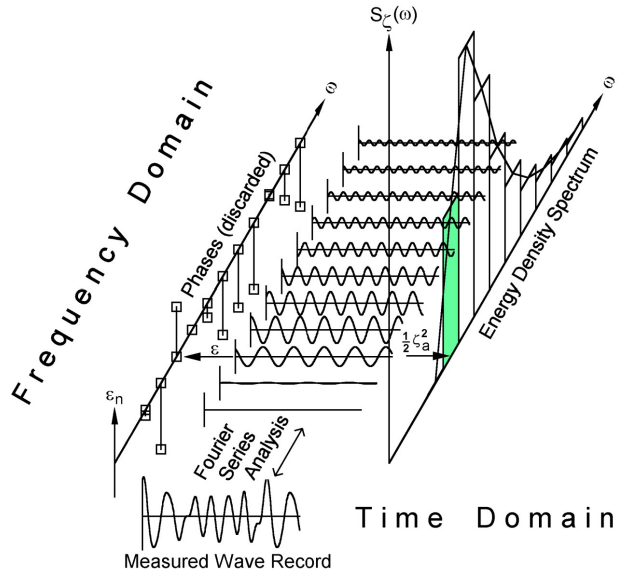


Figure 2.5: Energy density spectrum from a wave record analysis (Journée and Massie, 2001).

$$S_\zeta(\omega) = \frac{320 \cdot H_{1/3}^2}{{T_p}^4} \cdot \omega^{-5} \cdot exp\left\{\frac{-1950}{{T_p}^4} \cdot \omega^{-4}\right\} \cdot \gamma^A \tag{2.4}$$

where:
$H_{1/3}$ = significant wave height (m),
T_p = peak of the spectrum,
$\omega_p = \frac{2\pi}{T_p}$ (circular frequency at spectral peak),
$\gamma = 3.3$ (peakedness factor),
$A = exp\left\{-\left(\frac{\frac{\omega}{\omega_p}-1}{\sigma\sqrt{2}}\right)^2\right\}$,
σ = a step function of ω:
if $\omega < \omega_p$, $\sigma = 0.07$
if $\omega > \omega_p$, $\sigma = 0.09$

Deep water waves are used throughout the testing, defined by a value of $d/\lambda > 0.5$ (Journée and Massie, 2001). Using Airy wave theory, a relationship between ω and k is established:

$$\omega^2 = kg \cdot tanh(kh) \tag{2.5}$$

The deep water relation between T_p and λ becomes:

$$\lambda = \frac{g}{2\pi} \cdot T_p^2 \tag{2.6}$$

2.2.3 Current

Ocean current contributes to the hydrodynamic loading on a FOWT platform in the form of viscous loading of the mooring lines. There are three types of ocean currents (Gordon and Cenedese, 2023):

1. Tidal Currents: These are prevalent near the shore, where the tide rises and falls, causing a horizontal displacement of water as the water ebbs and floods, in the form of currents.

2. Wind-driven: Blowing wind pulls on the surface of the water by means of the no-slip condition, leading to currents flowing in similar patterns to the winds discussed in section 2.2.1. These are also affected by trade winds, The Coriolis Effect and surrounding landmasses.

3. Thermo-haline circulation: The movement of ocean currents due to temperature (thermo) and salinity (haline) gradients in the water. These temperature and salinity gradients lead to density changes across regions.

The drag force as a result of the current load on the platform can be described using the Morison equation:

$$F_D = \frac{1}{2}\rho C_d A|U-u|(U-u) \tag{2.7}$$

Where A is the projected area, C_d is the drag coefficient, U is the current velocity and u is the platform velocity.

2.2.4 Wave-Current Interactions

In a technical report outlining the gaps and recommended advancements of testing procedures for offshore energy devices conducted by Noble et al. (2018), combined wave-current conditions in testing tanks were noted, to assess the durability, reliability and fatigue of devices. Currents alter the form of waves, by changing the wavelength and amplitude. A wave interacting with an opposing current will experience a shorter wavelength and increased amplitude. This is also met with an increase in spectral density (Draycott et al., 2018).

For the wave-only case, the wave frequency, ω and wavelength λ, can be obtained from the following:

$$\lambda = \frac{2\pi}{k} \tag{2.8}$$

$$\omega = \sqrt{gktan(kh)} \tag{2.9}$$

Where k is the wave number, g is the gravitational acceleration and h is water depth. When a current that is presumed to be uniform, moving in the horizontal direction, in deep water, is present, the wavelength and wave frequency are adjusted accordingly using:

$$\lambda_I = \frac{2\pi}{k_I} \tag{2.10}$$

$$\omega_r = \omega \pm k_I \cdot Ucos\alpha = \sqrt{gk_Itan(k_Ih)} \tag{2.11}$$

Where U is the current velocity and ω_r is the reference frame wave frequency. α is the angle between current and wave propagation directions. The subscript I denotes the value with the addition of current. The $\pm$ indicates the current either following (+) or opposing (-) the wave motion. As discussed earlier, the wave amplitude is also altered depending on the wave-current interaction. Equation 2.12 is used to account for this interaction:

$$A_I = A_0\sqrt{\left(\frac{C_{g,0}}{C_{gr,I}+Ucos\alpha}\right)\left(\frac{1}{1+Ucos\alpha/C_{gr,I}}\right)} \tag{2.12}$$

With C_{gr} indicating wave group celerity. Similarly, the wave energy spectra are adjusted by the following:

$$S_I(\omega) = S(\omega)\frac{4}{\left[1+\sqrt{1+(4U\omega/g)}\right]^2\sqrt{1+(4U\omega/g)}} \tag{2.13}$$

Draycott et al. (2018) performed wave-current tests in the FloWave test facility and found that for a given wave, increasing the current velocity and relative angle between the wave and current, led to an increase in wave height (Figure 2.6). A comparison of spectral density for a range of current velocities and relative angles was conducted. The effect on spectral density with changing velocities and relative angles is also presented in Figure 2.7. The wave spectra display similar patterns to the wave height, with opposing currents and large relative angles showing larger responses and vice versa.

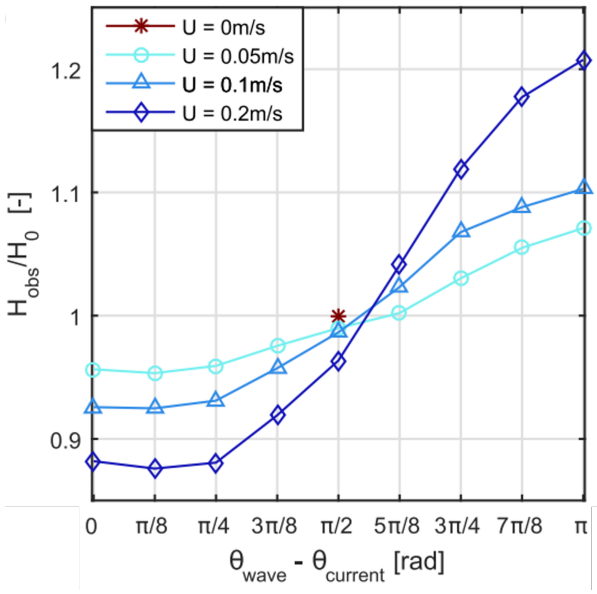


Figure 2.6: Impact of wave-current interactions on wave height. H_0 refers to wave height values obtained without the presence of current (Draycott et al., 2018).

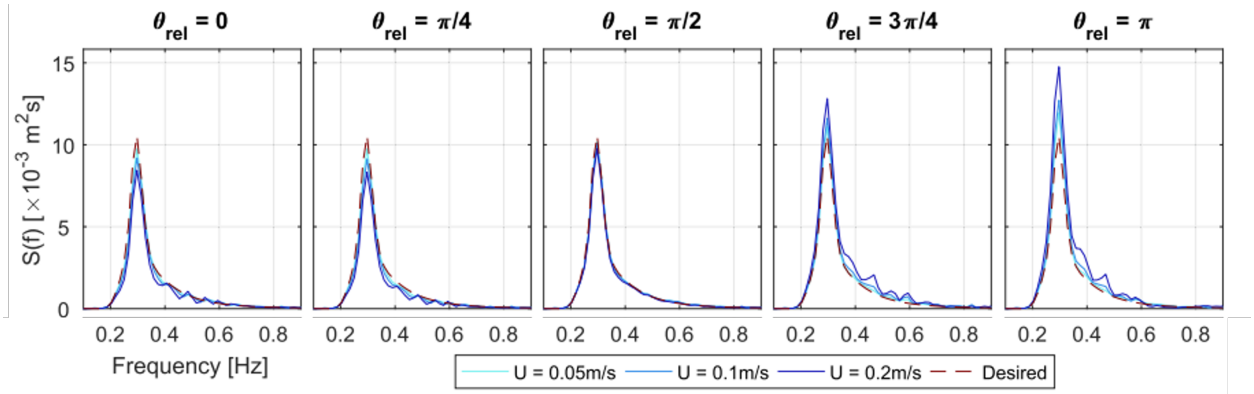


Figure 2.7: Impact of wave-current interactions on spectral density (Draycott et al., 2018).

2.3 Modelling of FOWTs

In the development phase of a FOWT, concurrent analysis of multiple systems is required. In an ideal scenario, a fully coupled hydro-aero-elastic-servo analysis would be carried out to consider the hydrodynamic loading of the platform and mooring lines, the aerodynamics of the turbine, elastic structural analysis of the turbine structure and a servo analysis of the drivetrain. Achieving a fully coupled analysis can be both financially and computationally expensive. A fully coupled analysis, such as that described by Connolly et al. (2018), aims to incorporate all loads experienced in real site conditions, using numerical simulation. They found a good agreement, with steady wind loading for a range of sea states (random and regular), with experimental tests, identifying the capabilities of numerical simulations.

2.3.1 Numerical Modelling

2.3.1.1 Software Fidelity

Numerical simulation tools are widely used across engineering disciplines to reduce prototype testing costs and aid engineering decisions in the design phase (Figure 2.8). When using numerical models during each stage of the design, an efficiency analysis must be carried out to ensure the correct fidelity model is being used, based on the requirements of each stage. Commonly, designers use low-fidelity models for quick, initial design work, before moving onto medium-fidelity for validation and optimisation of the structure. Lower fidelity models are used for rapid testing with larger margins of error and uncertainty. For final design changes, high-fidelity, computationally expensive models are used to confirm low- and mid-fidelity results (Otter et al., 2022b).

Otter et al. (2022b) carried out a comprehensive review of the modelling techniques of FOWTs. Table 2.6 indicates commonly used mid-fidelity software and their methods for analysing FOWTs. The Offshore Code Comparison Collaboration project (OC) focuses on comparing engineering tools of different complexities, to understand the discrepancies and shortcomings of lower fidelity models. The OC6 project consisted of four phases between 2019-2023 (IEA, 2023), with phase 1 looking at nonlinear hydrodynamics. A major finding from Phase 1 was the under-prediction of the response of the DeepCWind semi-submersible platform using engineering tools, compared to experimental tests in MARIN (Robertson et al., 2020). It was determined that the engineering tools were missing the underlying physics required to predict the nonlinear hydrodynamic loading on the platform. While this used experimental data to tune the engineering models, a separate investigation into using high-fidelity Computational Fluid Dynamics (CFD) for tuning is ongoing.

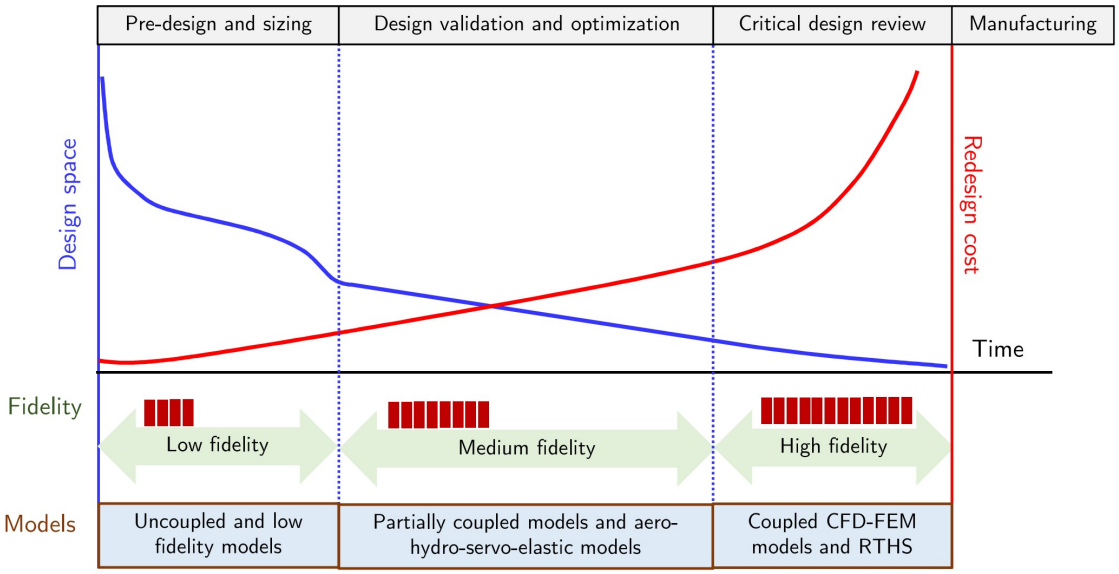


Figure 2.8: Models utilised during stages of FOWT production (Subbulakshmi et al., 2022).

Table 2.6: Summary of software and methods used for the analysis of FOWTs (Otter et al., 2022b).

Software	Hydrodynamics	Aerodynamics	Structural
FAST	PF + ME	BEMT + GDW/FVW	RB + Modal/FEM + Dyn/QS
HAWC2	PF + ME	BEMT + GDW	FEM + Dyn
SIMA	PF + ME	BEMT	FEM + Dyn
Bladed	With SIMA	BEMT + GDW	Modal
SIMPACK	With HydroDyn	AeroDyn/AeroDynModule	FEM
Orcaflex	PF + ME	With FAST	RB + FEM + Dyn
Flexcom	PF + ME	With FAST	RB + FEM + Dyn

2.3.1.2 Hydrodynamic Coefficients

A common obstacle in ensuring accurate numerical simulations is the derivation of the hydrodynamic drag and added mass coefficients for FOWTs. Accurate drag coefficients are especially important with hybrid systems (see section 2.3.3), as the force emulation by actuators using SIL technology alters the platform's response and can misrepresent the coupling between applied loads and platform response. Mid- and low-fidelity computational tools require software such as AQWA, WAMIT and Nemoh for accurate radiation/diffraction analysis. This method requires high computational cost in generating the quadratic transfer functions (QTF) (Reig et al., 2023). As an alternative, to decrease computational time, platforms have been modelled under the assumption of slender body theory using the Morison equation.

Previous work carried out by Otter et al. (2022a) determined the drag coefficient, C_d, by resistance tests in the WCF in the Lir NOTF. The model was kept stationary in the surge DOF (x-direction), while physical current was applied, up to a current velocity of 0.28

m/s. The force in the surge DOF was measured and a drag coefficient was derived from the Morison equation (equation 2.7). Confidence in the acquired C_d was obtained from a relative error (RE) of ≤ 0.15 for the platform surge with SIL current. The symmetrical nature of the INNWINDEU model enabled drag coefficient testing to be conducted for one orientation of the platform only, with constant current flows.

Frequently, a combination of Potential Flow (PF) methods and the Morison Equation (ME) are utilised to account for first- and second-order loads in the analysis of a FOWT. The PF method has limitations in that a non-viscous flow is assumed, making it unsuitable for modelling complex flows around the FOWT columns and braces (Journée and Massie, 2001). Limitations of the ME approach include its slender structures assumption, where the ratio of the column diameter to the wavelength of the incident waves is less than 0.2. Semi-submersibles are large enough to disturb the wave flow and thus diffraction effects must be modelled to correctly replicate the local pressure force around the structure (Matha et al., 2011). ME is used for fixed-bottom wind turbines, due to their restricted motions, however floating platforms exhibit noticeably larger movement and thus radiation effects must be considered. A combination, therefore, of PF + ME methods is utilised when either method fails to accurately model the loading conditions on the FOWT individually. This combination is seen as more computationally efficient in comparison with CFD tools.

Adaptations to the PF + ME methods are common to improve its accuracy further. Ishihara and Zhang (2019) investigated the response of a semi-submersible FOWT with frequency-dependent Morison hydrodynamic coefficients. Forced oscillation tests were carried out in the water tank, to determine the effect of oscillating period (T_o) on the response of the platform. A steady flow test was also carried out for the horizontal drag, representing an infinite oscillating period. Results found a dependent relationship between C_d and T_o in the horizontal direction. Further tests found the amplitude and natural period in sway motion are overestimated when the hydrodynamic coefficients from the forced oscillation tests aren't corrected to account for frequency-dependent phenomena. The correction factors applied to the Morison equation better matched the experimental test, however, these correction factors are specific to the floater in the paper and are therefore not directly applicable to other platform designs.

Reig et al. (2023) proposed an accelerated second-order hydrodynamic load model for semi-submersible platforms. Slender body theory was employed by using the superposition of the platform's members assuming no interaction between them. While a semi-submersible is not slender, the superposition of its members was used. This bypasses the time-consuming double sum over frequencies calculations by using the eigenvalue decomposition of the QTFs. For diameter-to-draft ratios below 0.2, the pitch moment was well predicted with an error below 3%. While the surge force displayed a significant under-prediction of 22%, attributed to the slender body approach.

Benitz et al. (2015) conducted an investigation into the selection of hydrodynamic drag coefficients, with an emphasis on member interaction and shadowing of leading columns for semi-submersibles. A comparison was made using OpenFOAM and HydroDyn, for the case of a stationary semi-submersible in current-only conditions. HydroDyn used a drag coefficient for the columns based on an infinitely long, fully submerged cylinder at the same Reynolds number, while OpenFOAM generated drag coefficients for each column, as well as

a drag coefficient for the upper and base elements of the OC4 columns. A study comparing an isolated column against the OC4 setup with one front column and two trailing columns, showed a reduction in drag coefficient for the front and trailing elements compared to the isolated column. This demonstrated the effect other members have on the drag coefficient of others. The distribution of drag between the upper and base elements was also altered in comparison with the isolated column. For downstream columns, the drag on the base element increases while the drag on the upper element decreases.

Kvittem et al. (2018) conducted a calibration of hydrodynamic coefficients for a numerical model to experimental results of the OO-Star Wind Floater at the SINTEF facility. Applying potential wave theory, with slow drift forces, resulted in an underestimated low-frequency surge response as well as surge-pitch coupling and mooring line tensions. Drag coefficients from decay tests were also seen to underestimate low-frequency surge motions in irregular sea states. Adjustments to the horizontal drag coefficient in the upper and lower parts of the columns successfully reproduced low-frequency motions for the model.

2.3.2 Physical Modelling

Physical modelling of FOWTs produces complexities due to the scaling requirements of the two working fluids, air and water. Adaptations to the FOWT model are required to limit the scaling discrepancy of the fluids. This can be achieved through performance scaling of the turbine to match the thrust coefficient with the full-scale model, or Froude scaling of the turbine rotor and higher-than-Froude scaled wind velocity. Froude-scaling with higher-than-Froude-scaled wind velocity was used in an experimental test conducted by Mortensen et al. (2018), which consisted of a 1/35 scale TLP with a scaled 5 MW NREL reference turbine. MATLAB and FAST simulations correlated closely with experimental testing that utilised a wind tunnel and wave tank. Performance-scaling consists of geometrically modified, low-Reynolds airfoils with correctly scaled Froude wind velocity. Borisade et al. (2018) conducted tests with a model of the OC4-DeepCWind semi-submersible platform with a Froude scaled rotor with low-Reynolds airfoils in a wind-wave basin. Good agreement between experimental results and a SIMPACK model was seen for free-decay tests, irregular and regular waves and wind-only tests.

2.3.2.1 Scaling Laws

Scale model testing requires several similitude parameters to ensure the forces exerted on the model are representative of the full-scale design. Geometrical, kinematic and dynamic similarity are required to achieve this (Canabes, 2010). Geometric similitude consists of structures in model and full-scale having similar shapes, defined by a characteristic length ratio, $\lambda_L = L_f/L_m$, where subscripts f and m represent the full- and model-scales respectively. Kinematic similarity requires the velocity ratios to be equal across model and full-scale structures. Dynamic similarity requires the ratio of forces to be equal across model and full-scale tests. Such forces include inertial, gravitational, viscous, pressure, elastic and surface forces. Viscous, inertial and gravitational forces are vital for the analysis of FOWTs.

Physical modelling of FOWTs often consists of scale models being placed in wave tanks with wind generators. Wave tank models are attractive as they require less cost and risk compared to full-scale testing. They also display effects that can't be easily modelled in numerical simulations such as vortex shedding and mooring dynamics. Hydrodynamic model testing requires scaling of the Froude number (Fr), while aerodynamic models are scaled using the Reynolds number (Re). The combination of these scalings for FOWT models adds complexity to the design of the model. The Froude number for a free surface wave is given by (Atcheson et al., 2016):

$$Fr_{wave} = \frac{\text{Inertial Forces}}{\text{Gravitational Forces}} = \frac{U_m}{\sqrt{gL_m}} = \frac{U_f}{\sqrt{gL_f}} \tag{2.14}$$

Where U is the wave velocity (celerity) and L is a characteristic length. While the Reynolds number is:

$$Re = \frac{\text{Inertial Forces}}{\text{Viscous Forces}} = \frac{U_m L_m}{\nu} = \frac{U_f L_f}{\nu} \tag{2.15}$$

It can be seen that for a given scale ratio $\lambda_L = L_f/L_m$ (e.g. 50) if we aim to scale using Re, since the kinematic viscosity, ν, of air for the model and full-scale is constant, the model velocity is required to be 50 times the full-scale velocity, which is impractical. If Froude scaling is imposed, with g constant for both model- and full-scale, the model velocity is the square root of λ_L times the full-scale velocity. This is a more achievable figure and thus Froude scaling is used, albeit compromising by using a lower Reynolds number for the model. This can lead to a misrepresentation of the aerodynamic loading of the platform, thus hybrid approaches are utilised to address this.

2.3.3 Hybrid Modelling

Hybrid modelling offers an alternative to physical modelling by replacing one of the hydro-aero-elastic-servo forces experienced by a FOWT. This is often used to overcome the scaling issues, however, with the introduction of complexity and uncertainty in the test setup. This approach is used to accommodate testing facilities designed for either aerodynamic testing (wind tunnel) or hydrodynamic loading (wave tanks).

2.3.3.1 Wind Tunnel Testing

This system replicates physical aerodynamic loading using a wind tunnel with a scaled wind turbine rotor, with hydrodynamic loading replicating the wave loading by use of a platform or rig based on numerical simulations in software such as AQWA. The wind tunnel in Politecnico di Milano is commonly used for such testing. Bayati et al. (2017) used a 1/75, performance-scaled DTU 10-MW turbine placed on a 2-DOF rig to simulate the surge and pitch motions of the OC5 semi-submersible FOWT. This system was then upgraded to use a 6-DOF parallel kinematic Hexafloat robot to include all motions of a FOWT (Belloli et al., 2020) (Figure 2.9). For the 2-DOF system, free decay tests resulted in excellent replication of the frequency and damping compared with the numerical model and OC5 FAST predictions.

The 6-DOF Hexafloat control system was shown to have no impact on the wind turbine's aero-elastic response.

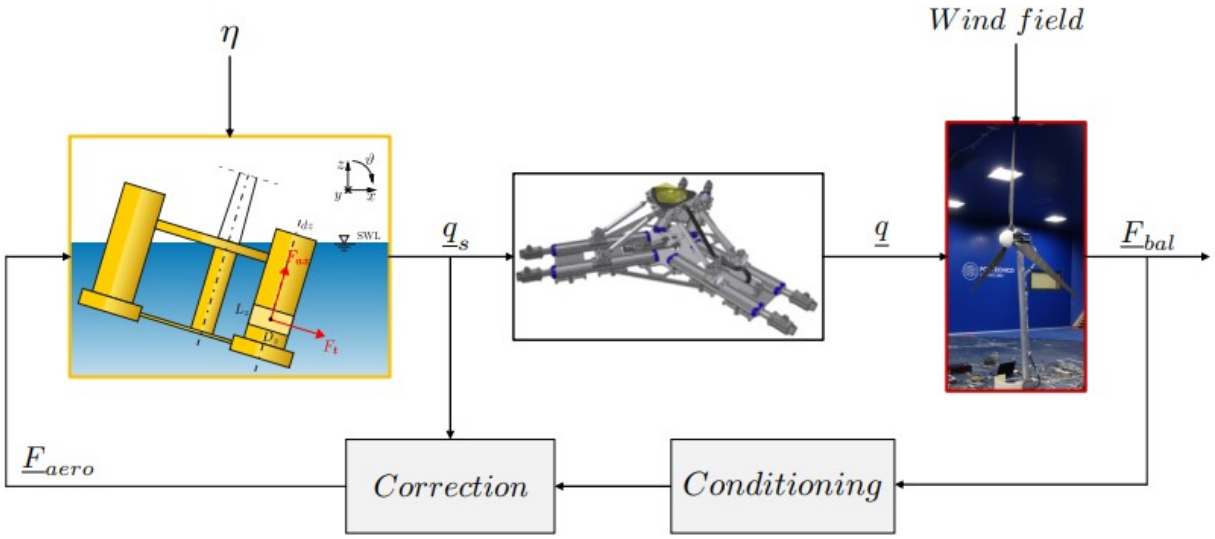


Figure 2.9: HIL setup for the Politecnico Wind Tunnel with a 6-DOF HexaFloat (Bayati et al., 2018).

2.3.3.2 Wave Tank Testing - Cable Actuators

A more common approach to the hybrid testing of FOWTs is the actuation of wind forces with the physical generation of hydrodynamic forces in wave and current tanks. The wind forces can be actuated through either the use of cable or propeller actuators.

Cable winch actuators are beneficial in wave basin testing of FOWTs as they (1) overcome Fr-Re scaling issues associated with physical aerodynamic loading (2) simulate all aerodynamic load components for varying requirements and (3) can apply unique situations such as blade seize or turbine braking through careful winch actuation.

Hall and Goupee (2018) implemented a single-DOF system to emulate rotor thrust only using two co-linear winch cables attached to the bow and stern sides of the turbine nacelle. This method adheres to the established technology of cable-driven parallel manipulators (CDPM), wherein an additional cable is incorporated beyond the simulated degrees of freedom (DOFs). This extra cable introduces redundancy into the system, thereby facilitating independent tension control. (Kawamura et al., 1997). Tests with and without an applied thrust force were conducted to disregard interference of the cable system on the platform response, with success. Further tests using physical wind generation from the facility were compared with cable-emulated thrust, using the same sea states. Platform motions and mooring tensions were reported to match well, validating the hybrid model approach. Significant differences in aerodynamic damping were seen between Froude-scaled and true-to-scale wind turbine performance. Turbulence was also seen to add significant excitation to the hybrid system. This highlights the value of a hybrid system in applying true-to-scale loading, without the complex physical wind generation.

Researchers in SINTEF, Norway, developed a real-time hybrid model (ReaTHM) using dynamic winch actuators to model the aerodynamic loading on FOWTs (Sauder et al., 2016,

Bachynski et al., 2016, Berthelsen et al., 2016). This consisted of a frame attached to the turbine tower, connected by 6 winch cables, emulating aerodynamic thrust, tangential aerodynamic force, generator torque and the pitch and yaw moments at the rotor. The choice to neglect the gyroscopic moments and vertical aerodynamic loads was made to reduce the workspace of the winch system.

Advancements on the ReaTHM system were undertaken by Thys et al. (2018), by simulating a 10MW semi-submersible FOWT in the ocean basin at SINTEF. The model experienced physical waves while the aerodynamic loadings came from cable actuation using a numerical model from FAST. Methods were advanced to simulate parked conditions and the bandwidth was extended to include 3P frequency and the first tower bending frequency.

A separate study uses the CFD solver REEF3D to simulate the hydrodynamics of the INO WINDMOOR semi-submersible (Berthelsen et al., 2022). This is coupled with the ReaTHM 6-DOF winch system and compared with experimental results of the WINDMOOR platform at the SINTEF ocean basin (Thys et al., 2021) (Figure 2.10). Simulation of decay tests in surge, pitch and heave are carried out as well as regular wave loading of the platform. The findings stated the surge- and heave-decay tests were more sensitive to grid size than the pitch test. Grid resolution of the CFD model was found to have an impact on the buoyancy and added mass forces. A comparison of measured data shows that wave-induced surge and heave motions were modelled well, with larger deviations for the pitch motions, however, the response of the pitch motions was small for this testing, which led to a large error. The responses of the small magnitude pitch motions were difficult to predict.

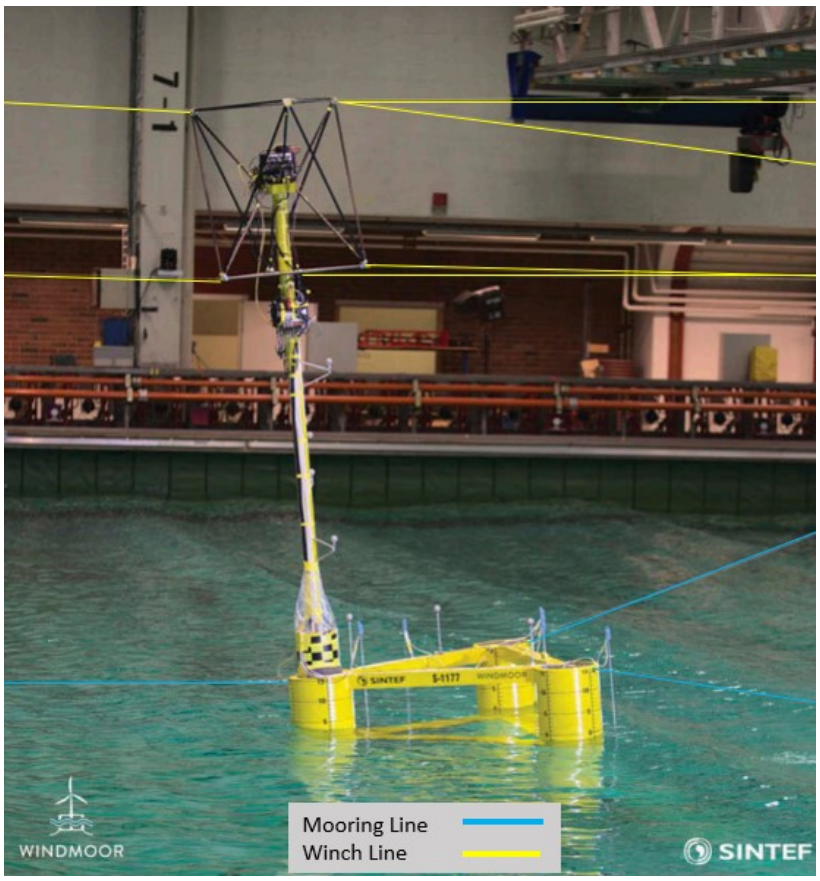


Figure 2.10: ReaTHM system mounted to INO WINDMOOR semi-submersible, adapted from (Berthelsen et al., 2022).

Emulation of current loading on platforms can be achieved through the use of a winch system similar to the ReaTHM design for emulating aerodynamic loads. The advantages of current loading of a platform through winch actuators are (1) their ability to exert precise current drag forces that current flumes may not reach, (2) it enables current application in basins that either do not generate current or are significantly expensive to do so (3) they can enable a variety of wave-current incidence angle combinations by combining two winches.

Otter (2022) developed a single winch actuator that enabled current emulation of the INNWINDEU semi-sub platform (Figure 2.11). Testing was limited to the case of wind and waves directly opposing the current direction only. Initial testing in the WCF compared the response of the platform to physical current and system-in-the-loop (SIL) current. This is a comparison of a hybrid testing method and a full testing method. Physical current was generated using three thrusters in the circulation gallery of the WCF, in combination with a 44% porous screen to reduce turbulence in the flow. The winch is attached to column C2 of the platform, at the COG to reduce unwanted pitch motion of the platform. An initial accuracy test of the winch actuation was conducted in still water as shown in Figure (2.12). During this test (TC 1), the system received tension feedback through a loadcell in the winch wire, however, no Qualisys motion tracking was used, thus for this test it is regarded as emulation without SIL. The measured signal tracks closely and the reliability between measured 1 and measured 2 has a correlation coefficient of 0.994.



Figure 2.11: Single winch actuator in the WCF (Otter, 2022).

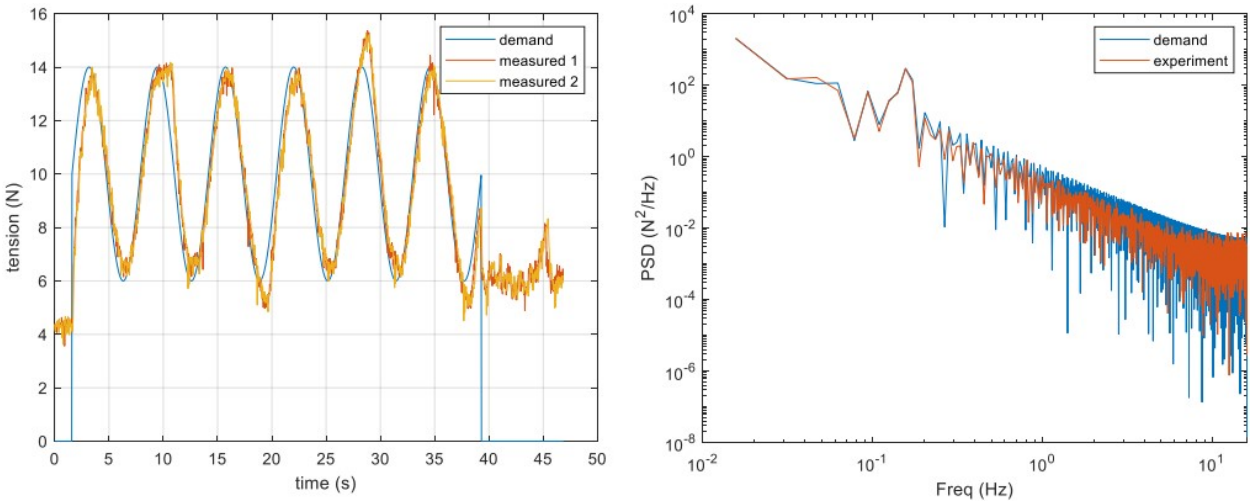


Figure 2.12: Winch actuation accuracy in still water (Otter, 2022).

Figure 2.13 compares physical and SIL current in the WCF. The oscillation amplitude of the physical current is larger, however, both settle at a similar surge distance, with disturbances in the physical current attributed to sway motion due to vortex shedding, which is not simulated with SIL current.

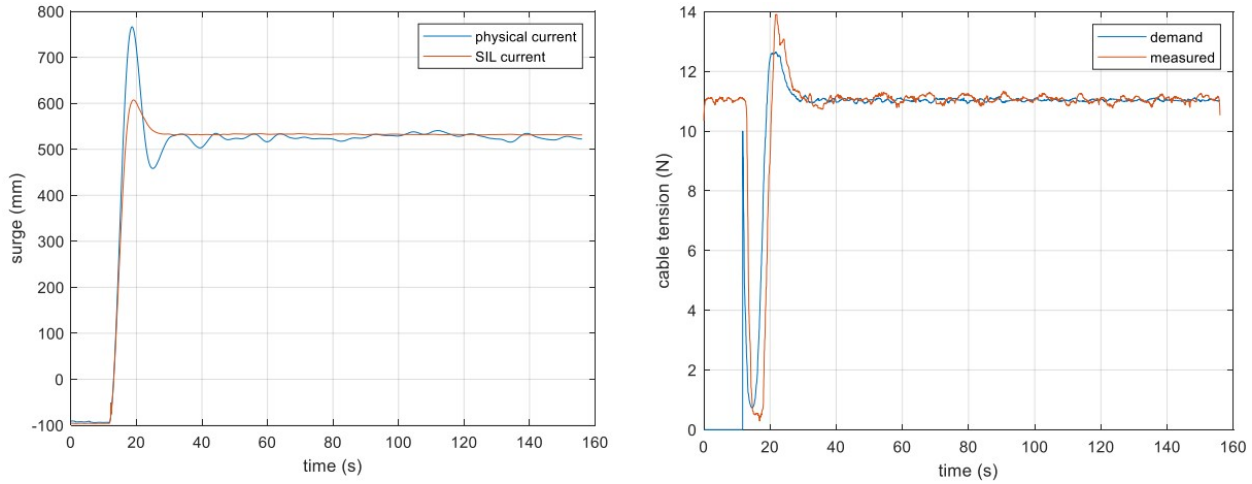


Figure 2.13: Physical vs. SIL current in the WCF (Otter, 2022).

2.3.3.3 Wave Tank Testing - Propellor Actuators

Propeller actuators are an alternative to cable winch actuators, in an attempt to overcome scaling laws and accurately reproduce aerodynamic loads. Bachynski et al. (2015) carried out a sensitivity analysis for FOWTs to different aerodynamic loads. The relatively small motions of the platform chosen for the testing inflated the coupling between aerodynamic loading and platform response, however, the significant loads were highlighted. Thrust and rotor torque were the leading forces, with gyroscopic moments and the vertical component of thrust deemed insignificant in comparison.

A series of experiments have been conducted to simulate the aerodynamic loadings of a wind turbine through propeller actuators as seen in Table 2.7. Azcona et al. (2014) found the experimental and aero-servo-hydro-elastic simulations matched well for emulation of the turbine thrust, using a single ducted fan. Pires et al. (2020) then upgraded the system by

Azcona et al. (2014), to incorporate 4 propellers. The findings from this study found the gyroscopic moments are of less significance than the rotor torque. Urbán and Guanche (2019) developed a system with 6 propellers, however, this study emitted gyroscopic moments and used constant wind loading only. They found the simultaneous modelling of thrust, torque and wind shear by the device was within 2% of theory. Otter et al. (2020) developed a 6-propeller wind emulation device termed a Multi Propeller Actuator (MPA). Results found the MPA to be suitable for emulating aerodynamic loads for thrust and torque only, with poor yaw and gyroscopic moment results.

Table 2.7: Literature review of propeller actuators for FOWT testing.

Reference	Propellers	Thrust	Rotor Torque	Gyroscopic Moments
Otter et al. (2020)	6	✓	✓	✓
Urbán and Guanche (2019)	6	✓	✓	✗
Pires et al. (2020)	4	✓	✓	✓
Azcona et al. (2014)	1	✓	✗	✗

2.4 Process Control

Process control is comprised of three fundamental variables:

- Control Variables: These are the variables that are controlled. The desired value of these variables is the set point, e.g. line tension.
- Manipulated Variables: The variables that can be altered to keep the control variables at or near their set point, e.g. flow rate, motor voltage.
- Disturbance Variables: Variables that affect the values of the controlled variables, but that cannot be manipulated, e.g. environment temperatures, platform surge.

Control problems, such as the single winch actuation system from Otter (2022) discussed in section 2.3.3.2, are referred to as single-input, single-output (SISO) systems (Seborg et al., 2016). These have one controlled variable (winch line tension) and one manipulated variable (winch motor voltage). Many systems deal with multiple-inputs, multiple-outputs (MIMO), such as the current emulation system with two winches. For this system, the controlled and manipulated variables remain the same as in the SISO system, however, there are now two of each. Unlike the SISO system, MIMO contains process interactions, that is the interaction of one manipulated variable on more than one controlled variable. Figure 2.14 gives an example of a MIMO system where manipulated variables have an impact on more than one controlled variable, where G_{p12} and G_{p21} are the process interactions. If manipulating one variable does not affect the other variable, these can be set to zero, this is known as partial decoupling. If interactions occur between each system, however, a full decoupling system is required to compensate for this. Figure 2.15 presents the same MIMO system, with feedforward decoupling controllers to eliminate the control loop interactions. When

correctly designed, decouplers enable the stability of the individual closed-loop systems to determine the system's stability. Additionally, a set-point change for one controlled variable does not affect others. The design of the decoupler is completed as follows:

Equation 2.16 is used to cancel the effects of y_{21}

$$G_{p21}u_{11} + G_{p22}u_{21} = 0 \tag{2.16}$$

Substituting $u_{21} = D_{21}u_{11}$ and factoring gives:

$$D_{21}(s) = -\frac{G_{p21}(s)}{G_{p22}(s)} \tag{2.17}$$

If the process dynamics of the two loops are similar, static decoupling can be implemented to reduce the dynamic equation 2.17 to equation 2.18. A disadvantage of this simplification is the presence of control interactions during transient conditions.

$$D_{21} = -\frac{K_{p21}}{K_{p22}} \tag{2.18}$$

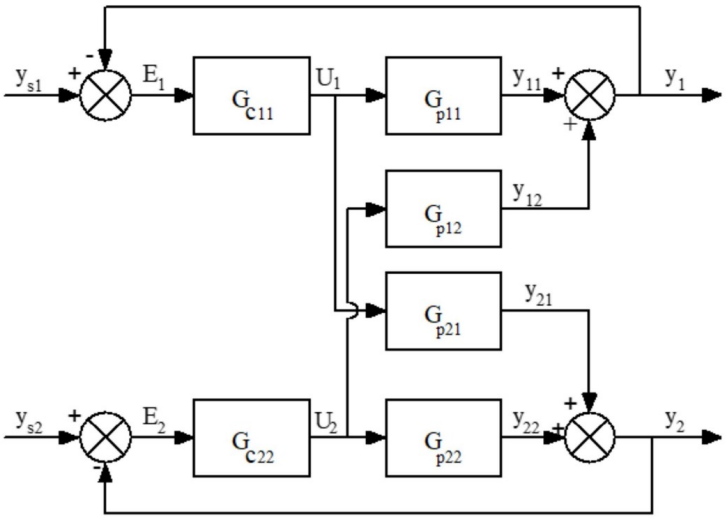


Figure 2.14: Block diagram of a MIMO system (Seborg et al., 2016).

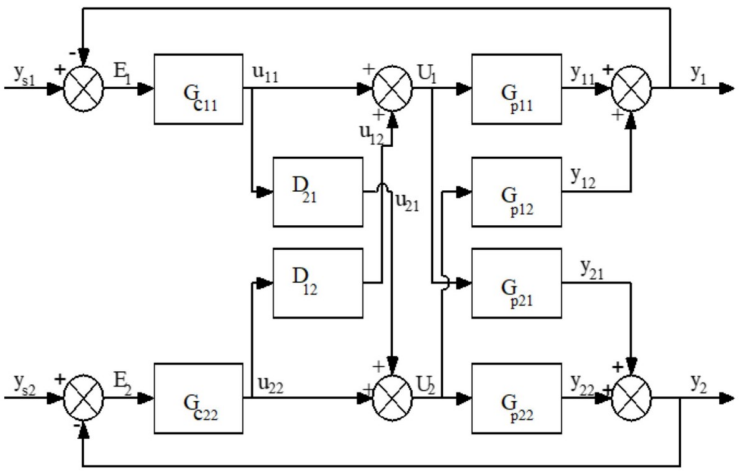


Figure 2.15: Block diagram of a MIMO system with decoupling controllers (Seborg et al., 2016).

Table 2.8 summarises the effects of independent Proportional (P), Integral (I) and Derivative (D) tuning on closed-loop behaviour.

Table 2.8: PID behaviour, adapted from (Li et al., 2006)

.

	Rise Time	**Overshoot**	**Settling Time**	**Steady-State Error**	**Stability**
Increasing K_p	Decrease	Increase	Small Increase	Decrease	Degrade
Increasing K_I	Small Decrease	Increase	Increase	Large Decrease	Degrade
Increasing K_D	Small Decrease	Decrease	Decrease	Minor Change	Improve

Ahmed et al. (2011) demonstrated the use of decouplers to remove process interactions between light bulbs. Open-loop tests were conducted individually to determine the bulb skin temperature response to a step input in current. Tests to determine the process interactions were conducted by measuring the inactive bulb's response to the active bulb's input. This enabled the transfer functions of the processes to be obtained. Figure 2.16 displays the reduction in the response of the right bulb due to the step change in the left bulb. The decouplers used in Ahmed et al. (2011) follow a similar design process as described by equations 2.16 and 2.17.

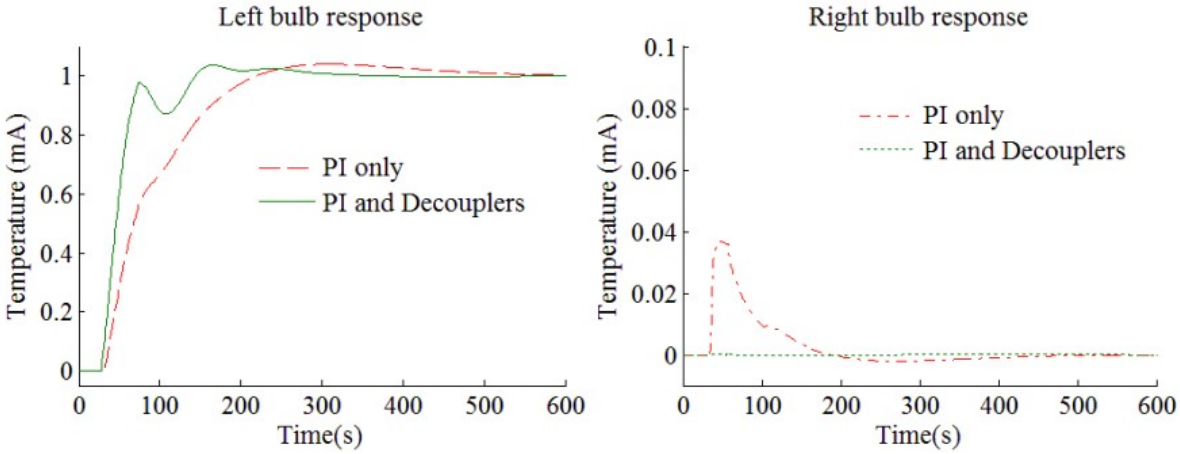


Figure 2.16: Decoupler effect on bulb process interactions (Ahmed et al., 2011).

2.5 Mooring Systems

2.5.1 Overview of Mooring Systems

A mooring system for a FOWT is employed to restrain the movement of the structure within allowable limits. The mooring must account for horizontal, vertical and rotational displacement. The main types of mooring systems for semi-submersible platforms are catenary and taut, while multi-catenary and buoyant semi-taut systems are also used (Figure 2.17).

- Catenary: Uses free-hanging chains leading to a catenary shape. A portion of ground chain is used to provide a horizontal restoring force, while the weight of the chains

provides vertical damping of the platform's response. This system is chosen for its simplicity and relatively low cost. It is commonly used in shallow waters.

- Multi-catenary: Similar to the traditional catenary system, with the introduction of floats and clump weights to tune the response of the system.
- Taut: This system uses taut lines between the structure and anchors. Gravity or suction-piled anchors are frequently used, depending on seafloor conditions. Compliance is added through the elasticity of a rope section.
- Buoyant semi-taut: Combines a lower catenary section with a taut upper section by the use of floaters and ground chains.

The choice of mooring system is determined by the seabed geology, water depths and cost. The minimum cost for mooring systems is seen in the depth range of 100-150 metres with the cost increasing above and below this range due to wave interaction (shallower) and chain cost (deeper) (BVG Associates, 2023). BVG Associates (2023) estimated the cost of the mooring system of a 450 MW floating offshore wind farm to be £80 million, distributed as £17 million, £50 million and £9 million for the anchor, mooring line and jewellery respectively. Jewellery refers to a range of components attached to the mooring line (Figure 2.19).

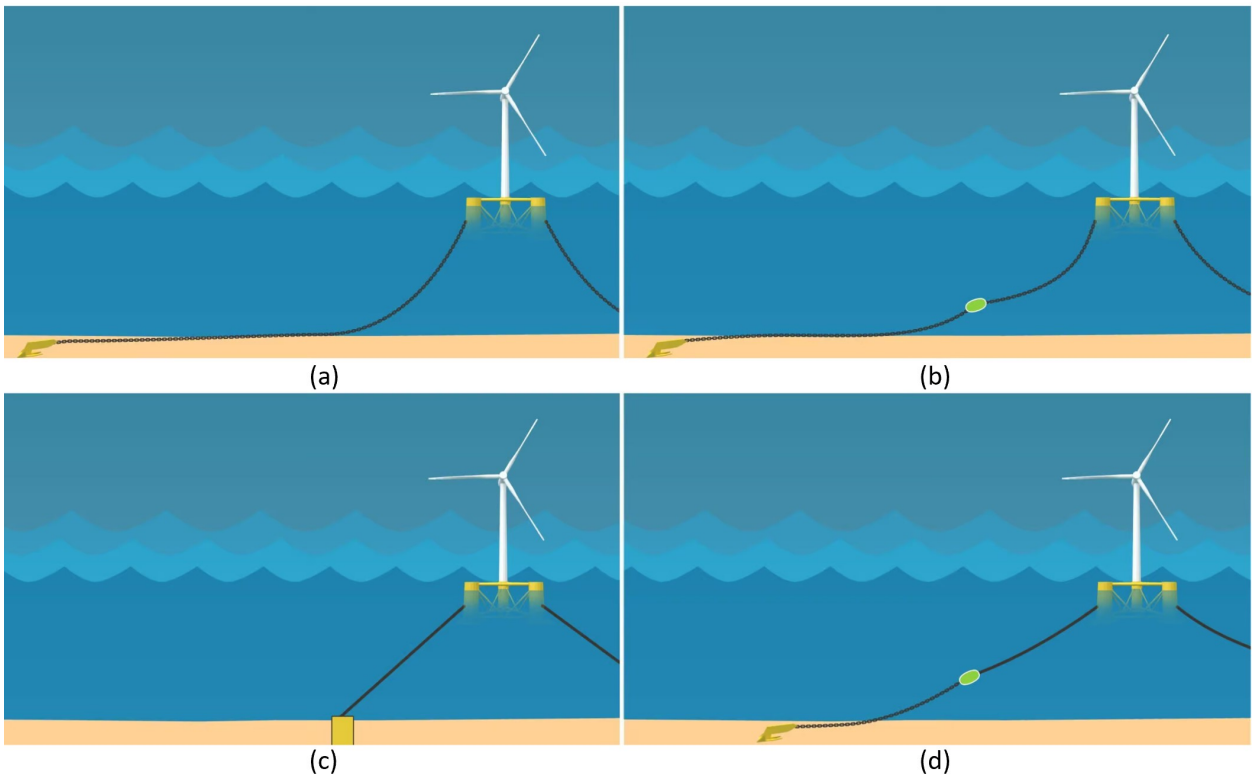


Figure 2.17: (a) Catenary (b) Multi-catenary (c) Taut (d) Buoyant semi-taut, mooring systems (BVG Associates, 2023).

2.5.1.1 Mooring Line

The mooring line of a FOWT is commonly comprised of three sections, lower (seafloor), middle and upper (platform). Chains are frequently used for the lower section due to their abrasive resistance and their weight, providing restoring forces (Atcheson et al.,

2016). Synthetic fibres are often used in the middle section for their stiffness-to-weight characteristics and high load capacity. The drawback of synthetic fibres is their durability, with nylon, polyester or HMPE commonly wrapped in a HDPE jacket to provide abrasive resistance (BVG Associates, 2023).

2.5.1.2 Anchors

Mooring systems induce horizontal and vertical loading on anchors. Seabed conditions also determine the type of anchor for the system. Figure 2.18 displays common anchor types. Catenary mooring systems predominantly use drag anchors [3], where seabed conditions allow, while taut mooring systems impose high vertical forces which require specialised anchors. Driven pile [2], suction pile [4] and torpedo pile [5] require geological analysis of the seafloor conditions and offer a permanent solution. For short-term operations, the geophysical analysis can be reduced by implementing dead weight [1] and vertical load anchors [6] where possible (Ma et al., 2019).

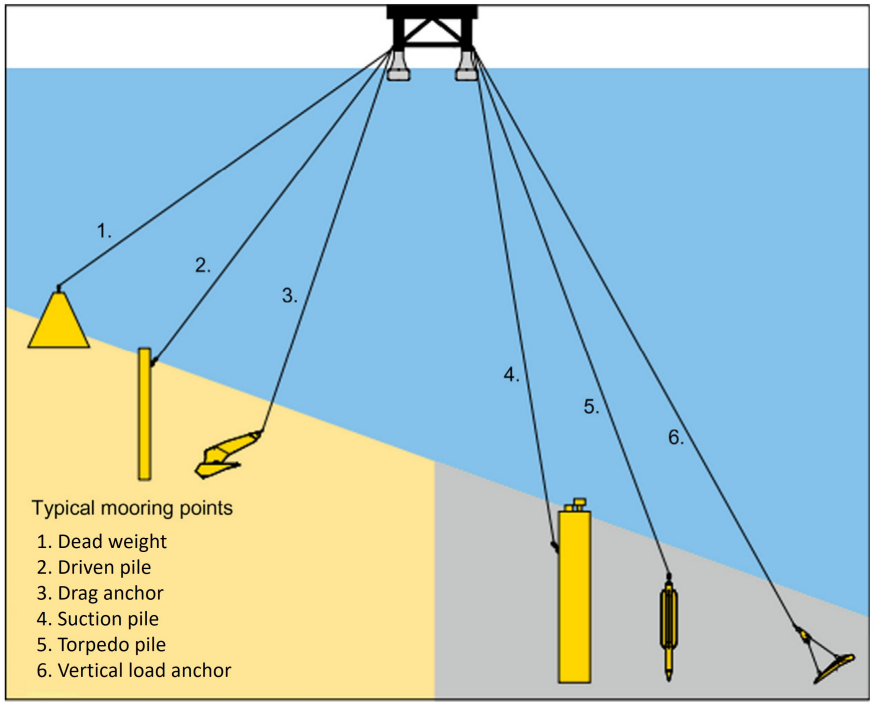


Figure 2.18: Anchor styles for general FOWT applications (Vryhof, 2015).

2.5.1.3 Jewellery

General components located along the mooring line between the anchor and structure consist of connectors, buoyancy aids, clump weights, load reduction devices and in-line tensioners. Connectors such as H and D links are used to connect sections of rope/chain. Buoyancy aids and clump weights, attached using tri-plates, tune the compliance of the mooring systems response. Load reduction devices are used to dampen the response of the platform, reducing tension loading in the mooring line. These can operate on hydraulic, gravitational or elastic principles. In-line tensioners maintain tension in the mooring line and can be operated by adjusting lines attached to surface buoys. This reduces cost and improves the reliability of the system through simplification.

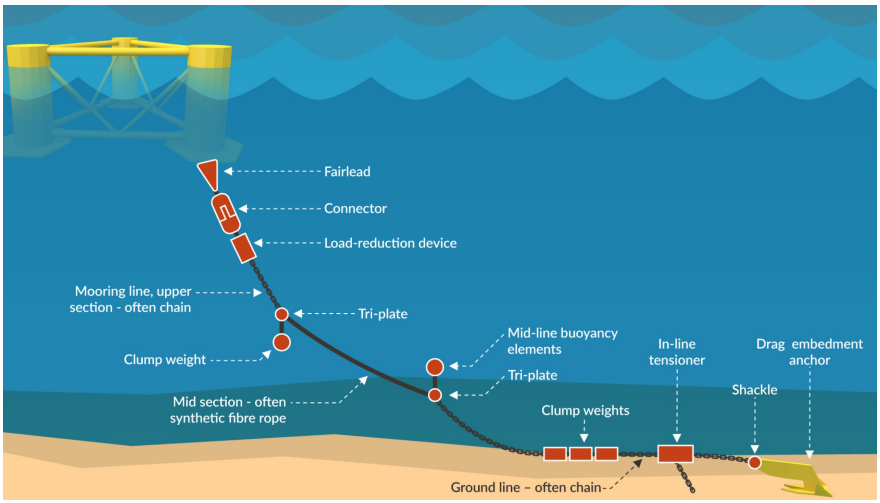


Figure 2.19: Range of components commonly connected to a mooring line (BVG Associates, 2023).

2.5.2 Numerical Modelling of Mooring Systems

For numerical modelling of mooring systems, either a dynamic or quasi-static (QS) approach is used. The QS approach is a low-fidelity method, that ignores the inertia forces and the fluid drag loads while accounting for the mean forces in the mooring system such as elasticity of the line, weight and nonlinearities. Dynamic models are a medium-fidelity solution such as those used in MoorDyn, FEAMooring and OrcaFlex. While computationally more expensive, the hydrodynamic drag and inertia loads provide a more accurate representation of the system. Wendt et al. (2016) compared MAP++ (QS), with MoorDYN and FEAMooring coupled to FAST v8 (Dynamic) to determine the significance of dynamic inclusion for mooring system modelling. Wendt et al. (2016) found the coupled FAST v8 setup had similar fairlead load predictions with the commercial OrcaFlex software. The QS-based MAP++ was unable to replicate the fairlead load amplitudes during regular and irregular wave cases. All dynamic mooring modules were able to sufficiently reproduce the fatigue spectrum of the fairlead load signal and also predicted the fairlead loads in extreme, slack-line tension scenarios.

Hall et al. (2014) compared QS and dynamic approaches for spar, semi-submersible and TLP platforms. They concluded that for spar platforms, with fairlead locations close to the centre of mass, small movements and slack moorings, a QS approach can accurately predict the platform response, however should not be used to evaluate mooring line loads. QS models are not applicable for evaluating slack-moored designs with large motions and fairleads a distance from their centre of mass, such as semi-submersible platforms.

Azcona et al. (2017) investigated the effect of mooring dynamics for a spar, semi-submersible and TLP. Mooring line tension was found to be strongly coupled with line dynamics, both for fatigue and extreme load cases, for all platforms. The biggest influence was the semi-submersible platform, with the heave natural period inside the wave spectrum, mooring dynamics increased the equivalent tension by up to 57%.

Barrera et al. (2020) conducted a sensitivity analysis and found the dynamic modelling of the mooring system under predicted snap loads by 23% compared to experimental results, highlighting the limitations of dynamic mooring modelling for extreme conditions.

2.5.3 Physical Modelling of Mooring Systems

Froude scaling aids in the correct modelling of the mooring weight and inertia. Consequently, the hydrodynamic drag is not correctly scaled as a result of incorrect Reynolds scaling. Key model parameters are the weight per unit length, axial stiffness and line diameter.

Barrera et al. (2019) investigated the behaviour of catenary mooring systems. Findings included the damping effects of the mooring line was more prominent for tests with shorter periods and the lightest line was the most efficient in damping the platform motion in relative terms, when non-dimensional parameters are used. Both the maximum and minimum tension were experienced by the mooring line, for large amplitude, short period conditions, where snap loads are common. When current loading was introduced, energy dissipation of the mooring line increased up to 6% for short periods, however, long periods showed a negligible difference in mooring line dissipation. Mooring line tensions increased with the addition of current, with increases of 6-13% and 3-4% for maximum and minimum loads respectively. The addition of a sand bed on the basin floor was used to test the effects of seafloor friction on mooring line dynamics. For dynamic periods (less than 2.25 s), the energy absorbed increased with sand, in both surge and heave motions, with minimal difference in energy absorption for longer periods. Similarly for dynamic periods, the maximum tension increased by up to 11%, with minimal increases for longer periods.

Barrera et al. (2020) furthered these findings by conducting a sensitivity analysis for modelling a mooring system. The physical characteristics of the mooring line used were shown to affect mooring line loads. Inertial forces were found to be negligible on line loads, while variations in the drag coefficient by 50% led to a 30% increase in mooring loads. Similarly, a 10% discrepancy in the ratio of weight-to-diameter for the catenary chain resulted in an increase of 11% for mooring loads. Mooring line length showed extreme sensitivity, with a 1% error resulting in mooring loads up to twice the experimental loads.

Truncated mooring systems are used to replicate a catenary mooring system, in ocean basins, where insufficient water depth prohibits the modelling of a full-scale mooring system (Figure 2.20). Using geometric similitude, with a focus on scaling the *sensitive* parameters as discussed by Barrera et al. (2020), the error between a truncated and full catenary system can be reduced. To replicate the mooring line forces, a calibrated spring can be enforced to replicate the equivalent elasticity of the lower, middle and upper sections commonly seen in a catenary line. Tensile testing of the catenary chains has been used by Barrera et al. (2019) to compare laboratory standard chains with mooring line standards according to DNV (2015).

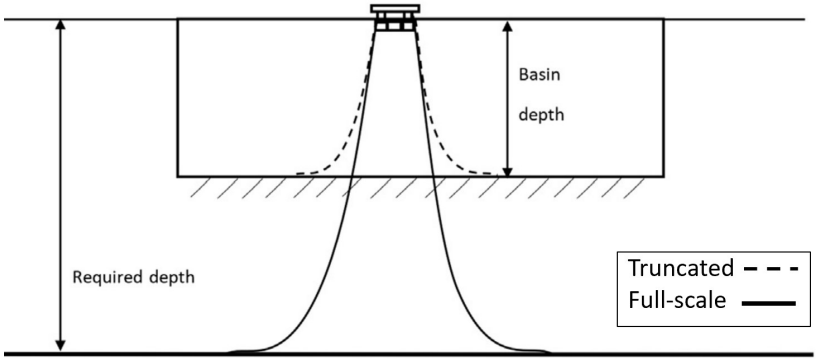


Figure 2.20: Truncated mooring system (Ma et al., 2019).

Chapter 3 - Test Setup

This chapter describes the models used for testing, the Lir National Ocean Test Facility (NOTF), the test plan and specifications of the hardware and software used during testing. Two devices were used throughout testing, the INNWIND Semi-submersible FOWT platform and the OE Buoy WEC. Two devices are chosen to investigate the impact of different body shapes on drag coefficient during tow-testing and resistance testing. The INNWIND model was selected as this platform was used during the initial testing of the winch actuation conducted by Otter (2022). The OE Buoy is used for the drag coefficient testing only and was selected due to the availability of the model and its contrasting geometric shape to the INNWIND model.

3.1 Lir National Ocean Test Facility

Experimental testing was conducted in the Lir NOTF, situated in the UCC Beaufort Building in Ringaskiddy, Co. Cork. Two wave basins were used during testing, the Wave Current Flume (WCF) and Deep Ocean Basin (DOB). The WCF is a multi-purpose facility with wave and current ability. It has a length of 28 m, a width of 3 m and a depth of 1 m. Eight hinged force-feedback paddles can generate waves with $H_s = 0.16$ m, $T_p = 1.5$ s and $H_{max} = 0.35$ m while three thrusters can generate current velocities of up to 1 m/s. The DOB has a movable floor enabling depths of up to 3 m, a width of 12 m and a length of 35 m. Sixteen hinged force-feedback paddles are capable of producing waves with $H_s = 0.6$ m, $T_p = 2.7$ s and $H_{max} = 1.1$ m.

3.2 Description of the INNWIND Semi-submersible Model

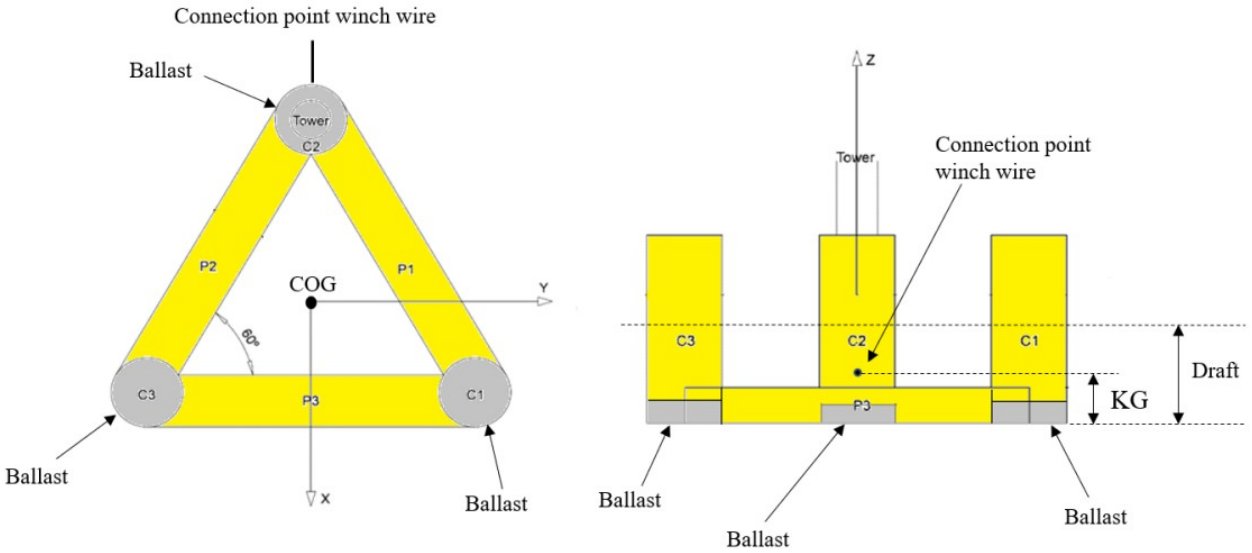


Figure 3.21: INNWIND Model Schematic adapted from (Sandner et al., 2015).

Table 3.9: Description of the INNWIND Semi-submersible Model, updated from Otter (2022).

	Model Scale	Full Scale
Weight empty platform	54 kg	-
Weight tower	5.7 kg	712,500 kg
Weight MPA with loadcell	2.96 kg	-
Weight ballast C1 & C3	37.6 kg	-
Weight ballast C2	29.1 kg	-
Total mass	167.7 kg	20,963,750 kg
KG	0.17 m	8.5 m
GM	0.295 m	14.75 m
Draft	0.36 m	17 m (in salt water)
Diameter columns	0.29 m	14.5 m
Depth columns	0.75 m	37.5 m
Width columns	0.2175 m	10.875 m
Depth pontoons	0.14 m	7 m
Distance between columns	1.32 m	66 m
Hub height (from SWL)	1.82 m	90 m (in salt water)
Roll moment of inertia	72.481 kg m^2	22,650,180,300 kg m^2
Pitch moment of inertia	73.413 kg m^2	22,941,478,633 kg m^2
Yaw moment of inertia	88.849 kg m^2	27,765,273,191 kg m^2

3.3 SIL Test Setup

The setup of the moored INNWIND model for SIL testing in the DOB is presented in Figure 3.22. Reflective markers needed for the Qualisys motion tracking system are attached on top of the port and starboard columns and the bottom and middle of the aluminium tower.

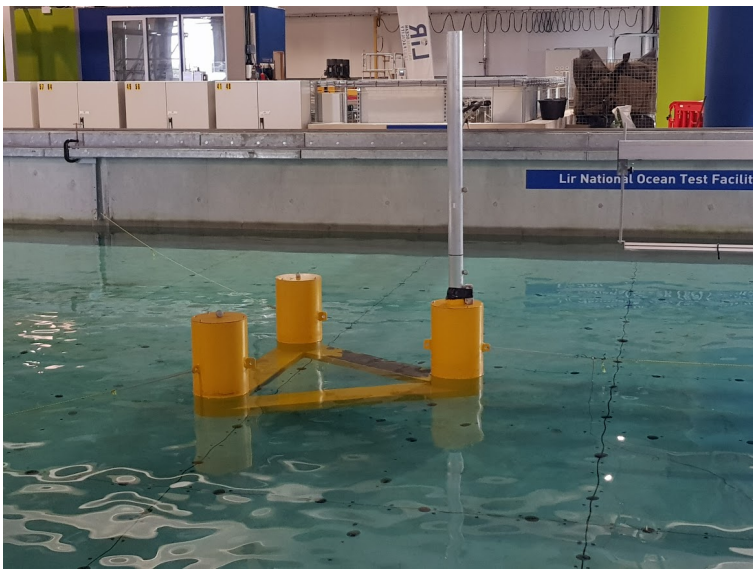


Figure 3.22: Moored INNWIND model in the DOB.

3.3.1 SIL - Mooring Design

As the focus of this thesis is the emulation of current loads through a winch actuator system, the decision was made to maintain the previous mooring system used by Otter (2022) in the initial actuator testing phase. This choice aimed to prevent uncertainty in the platform's motion response during the testing presented. The mooring system consists of 3 mooring lines (ML), in a 120 ° spread, attached to each column at KG as per Figure 3.21. An initial pretension of 9 N was imposed on the mooring system. This was achieved by setting the tension of ML2 to 9 N, obtained from the load cell, and attaching ML1 and ML3 to replicate this spring deflection for the other springs. Adjustments were made to ensure the model was centred and that the line of action of the 3 mooring lines coincided with the model COG in the XY plane. To ensure similarity between the mooring system presented and that of Otter (2022), spring calibration and free decay tests were conducted.

3.3.2 SIL - Emulation of Current Loads

The winch system consists of two servo-drive systems. Winch 1 consists of an LXM28A drive, with a Schneider BCH2MM152 1.5 kW servo motor, while Winch 2 uses an LXM28A drive with a BCH2LD043 400 W servo motor. Table 3.10 contains the relevant specifications of both drives and motors. As a servo motor, the system contains an encoder that measures the rotational angle, speed and distance of the motor which is fed back to the motor to update its response. An internal PID controller ensures the error between the demanded and measured response is reduced. The 445 N Futek load cell used for C_d testing was replaced with a 44.5 N load cell when switching to the LabVIEW setup for SIL testing.

Table 3.10: Specifications of the servo-drive systems (Schneider Electric, 2022).

Technical Data - General	Winch 1	Winch 2
LXM28A Current (mA)	7	2.6
Continuous stall torque, M_0 (Nm)	7.16	1.27
Peak torque, M_{max} (Nm)	21.48	3.81
Nominal speed of rotation, n_N (rpm)	2000	3000
Nominal torque, M_N (Nm)	7.16	1.27
Nominal current, I_N (A_{rms})	6.74	2.5
Nominal power, P_N (kW)	1.50	0.4
Technical Data - Mechanical	**Winch 1**	**Winch 2**
Maximum permissible speed of rotation, n_{max}, (rpm)	3000	5000
Rotor inertia without brake, J_M (kgcm^2)	9.7	0.27
Product weight, m (kg)	8.6	2.1
Shaft diameter, (mm)	22	14
Shaft length, (mm)	55	30
Key width, (mm)	8	5

3.3.3 SIL - Process Control Design

The SIL method of Otter (2022) was employed, using a Simulink model that incorporated a PI controller and Qualisys real-time tracking (Figure 3.23). Qualisys is a motion tracking system consisting of numerous cameras positioned around the DOB that provides the displacement of a rigid body in each degree of freedom. The platform motion is combined with the Morison equation (equation 2.7) to derive a demanded tension for the winch line equating to the current drag force. Using the load cell to provide a measured tension, the PI controller adjusts the signal to the winch to reach this demanded tension. A distinction is used to differentiate tests conducted with constant demanded Tension (TSIL), from those that use real-time Qualisys tracking to update the demanded tension (QSIL).

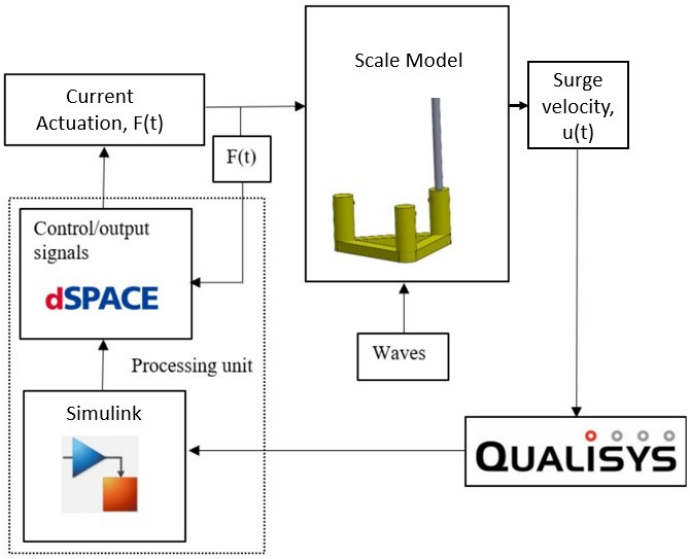


Figure 3.23: Hardware control layout of the current only system, adapted from Otter (2022).

Figure 3.24 displays the Simulink model for the current-only case with a single winch. A Simulink function is used to define the drag coefficient, C_d, based on the results from the tow tank tests as per section 4.1. The only difference between the TSIL and QSIL systems is the value of platform surge velocity u. For TSIL this remains a constant, while for QSIL this value is updated at 32 Hz via the file "Cillian_winch.m" (Appendix A). This file enables communication between the Qualisys host computer and the computer hosting the dSPACE processor.

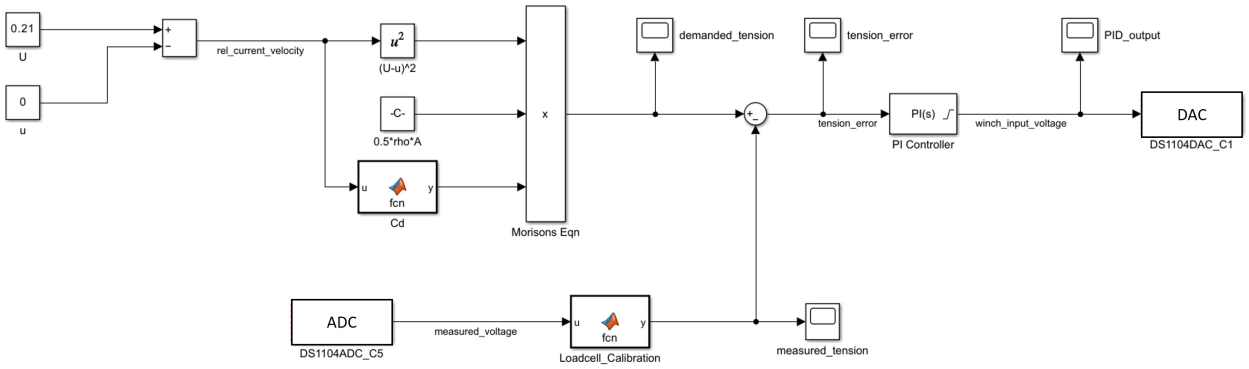


Figure 3.24: Single winch, current-only Simulink model.

Initially, a LabVIEW system was developed for the TSIL tests, to enable the winch to respond to the tension in the winch line (Appendix B). A PI controller was implemented to tune the winch response. Safety limits were applied to the winch output voltage, as the maximum output of the 1.5 kW motor exceeded the needs for this campaign. While the system worked for the TSIL tests, the network firewall restricted the transfer of the Qualisys data across the network from one PC to another therefore, due to time limitations, we reverted to the dSPACE system for the QSIL tests.

The dSPACE system operates similarly to LabVIEW but uses a direct implementation of the Simulink model from Figure 3.24. ControlDesk is the software that connects the user to the real-time simulation via the dSPACE processor. Once changes have been made in Simulink, the Simulink file can be compiled into C+ code making it compatible with implementation in ControlDesk by using ctrl + b. ControlDesk contains the ability to enable real-time altering of the Simulink code variables. Figure 3.25 displays QSIL testing with Current B (U), real-time surge velocity (u), PI tuning settings and load cell response.

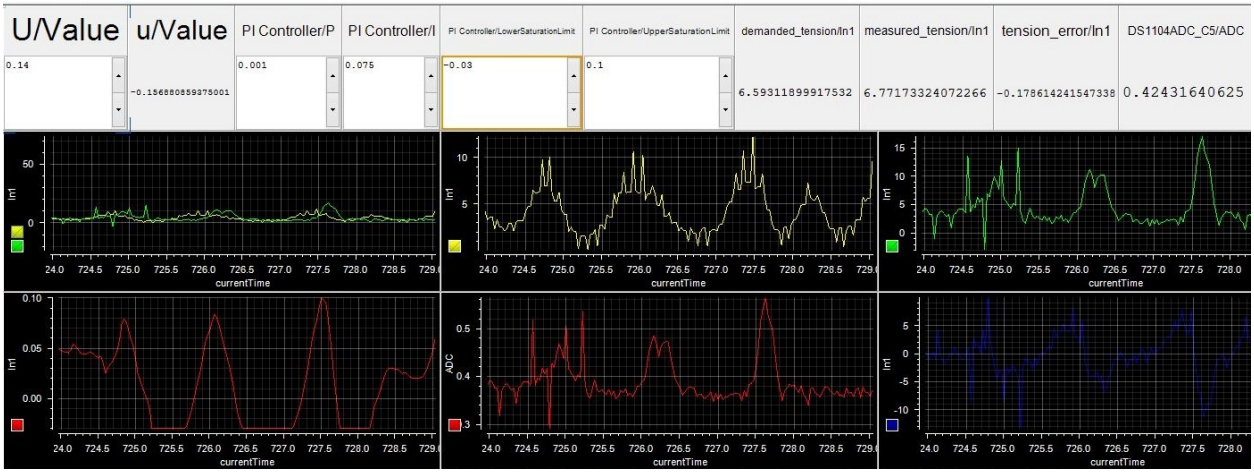


Figure 3.25: ControlDesk layout of the single winch system.

3.3.3.1 SIL - Proposed Simulink code for Dual-Winch System

Introducing a second winch requires alterations to the Simulink model to account for the process interactions of the winch lines. The demanded tensions of each line are altered to be a function of the current incidence angle, by resolving the force vector triangles of the winch lines. The resultant forces for each line are sent to individual PI controllers. As discussed in section 2.4, to reduce unwanted interaction between the winches, decoupling blocks D_{12} and D_{21} are installed in each branch in the Simulink code. A proposed methodology for tuning the decoupling blocks is found in section 4.2.6.

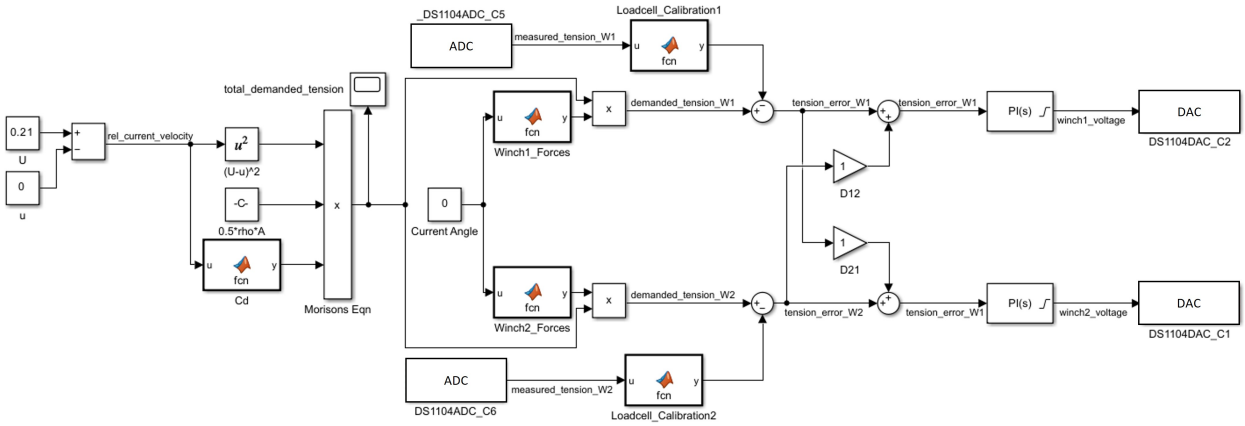


Figure 3.26: Double winch, current-only Simulink model.

3.3.4 SIL - Hardware Layout for Single- and Dual-Winch Systems

The proposed hardware layout for the dual-winch system enables current emulation for a range of incidence angles (Figure 3.28). Testing for the single winch system using winch 1 (W1) and line 1 (L1) only has been conducted during this thesis. The combination of two winches poses further challenges due to the cross-coupling of each winch as mentioned in section 2.4. Due to unforeseen delays in the assembly of the second winch, a two-winch system was not tested as part of this research, however, the proposed layout was developed.

Table 3.11 outlines the lines, winches and pulleys used for each current incidence angle. Each line is connected to the platform at the height KG, as per Table 3.9, to mitigate unwanted pitch motions of the platform. As displayed in Figure 3.27, P1 has an upper pulley located in line with W1, and a submerged lower pulley at KG. A similar configuration will be required for P2, P3 and P4.

Table 3.11: Two-winch system layout configurations.

Current Angle (°)	Lines	Winches	Pulleys
0	L2', L3	W1, W2	P1 - P2, P3 - P4
45	L2', L3	W1, W2	P1 - P2, P3 - P4
90	L1, L2	W1, W2	P1, P2 - P3
135	L1, L2	W1, W2	P1, P2 - P3
180	L1	W1	P1
225	L1, L3	W1, W2	P1, P3 - P4
270	L1, L3	W1, W2	P1, P3 - P4
315	L2', L3	W1, W2	P1 - P2, P3 - P4

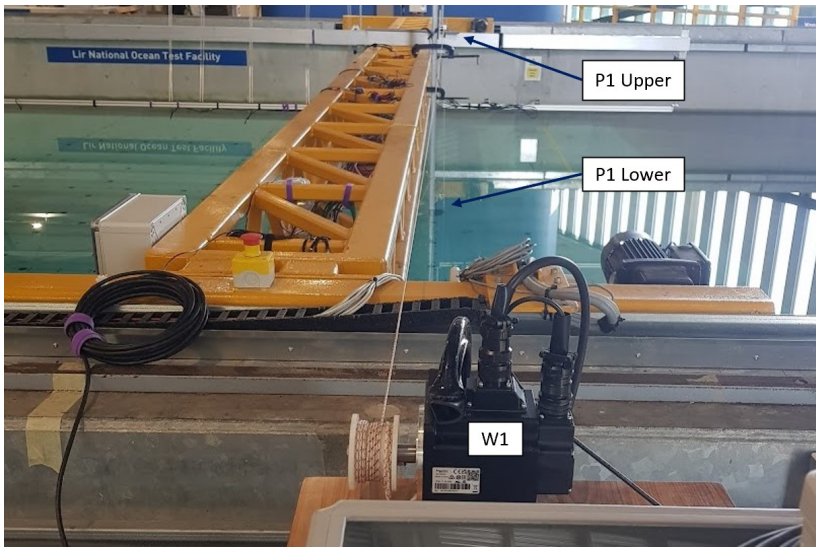


Figure 3.27: W1 at the edge of the DOB. Note that P1 lower is submerged.

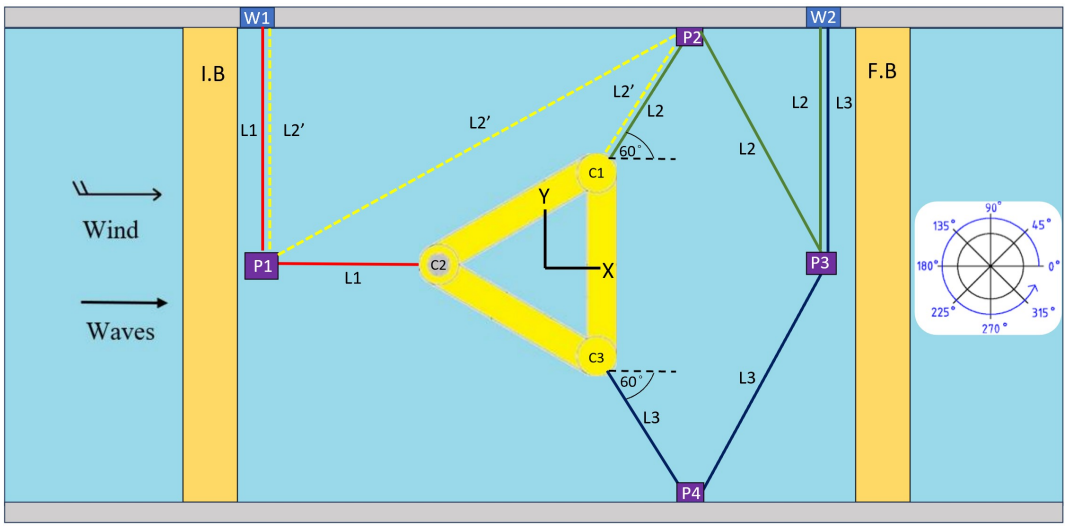


Figure 3.28: Schematic of the dual-winch system in the DOB.

3.4 Ansys AQWA Simulation Setup

Ansys AQWA is a toolbox of Ansys Inc. that enables the analysis of marine structures and their surrounding fluid (Ansys, 2016). As part of the validation of the winch actuator system for this research, simulations with various environmental conditions (waves and current) were conducted in AQWA at the model scale. The decision to use a model scale for AQWA was chosen on account of several factors. Due to the adaptations made to the ballast and tower height by Otter (2022) to pair the INNWIND model with a 5 MW turbine, the only comparable experimental data of this platform is that of Otter (2022). As a result, AQWA was used to "model the model". Furthermore, the reduction of computational power required for a model scale simulation enabled simulations to be conducted on a mid-range laptop with 16 GB of RAM and an Intel i7 2.3 GHz processor.

The model water geometry resembles the DOB at the Lir NOTF, with a basin length of 35 m, width of 12 m and depth of 3 m. No wave absorption methods were used in the AQWA

model to replicate the DOB beach of the DOB as no clear guidance in the literature could be obtained regarding this. A SolidWorks .stl file of the scale model, with dimensions as per Table 3.9 was imported into Ansys Workbench. Ansys SpaceClaim was utilised to split the model into separate surfaces above and below the waterline. A point mass was added to the COG of the geometry with the moment of inertia values from Table 3.9. The mesh size was determined through an iterative process. The initial panel mesh size was obtained from Otter (2022), which was 3 m (0.6 m in model scale). Using this as a starting point, a mesh sensitivity study was conducted to determine the most efficient mesh, three sizes, 0.015 m, 0.025 m and 0.06 m were chosen. The 0.025 m mesh returned a similar response to the 0.015 m mesh in terms of RAO natural frequency and magnitude. As the 0.025 m mesh required only 7762 elements compared to the 21648 of the fine mesh, it was selected as a suitable balance between accuracy and efficiency (Figure 3.29). Figure 3.30 displays the mooring lines attached to each column, in a 120-degree circular pattern to ensure the force vectors intersect at the platform COG. Fixed points were used to represent the anchor locations in the DOB, while connection points were were used on the semisub, at the fairlead positions. A cable attachment was used to represent the mooring lines, with a stiffness of 19 N/m. The same cable attachment type was used for the winch, with the stiffness set to 200 N/m. Also visible is the wave probe location, 2 m to the right of the platform and the winch attachment locations on each column, below the mooring attachments. A hydrodynamic diffraction block was implemented to calculate the platform hydrostatics and response to numerous wave directions and frequencies in the frequency domain. Table 3.12 shows the volumetric displacement of water is 0.165 m^3, equating to a platform mass of 165 kg, 2.7 kg less than that defined in Table 3.9. The metacentric height (GM) of AQWA and Table 3.9 demonstrate considerable agreement.

Currents A, B, C and D were added to the system using the Current Force Coefficients (CFC) in the geometry tree. These are included to represent the viscous hull drag exerted on the platform. Defined as the force per unit velocity squared ($N/(m/s)^2$)), these were defined using the drag force and velocity data from the towing drag coefficient tests described in section 4.1. Tests were conducted in AQWA to replicate the test conditions in the DOB testing, using a combination of irregular JONSWAP waves and currents.

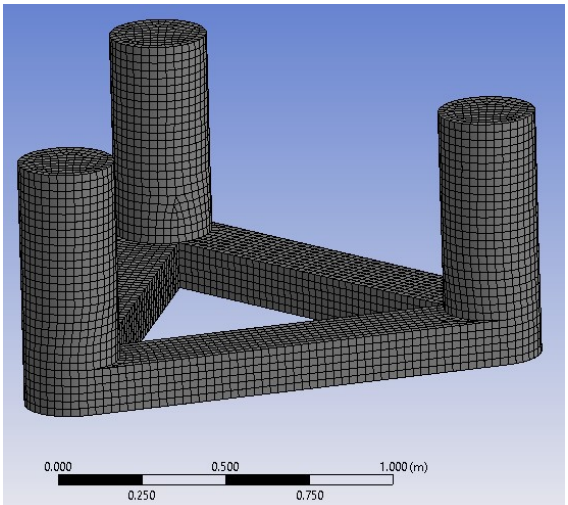


Figure 3.29: Mesh of the INNWIND semi-submersible model in AQWA.

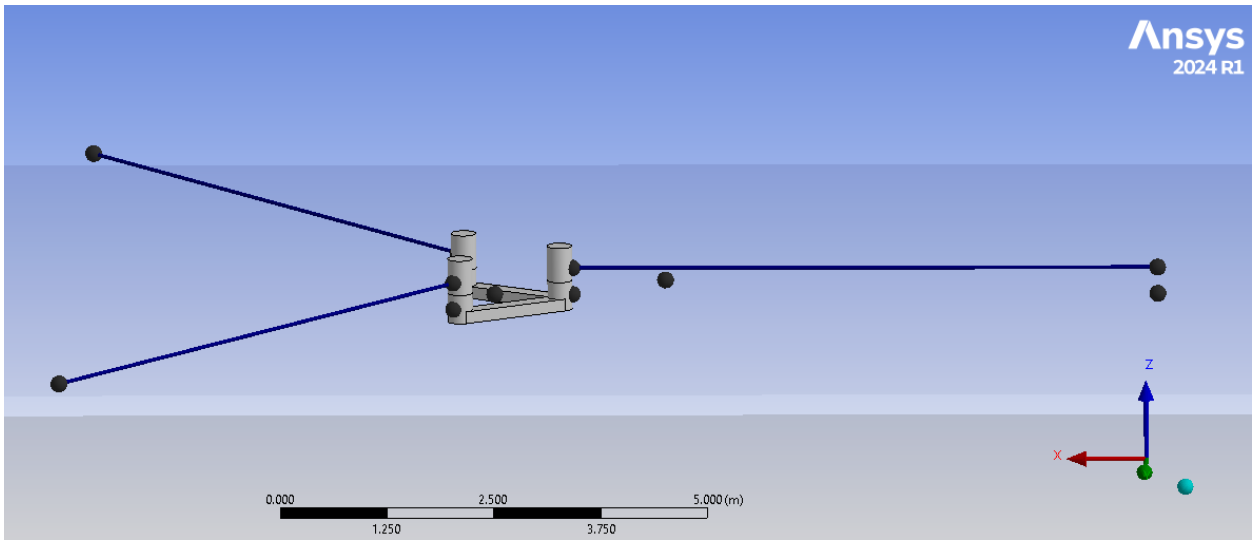


Figure 3.30: Model in the DOB basin with mooring lines, attachment points and wave probe location visible.

Table 3.12: Hydrostatic results of the INNWIND model in AQWA

Hydrostatic Stiffness			
Center of Gravity (CoG) Position:	X: 0.000 m	Y: 0.000 m	Z: -0.17 m
	Z	**RX**	**RY**
Heave (Z):	1967.617 N/m	-0.005 N/°	-0.065 N/°
Roll (RX):	-0.288 N.m/m	8.449 N.m/°	0.002 N.m/°
Pitch (RY):	-3.700 N.m/m	0.002 N.m/°	8.399 N.m/°
Hydrostatic Displacement Properties			
Actual Volumetric Displacement:	0.165 m^3		
Equivalent Volumetric Displacement:	0.164 m^3		
Cut Water Plane Properties			
Cut Water Plane Area:	0.196 m^2		
Center of Flotation:	X: 0.002 m	Y: -0.000 m	
Principal 2nd Moments of Area:	X: 0.058 m^4	Y: 0.058 m^4	
Small Angle Stability Parameters *with respect to Principal Axes*			
CoG to CoB (BG):	0.060 m		
Metacentric Heights (GMX/GMY):	0.290 m	0.291 m	
CoB to Metacentre (BMX/BMY):	0.349 m	0.351 m	
Restoring Moments (MX/MY):	8.399 N.m/°	8.449 N.m/°	

3.5 Test Plan

This test plan outlines a series of experiments to assess the performance of FOWT models under varying environmental conditions. Key tests include evaluating the models in different wave spectra and current velocities to simulate real-world ocean environments. The wave conditions follow the JONSWAP spectrum, and both current-only and combined wave-current scenarios are tested using TSIL and QSIL systems.

Table 3.13: Summary of primary environmental loads used during testing.

Load	Description	Model Scale	Full scale
Wave	JONSWAP 1	$T_p = 1.34$ s, $H_s = 0.1$ m	$T_p = 9.5$ s, $H_s = 5$ m
	JONSWAP 2	$T_p = 1.98$ s, $H_s = 0.25$ m	$T_p = 14$ s, $H_s = 12.5$ m
Current	A	0.11 m/s	0.75 m/s
	B	0.14 m/s	1.00 m/s
	C	0.21 m/s	1.50 m/s
	D	0.28 m/s	2.00 m/s

Table 3.14: Wave Conditions used in the RAO tests. T_p is the wave period, H_s is the significant wave height and γ is the peak enhancement factor.

Test	Wave Spectrum	$T_p(s)$	$H_s(m)$	$\gamma(-)$
RAO1	JONSWAP 1	1.34	0.1	3
RAO2	JONSWAP 1B	0.8	0.1	3
RAO3	JONSWAP 1C	1.8	0.1	3
RAO4	JONSWAP 1D	2.3	0.1	3
RAO5	JONSWAP 1E	2.8	0.1	3
RAO6	JONSWAP 1F	3.3	0.1	3
RAO7	JONSWAP 1G	3.8	0.1	3
RAO8	JONSWAP 1H	1.34	0.2	3
RAO9	JONSWAP 2	1.98	0.25	3
RAO10	JONSWAP 2B	1.98	0.1	3
RAO11	JONSWAP 2C	1.98	0.3	3
RAO12	JONSWAP 2D	1.98	0.25	1

Table 3.15: Current-only testing in the DOB.

Test	Current	Method
C1	A	TSIL
C2	B	TSIL
C3	C	TSIL
C4	D	TSIL

Table 3.16: Wave and Current testing in the DOB. Note adapted JONSWAP waves used to account for wave-current interactions.

Test	Wave	Current	Method
WC1	JONSWAP1_CurrentB	B	QSIL
WC2	JONSWAP1_CurrentC	C	TSIL
WC3	JONSWAP1_CurrentC	C	QSIL
WC4	JONSWAP1_CurrentD	D	QSIL
WC5	JONSWAP2_CurrentA	A	TSIL
WC6	JONSWAP2_CurrentA	A	QSIL
WC7	JONSWAP2_CurrentB	B	QSIL
WC8	JONSWAP2_CurrentC	C	TSIL
WC9	JONSWAP2_CurrentC	C	QSIL
WC10	JONSWAP2_CurrentD	D	QSIL

Chapter 4 - Methodology

The following summary explains the necessary methodology to develop an accurate single-winch actuation SIL system. For the dual-winch system, a further step is required for the tuning of the Simulink code as outlined in section 4.2.6:

1. Initial hydrodynamic coefficient testing of the platform is required to determine the C_d of the model. This is used in the Morison equation to apply a demanded tension force to the winch. Both tow-test and physical current resistance test methodologies are presented.

2. Validation of the model setup for SIL testing through spring calibration, RAO tests and free decay tests is required.

3. The C_d obtained in step 1 is applied to a Simulink function as outlined in section 3.3.3.

4. Preliminary tests are conducted with a range of wave and current loads to tune the PI controller. It is advised to use the TSIL system for this stage to simplify the process.

5. Adaptations to the desired waves from the test plan to account for wave-current interactions are required.

6. Once the PI controller is tuned adequately, the test plan can commence, using both the TSIL and QSIL systems.

4.1 Hydrodynamic Coefficient Test Methodology

To model accurate kinematics of a floating platform's response under environmental loading, evaluation of the hydrodynamic drag coefficient is required. Two methods of drag coefficient testing were used: tow testing and physical current testing. Two models were used in the experiments, the INNWIND Semi-submersible platform and the OE Buoy wave energy converter. The purpose of this testing is to evaluate the strengths and weaknesses of each testing method for platform testing at Lir NOTF.

Tow testing in still water was carried out in the Deep Ocean Basin (DOB), by attaching the platforms to the instrument bridge with a rope. A Futek 445 N load cell was installed in the tow rope to measure the drag force (Figure 5.34). The tow rope is attached at the centre of gravity of the platform to prevent a pitch-induced response and to prevent yawing during towing. Qualisys motion tracking system was used to validate that the bridge tow speed matches the set value, as well as tracking the rotational motion of the OE Buoy model. The tests were run at bridge speeds of between 0.1 - 0.7 m/s in increments of 0.04 m/s. For select speeds, repeatability tests were conducted to determine the precision of the instrument bridge as a testing method.

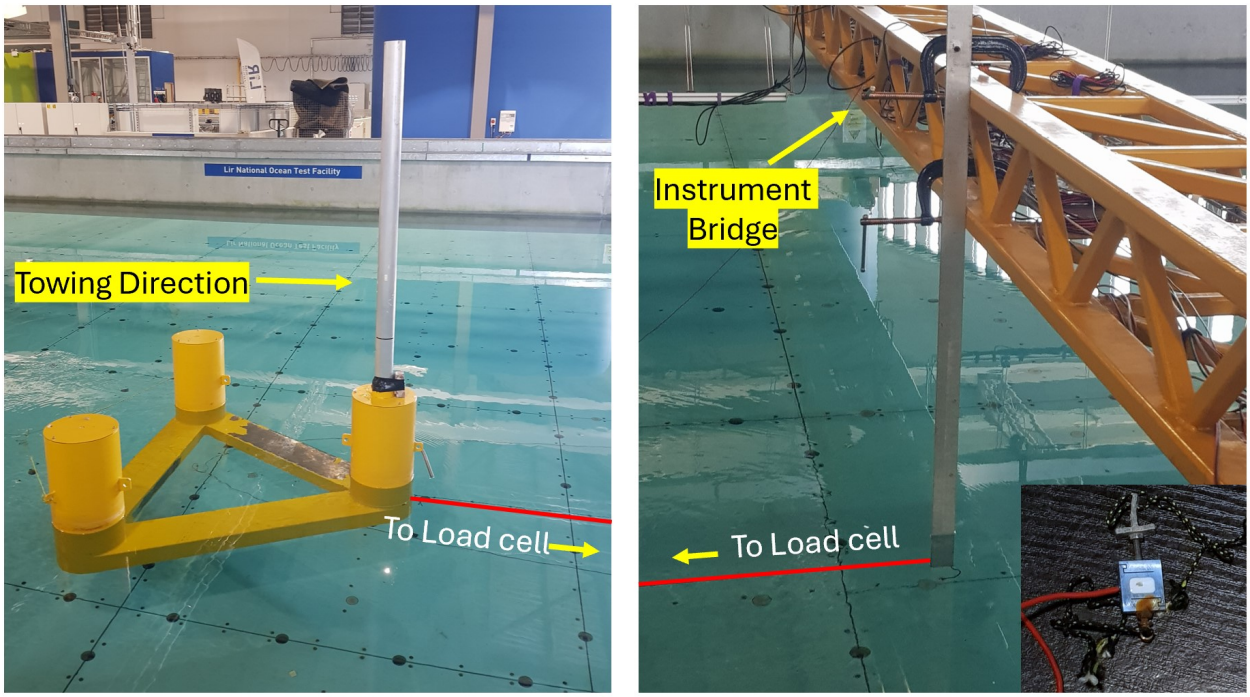


Figure 4.31: (a) INNWINDEU semi-sub in the DOB with tow rope attached at COG. (b) Instrument bridge with towrope attached, Futek 445 N Load cell (inset).

Physical current testing was conducted in the Wave Current Flume (WCF), with the platforms fixed in the surge direction and exposed to a current flow (Figure 4.32). An Aquadopp 2 MHz current profiler was used to determine the velocity of the flow. The profiler was placed on the floor of the flume, with readings beginning 0.3 m from the floor to the water surface, which was 0.83 m above the flume floor for this experiment. This enabled a current velocity with an accuracy of $\pm$ 1 % to be obtained for use in the Morison equation (2.7). Similar to the tow testing, a load cell was attached between the platform and a fixed point in the WCF to measure the drag force exerted on the platform. Tests were conducted using physically applied current.

The thrusters were increased from 10 - 70 % in increments of 5 % to obtain a velocity profile of the flow. Initially, a 10-second average was used on the Aquadopp readings, over a 120-second runtime. This was later altered due to poor velocity readings, to a 20-second average. As a result of the poor velocity readings obtained by the Aquadopp, manual velocity measurements were taken by tracking the time taken for a flotation device to travel a measured distance along the length of the WCF.

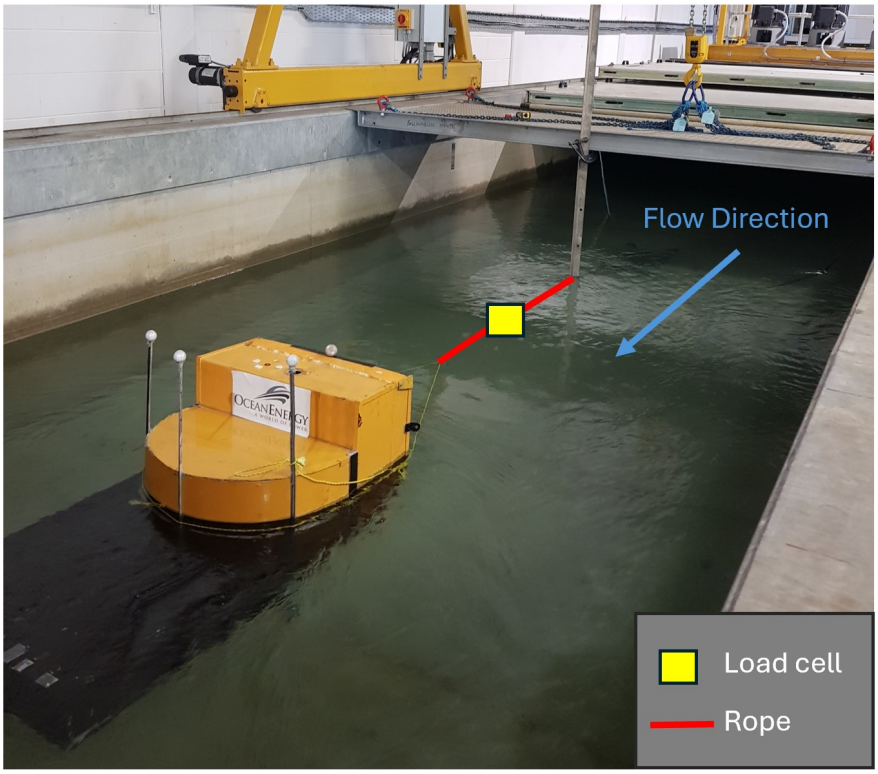


Figure 4.32: OE Buoy in the WCF with rope and load cell attached.

4.2 SIL Testing Methodology

In order to conduct a comprehensive SIL testing campaign, preliminary validation tests were required to give confidence in the model validation. Spring calibration, free-decay and RAO tests were conducted to validate the hydrodynamic model in the DOB, while process control testing was conducted to ensure adequate winch control tuning was utilised.

4.2.1 Spring Calibration

Validation of the springs to be used in the mooring lines and winch lines was conducted through a spring displacement test by attaching increasing weights and measuring the resulting displacement of the spring. 19 N/m mooring line springs and 265 N/m winch line springs were ordered to match the system used in Otter (2022) to remove uncertainties in the test results. Table 4.17 displays the corresponding results for the average of six mooring springs tested, also seen in Figure 4.33 (a). The actual spring stiffness was found to be 22.93 N/m, this is seen as an acceptable margin from the desired 19 N/m and is not expected to have a large impact on the platform's response. Similarly, the winch spring stiffness was found to be 263 N/m, again acceptable compared to the 265 N/m spring used by Otter (2022) to avoid snap loads in the winch line. While the linear trendline for both springs do not pass through the origin as expected, the mooring lines are pre-tensioned to 9 N, reducing the effects of this discrepancy.

Table 4.17: Spring displacement test results for mooring springs.

Weight (kg)	Force (N)	Length (m)	Displacement (m)
0.00	0.00	0.12	0.00
0.278	2.73	0.18	0.06
0.528	5.18	0.29	0.17
0.778	7.63	0.40	0.28
1.028	10.09	0.52	0.40
1.278	12.54	0.62	0.50
1.528	14.99	0.75	0.63

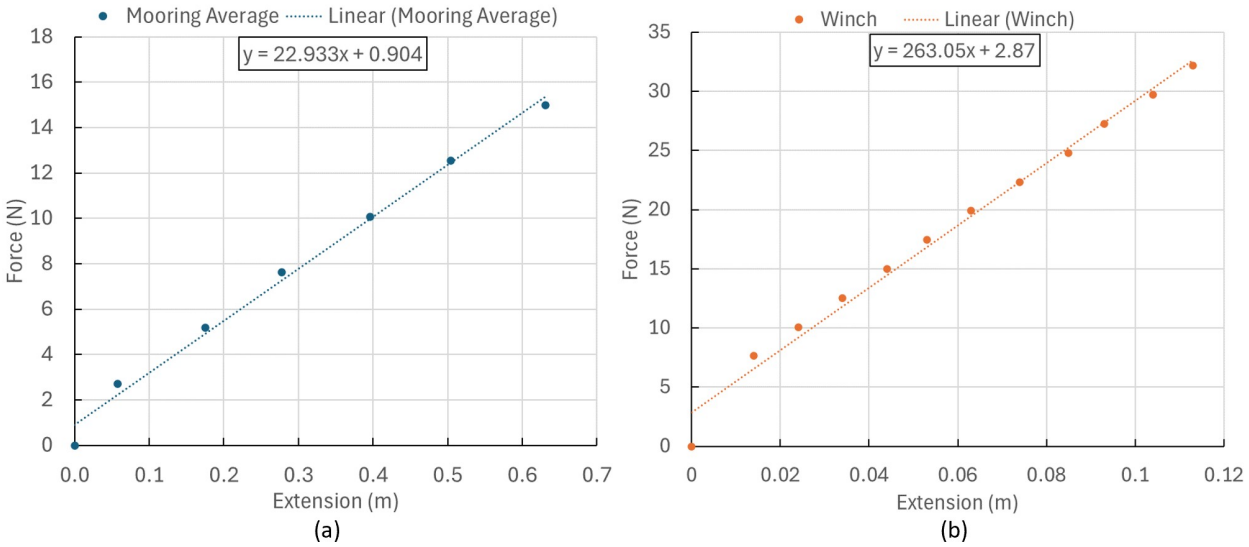


Figure 4.33: Force - displacement graphs of both Mooring (a) and Winch (b) springs.

4.2.2 Decay Test

Decay tests of the moored INNWIND model were conducted in the DOB to assess the stability of the model and to create a reference to validate the Ansys AQWA model. The decay tests were conducted manually by personnel in the tank displacing the platform from equilibrium in one of the 6 DOF's before releasing the platform and allowing the model to decay to equilibrium. Each DOF was allotted 300 s to enable the test to be conducted multiple times.

The natural periods of each DOF are obtained using the Qualisys motion response data and the logarithmic decrement method, denoted by δ (Inman and Singh, 2007):

$$\delta = ln\frac{x(t)}{x(t+T)} \tag{4.19}$$

where T is the period of oscillation. The peaks $x(t)$ and $x(t+T)$ are obtained using the MATLAB Signal Analyzer Toolbox. The damping ratio ζ determines if the system is underdamped ($\zeta < 1$), critically damped ($\zeta = 1$) or overdamped ($\zeta > 1$) and can be obtained by:

$$\zeta = \frac{\delta}{\sqrt{4\pi^2 + \delta^2}} \tag{4.20}$$

The natural frequency of the system, ω_n is:

$$\omega_n = \frac{\delta}{\zeta T}\ (rad/s) \tag{4.21}$$

Therefore, the natural periods for each DOF are determined by:

$$f_n = \frac{\omega_n}{2\pi}\ (Hz), \quad T_n = \frac{1}{f_n}\ (s) \tag{4.22}$$

4.2.3 Response Amplitude Operator (RAO) Testing

The RAO of a platform is defined as the ratio of a platform's response to original input. RAOs are calculated for all degrees of freedom for different wave conditions. The RAOs of the INNWIND model were obtained through Ansys AQWA initially and later with experimental tests in the DOB for a range of wave conditions (Table 3.14). To conduct the RAO analysis, the wave elevation is recorded using the wave probes in the DOB tank and the platform motions are tracked using Qualisys. The wave probe collects data at 128 Hz, while Qualisys tracks the motion at 32 Hz, therefore averaging of the wave probe data is required to ensure the time intervals of both series were equivalent. A MATLAB code was compiled making use of the *pwelch* and *cpsd* functions that calculate the power spectral density (PSD) and cross-spectral density (CSD) respectively. PSD is derived from the wave input x(t), while CSD is derived from the response of the platform y(t) to the wave input x(t). The transfer function of these densities, defined as the ratio of output response to a given input, is commonly referred to as the Response Amplitude Operator in marine applications (Ramachandran et al., 2013):

$$RAO = \frac{S_{xy}(\omega)}{S_{xx}(\omega)} \tag{4.23}$$

where $S_{xy}(\omega)$ and $S_{xx}(\omega)$ are the cross-spectral and power spectral densities as a function of frequency.

4.2.4 Wave-Current Interaction Procedure

Wave-current interactions, as outlined in section 2.2.4 alter the wavelength and period of a wave depending on the interaction angle. Testing conducted throughout this thesis consisted of waves and currents directly opposing each other. An iterative approach is required to determine the wavelength and wave number of the waves. Using equations 2.9 and 2.6 from section 2.2.2, an iterative approach was used to find λ. Excels, *goal seek* function was employed to aid the iteration calculations:

$$\lambda = \frac{g(T_p)^2}{2\pi} \cdot tanh\left(\frac{2\pi h}{\lambda}\right) \tag{4.24}$$

The wave number, k was required for the wave-current interaction calculations as outlined in section 2.2.4. The unaltered wave number, k could now be obtained from equation 2.8

using the derived λ from above. A simplified approach to the wave-current alterations was used in comparison with that of Draycott et al. (2018). Adjusted wave amplitudes, A_I and wavelengths ω_r only were used, and the frequency spectra were not changed in their entirety. This resulted in updated H_s and T_p values only for the JONSWAP spectrum when current is present. The updated wave number, k_I is found by iterating the following equation:

$$k_I^2 U^2 + k_I(2U\omega - gtanh(k_I h)) + \omega^2 = 0 \tag{4.25}$$

4.2.5 SIL Testing Procedure

The following procedure should be followed when using either the TSIL or QSIL system:

1. Ensure the DOB water is still and the model is centred in the tank.
2. Turn on the winch and all host computers. Arm the wavemaker if waves are required.
3. TSIL: Begin Qualisys tracking to record the platform motion. For current-only tests using TSIL, begin recording on dSPACE and input a current velocity to generate a demanded tension. For current and wave tests, repeat the above, however, apply an adapted wave file using the Wavemaker PC to match the desired current velocity. Begin the waves and currents simultaneously and run to completion.
4. QSIL: Begin Qualisys tracking to record platform motion. Go online in dSPACE. Start the MATLAB file to transfer Qualisys surge velocity readings to dSPACE. begin recording on dSPACE and input a current velocity to generate a demanded tension. For current and wave tests, repeat the above, however, apply an adapted wave file using the Wavemaker PC to match the desired current velocity. Begin the waves and currents simultaneously and run to completion.

4.2.6 Proposed Dual-Winch System Simulink Tuning Methodology

A proposed method for tuning the decoupling gains in the Simulink code to minimise process interactions is outlined below:

1. Tune the PI controller of both winches independently through empirical testing for a range of demanded tensions.
2. Using the PI settings derived above, set a current velocity to generate a demanded tension for both winches. This test requires a current incidence angle that uses both winches (Table 3.11).
3. By altering the Simulink code, manually set one winch to maintain a demanded tension of 0 N (passive winch), while leaving the remaining winch connected to the Winch_Forces function (active winch).
4. Set D_{12} and D_{21} equal to 1 for this test to turn off decoupling. Begin current actuation with both winches and record the demanded and measured tensions for both.

5. Compare the response of the active winch, to a test with the same current velocity from step 1. Discrepancies between these tests demonstrate the effect the passive winch has on the active winch. Similarly, deviation from 0 N of the passive winch will demonstrate the effect the active winch has on the passive winch.

6. The process interaction gains, G_{p21} and G_{p12} can be estimated from these tests by measuring the ratio of the output to input for each winch.

7. Initial estimations for the values of D_{12} and D_{21} can be found using equation 2.17.

8. Repeat steps 2 - 5 with the values of D_{12} and D_{21} updated.

9. Continue testing for a range of current incidence angles and velocities to obtain a wider scope of the interactions in the system.

4.3 Assumptions, Simplifications and Sources of Error

To clarify the limitations and scope of this work, the following assumptions, simplifications and sources of error are outlined for the methodology used throughout testing. Beginning with the assumptions:

- During hydrodynamic drag testing in the DOB, the platforms are assumed to be pulled directly in line with the tow rope, with yaw, pitch and roll effects neglected. As a result, the force from the load cell is assumed to be in the surge direction only.
- The drag coefficient determined from the towing and physical current tests was obtained to determine the discrepancies between the two methods and is not a finite method of determining C_d for a floating platform. The values are assumed to be correct when used in AQWA simulations and SIL testing.
- The current is assumed to be uniform and steady throughout the water column.
- The addition of an equivalent weight to the MPA used by Otter (2022) is positioned on top of column C2 to maintain the overall system weight. The positioning of this weight is assumed to have minimal influence on the platform response.
- The projected area, A, used in the Morison equation is unchanged throughout testing, despite dynamic changes in pitch and heave motions altering this value.
- The force vector of the winch line is assumed to act along the XY plane of the model at all times. Small angles between the winch line and the XY plane may be present during wave conditions where large pitch and heave motions occur.
- Alterations to the JONSWAP wave spectra for wave-current conditions using the winch as outlined in section 2.2.4 are assumed to be equivalent to the wave alterations due to physical wave-current interactions.
- When comparing C_d values between the WCF and DOB for the semi-sub, the velocities of Otter (2022) are assumed to be correct and obtained in a similar flow regime to the values of the load cell obtained during this testing.

The following simplifications have been made:

- Radiation and diffraction effects of the body are ignored in the Morison equation. The C_d values obtained are not frequency dependent.
- Waves and current travel in opposing directions in all tests.
- No hydrodynamic loading of the mooring lines is included due to the horizontal setup.
- Due to the lack of a functioning wave and current test facility, AQWA simulations are benchmarks for comparison with wave and current tests.
- A decision was made to use wave and current loading only as this thesis's primary focus was optimising the SIL setup.

Possible sources of error are as follows:

- No porosity screen was employed in the WCF C_d test campaign. This may contribute to the differences in the C_d results displayed in this thesis and that of Otter (2022) in the WCF for the INNWIND model.
- Velocity readings in the WCF testing using the Aquadopp profiler were unstable, despite changes made to averaging settings. The repeatability between tests and variance throughout the water column was poor. As a result, a manual speed calculation of a flotation device was employed. Each speed was run multiple times to obtain an average however user error in stopwatch measurements is likely present. The device was positioned next to the WCF wall to ease testing. The current velocity is likely higher in the centre of the WCF where the load cell was positioned.
- Friction in the pulleys, oscillation of the winch line between W1 and P1 and elasticity of the winch line contribute to a delay between the demanded and measured tension. Friction in the lines was mitigated by keeping all bends at right angles. The addition of another pulley between W1 and P1 may dampen the oscillations of the line.
- For current-only tests, the restoring force of the mooring system is not large enough to return the platform to its initial position when the winch is unwinding. As a result, the influence of the mooring decays slowly over a long period, introducing oscillations to the demanded winch tension. This effect is minimal for current and wave conditions where the wave force restores the platform in the surge direction.
- The Ansys AQWA mesh used is inefficient, with a constant element size across the platform. Increasing the number of refinement layers around the column and pontoon edges, while increasing the element size along the pontoon faces may result in a more accurate, efficient mesh.

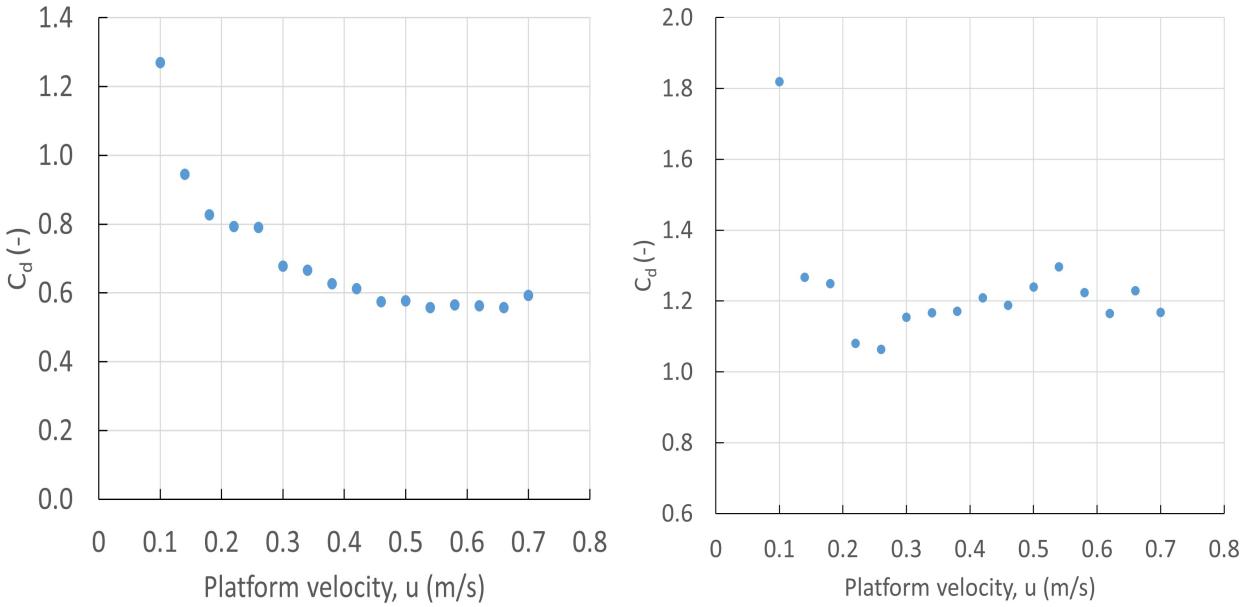
The methodology outlined in this chapter provides a comprehensive framework for conducting both hydrodynamic coefficient testing and SIL testing. These methods are crucial for developing accurate models of FOWTs and validating their performance under various environmental conditions. Chapter 5 contains the initial model setup results and tests outlined in section 3.5, offering insights into the performance and behaviour of the tested models.

Chapter 5 - Results & Discussion

This chapter presents the results obtained from the various tests outlined in the previous methodology chapter. The primary focus is hydrodynamic coefficient testing, decay test response, RAO testing and SIL testing. By comparing these findings with theoretical predictions and numerical simulations, we aim to validate the experimental setup and identify areas for improvement.

5.1 Hydrodynamic Coefficient Testing - DOB

Figure 5.34 displays the drag coefficient (C_d) as a function of platform velocity in the surge direction, u, for the semi-sub and OE Buoy models. The semi-sub displays a decreasing C_d as a function of speeds tested, while the OE Buoy remains constant throughout most tests.



(a) (b)

Figure 5.34: C_d from DOB tow testing for (a) Semi-sub (b) OE Buoy

Repeatability tests were conducted for each model to mitigate the short run times due to the length of the tank. Table 5.18 displays the results for the semi-sub, with an average deviation, from the average, of 14.9 % and 6.8 % at 0.18 and 0.3 m/s respectively. Table 5.19 displays the results for the OE Buoy, with an average deviation of 12.1 %, 12.9 % and 2.9 % at tow speeds of 0.18, 0.3 and 0.7 m/s respectively.

Table 5.18: DOB repeatability tests of semi-sub.

0.18 m/s				0.3 m/s			
Run	Force (N)	% Deviation	C_d (-)	Run	Force (N)	% Deviation	C_d (-)
1	6.38	14.13	0.94	1	10.98	13.71	0.59
2	4.73	15.27	0.70	2	12.39	2.57	0.66
3	4.36	21.97	0.65	3	12.62	0.80	0.67
4	6.62	18.53	0.98	4	13.91	9.36	0.74
5	5.84	4.59	0.87	5	13.70	7.72	0.73
Average	5.59	14.90	0.83	Average	12.72	6.83	0.68

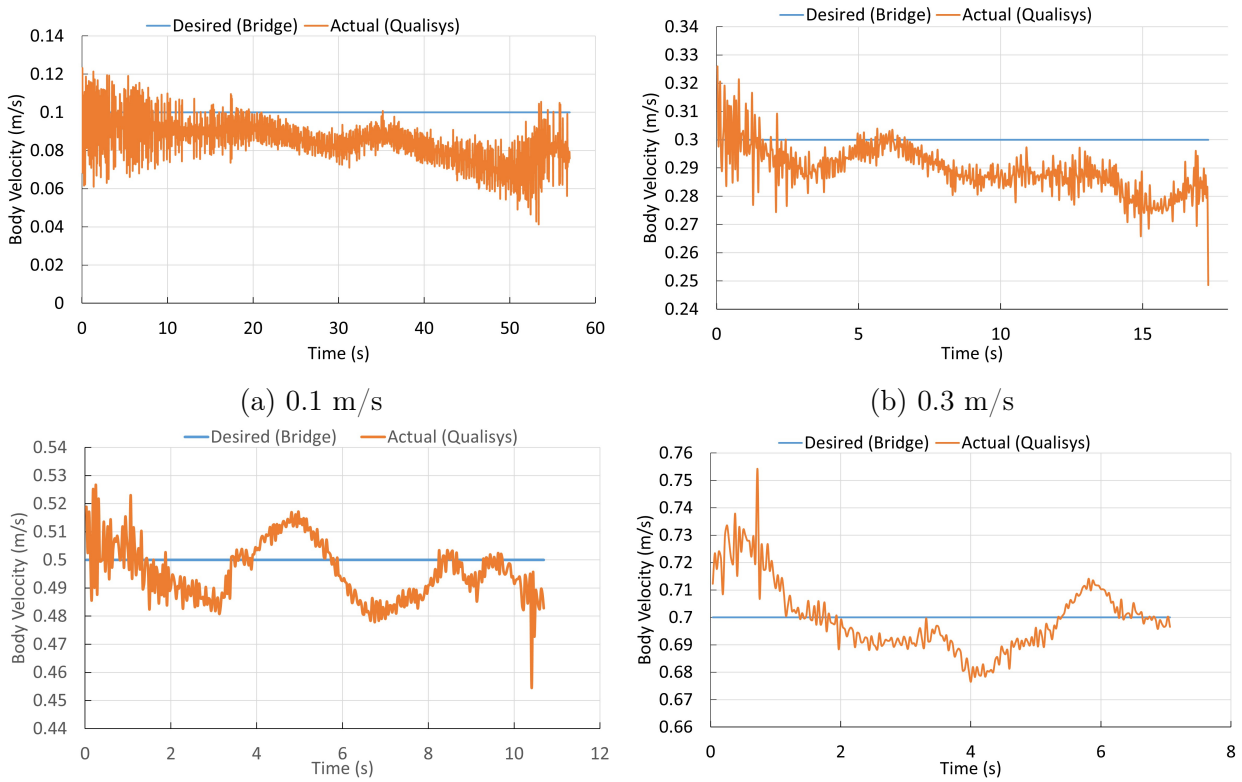
Table 5.19: DOB repeatability tests of OE Buoy.

0.18 m/s				0.3 m/s				0.7 m/s			
Run	Force (N)	% Deviation	C_d (-)	Run	Force (N)	% Deviation	C_d (-)	Run	Force (N)	% Deviation	C_d (-)
1	2.52	30.14	0.87	1	5.83	32.19	0.73	1	50.95	4.90	1.17
2	3.77	4.59	1.31	2	9.25	7.55	1.15	2	54.77	2.23	1.26
3	4.09	13.61	1.42	3	9.70	12.83	1.21	3	52.35	2.27	1.20
4	3.79	5.12	1.31	4	9.13	6.16	1.14	4	54.72	2.14	1.25
5	3.85	6.82	1.33	5	9.09	5.65	1.13	5	55.08	2.80	1.26
Average	3.60	12.06	1.25	Average	8.60	12.88	1.07	Average	53.57	2.87	1.23

Figure 5.35 displays a close correlation between the velocities recorded by Qualisys and the set velocities of the instrument bridge, with spikes of less than 10 % evident for most cases. Table 5.20 validates the accuracy of the instrument bridge, with deviations of less than 4 % for all cases except an outlier at the lowest speed of 0.1 m/s, where a relatively high error was recorded. This error is exaggerated due to the scaling effects of the velocity.

Table 5.20: Comparison of Instrument Bridge and Qualisys average surge velocities.

Desired (Bridge) (m/s)	Actual (Qualisys) (m/s)	Deviation %
0.1	0.085	15.0
0.18	0.175	2.8
0.22	0.213	3.2
0.26	0.251	3.5
0.3	0.289	3.7
0.5	0.496	0.8
0.54	0.535	0.9
0.58	0.578	0.3
0.62	0.615	0.8
0.66	0.662	0.3
0.7	0.7	0.0



(a) 0.1 m/s

(b) 0.3 m/s

(c) 0.5 m/s

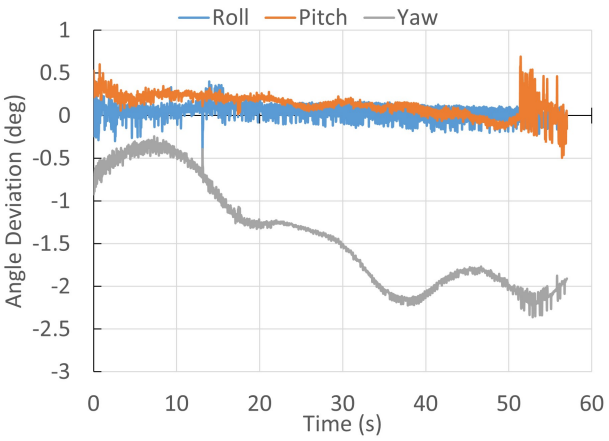
(d) 0.7 m/s

Figure 5.35: Comparison of Instrument Bridge and Qualisys surge velocities.

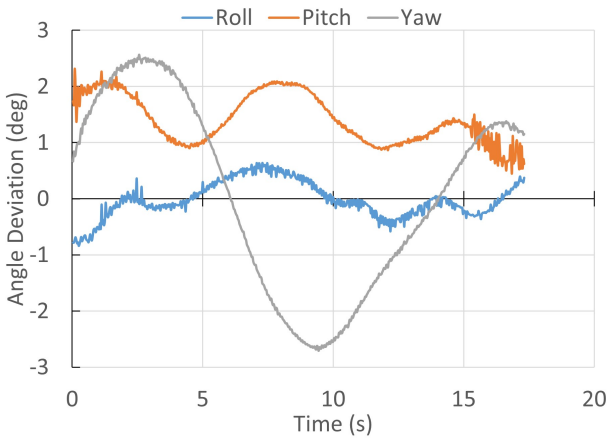
During testing of the OE Buoy, undesirable yaw and pitch motions were identified. From the assumptions outlined in section 4.3, the force exerted on the load cell was attributed to resistance from pure surge motion. To quantify the roll, pitch and yaw motions a Qualisys analysis was conducted, as displayed in Figure 5.36. At 0.11 m/s, the magnitude of the roll and pitch motions are insignificant. There is a correlation between towing speed and inclined towing, as evident from the larger pitch offset as towing speed increases. Roll offset is negligible as towing speed increases, however a correlation between towing speed and increased roll oscillations is shown. The starting position of the model before towing largely influenced the yaw response of the model. The equilibrium angle of the model in Figure 5.36 varies largely as a result of this. Similar to the roll response, a correlation between towing speed and increased yaw oscillations is evident, with oscillations of $\pm$ 1 $^\circ$ at 0.1 m/s to $\pm$ 3 $^\circ$ at 0.7 m/s. Table 5.21 displays the average model angles for a range of speeds, with a pronounced increase in inclined towing evident at higher towing speeds.

Table 5.21: Qualisys average roll, pitch and yaw results for the OE Buoy in the DOB.

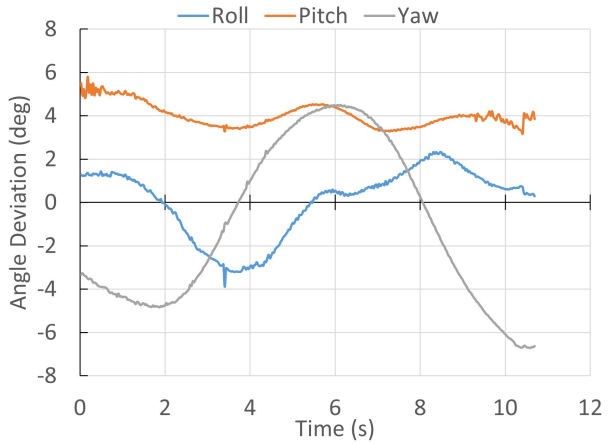
Body Velocity (m/s)	Roll (deg)	Pitch (deg)	Yaw (deg)
0.1	0.04	0.13	-1.40
0.18	0.03	0.56	0.20
0.22	0	0.84	-0.78
0.26	-0.02	1.23	-0.36
0.3	0.02	1.40	0.09
0.5	0.05	4.00	-1.09
0.54	0	4.30	-2.06
0.58	0.63	4.00	-1.15
0.62	-0.36	3.70	0.61
0.66	0.31	4.38	-1.51
0.7	-0.23	4.00	-0.69



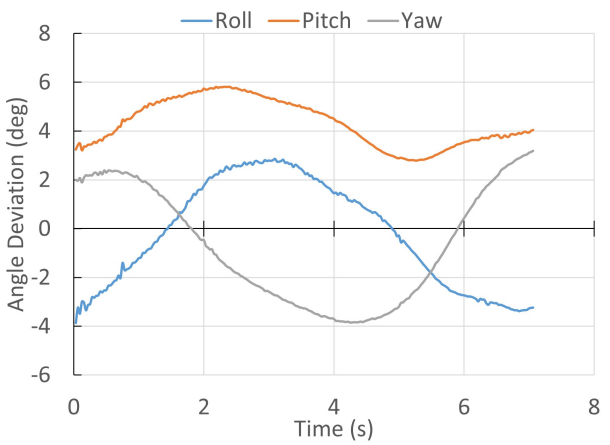
(a) 0.1 m/s



(b) 0.3 m/s



(c) 0.5 m/s



(d) 0.7 m/s

Figure 5.36: Qualisys roll, pitch and yaw results for the OE Buoy in the DOB.

5.2 Hydrodynamic Coefficient Testing - WCF

A comparison of the velocity measurement methods outlined in section 4.1 with results from Otter (2022) is shown in Figure 5.37. The velocity measurements from the manual method displayed a linear increase in current velocity as a function of thruster power. The Aquadopp device displayed inconsistent results, with current velocity unchanged between 30 - 40 % of thruster power and an increase from 20 to 25 % resulting in a lower velocity reading. Both methods were inferior to the Vectrino results from Otter (2022). Despite the improved velocity measurements using the manual method, C_d values for the WCF campaign were highly scattered, as seen in Figure 5.38. Aside from the different devices used to measure the current velocity, Otter (2022) used a deeper water depth of 1.2 m compared to 0.83 m in this testing, in addition to the use of a smoothing screen with a porosity of 44 %, to reduce turbulence in the flow.

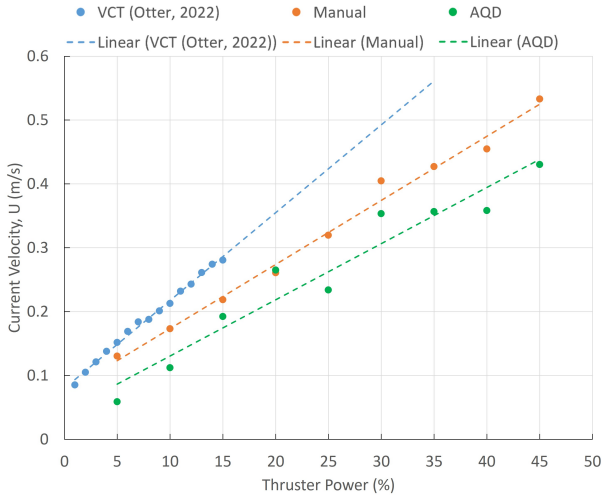
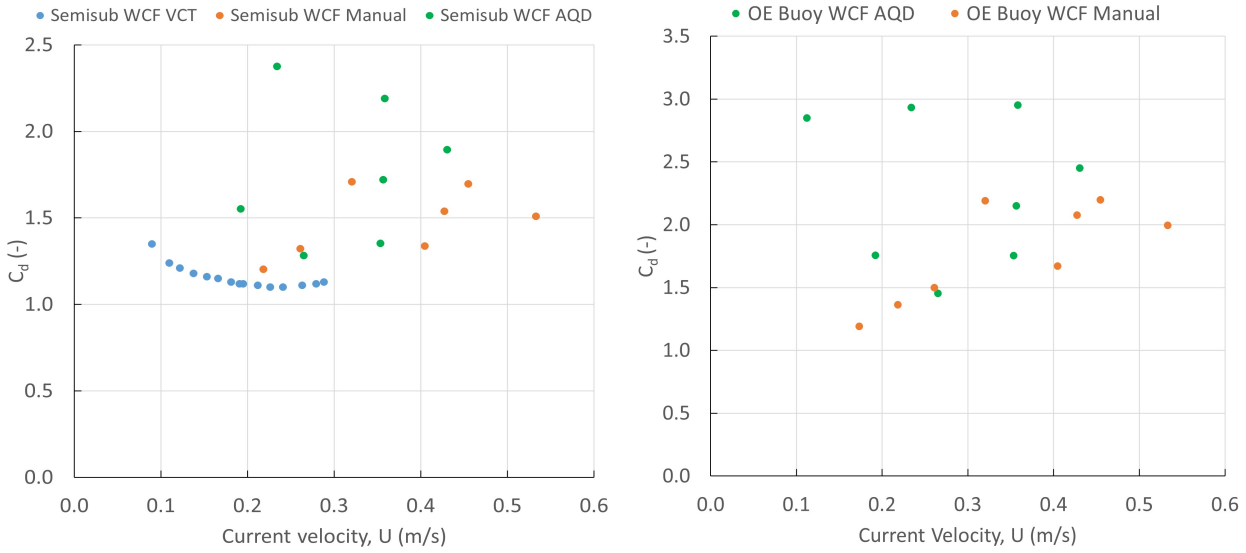


Figure 5.37: WCF current velocity method comparison.



(a) (b)

Figure 5.38: C_d from WCF resistance testing for (a) Semi-sub using Otter (2022) VCT results (b) OE Buoy.

Figure 5.39 compares the WCF and DOB tests for the INNWIND semi-sub. Due to the inconsistencies of the AquaDopp current profiler in measuring the WCF current velocity, it was assumed that the velocities obtained by Otter (2022) using the Nortek Vectrino were correct. Otter's velocities as a function of thruster power were used, with a linear fit applied and extended to higher velocities. These were coupled with the load cell values obtained during this campaign to derive a drag coefficient. Assuming the velocities of Otter (2022) are accurate and negating differences in current flows due to water depths and the use of porosity screens, the evaluated C_d of the semi-sub from the WCF and DOB is similar over the range of 0.3 - 0.7 m/s. Considering the turbulent flow and narrow channel of the WCF, compared with the controlled environment of the DOB, with accurate tow velocities, the difference between the basins is to be expected. The mechanism of testing also contributes to this difference in drag coefficient, with a larger drag experienced in the physical current of the WCF due to vortices in the flow, in comparison with the calm water of the DOB.

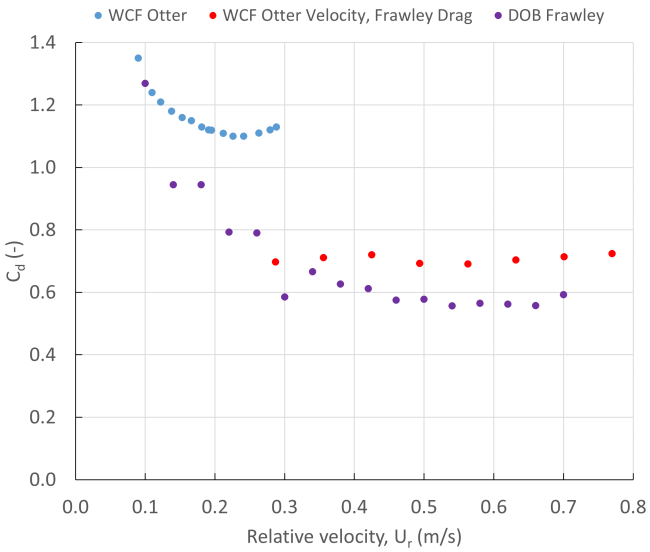


Figure 5.39: Comparison between the WCF and DOB for the INNWINDEU semi-sub.

5.3 Decay Test Response

The response of each DOF to an initial offset is presented in Figure 5.40. The influence of human error in the release of the platform in combination with the nature of the mooring setup has resulted in coupled motions, which are evaluated in Table 5.22. A strong coupling between sway and yaw is evident, resulting from the correcting force exerted by mooring line 2 (ML2) on column 2 (C2) for a given sway or yaw motion. This resulted in a yaw response of $\pm$ 7 °. Sway and surge motions are relatively constant across all tests. As the load cell was only attached to ML2 to set the pretension of all three lines, discrepancies between the tension of ML1 and ML3, which were set based on the spring displacement of ML2, could account for surge and sway disturbances.

A comparison of the natural periods derived from testing with that of Otter (2022) and the numerical model in AQWA is presented in Table 5.23. Interestingly, the largest discrepancies are seen for surge, sway and yaw when comparing the average experimental

results. An area of uncertainty between the results is the addition of the MPA to the tower. An equivalent weight was placed at the base of the tower on C2 to replicate the MPA. The addition of the MPA for the tests is not clarified in Otter (2022), therefore coupled pitch motions may be an influence attributing to the source of error between the results. The decay tests were conducted in AQWA, using the same initial offset per the experimental results (Table 5.22). A closer agreement between the experimental results and AQWA was seen compared with (Otter, 2022) further signifying potential setup differences. Confidence in the AQWA models' hydrodynamic setup is obtained as a result of the small margin of error between experiment and simulation.

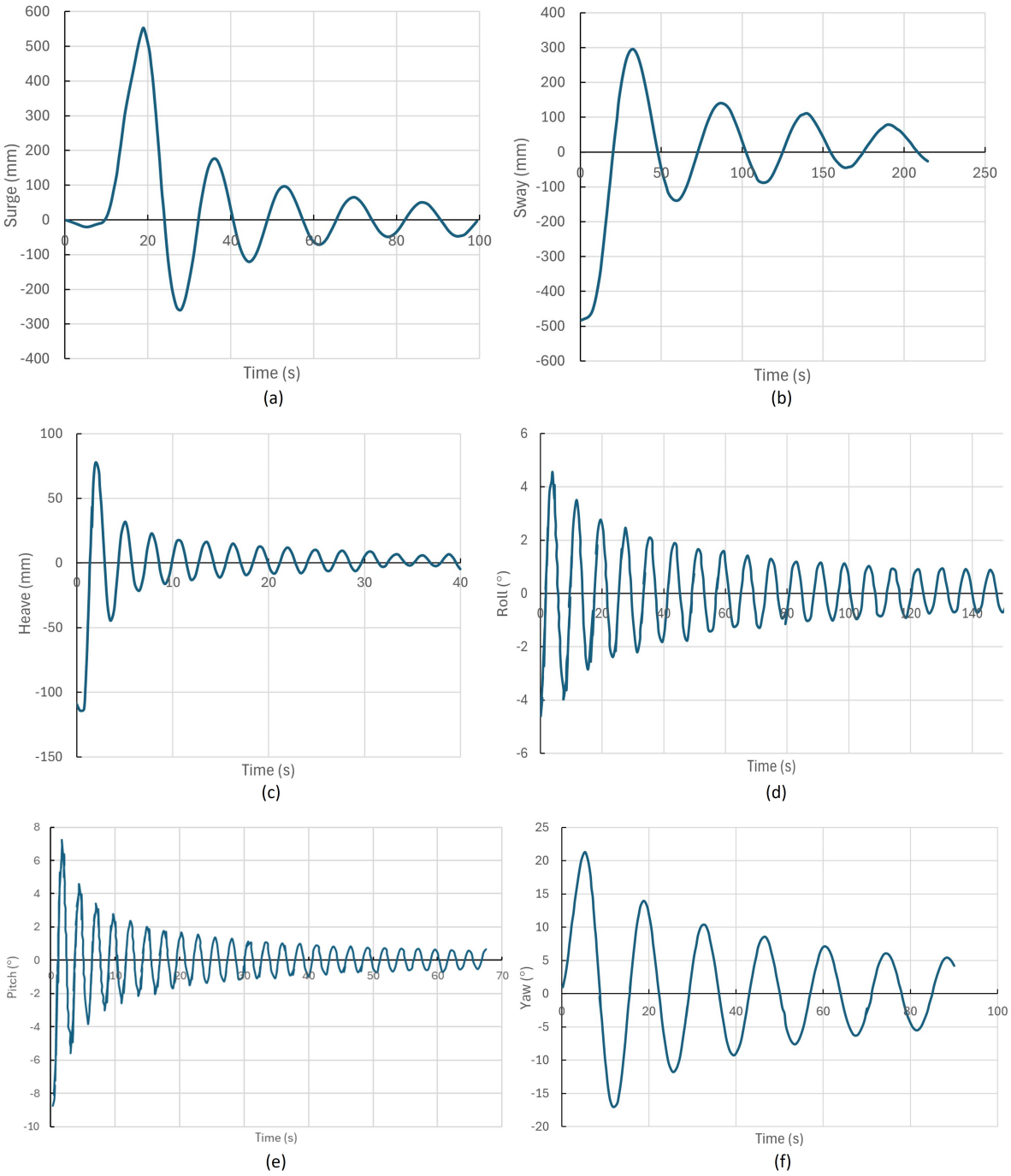


Figure 5.40: Experimental decay response using Qualisys (a) Surge (b) Sway (c) Heave (d) Roll (e) Pitch (f) Yaw.

Table 5.22: Maximum disturbances of coupled motions for each DOF test. Values in **bold** signify the initial disturbance for each test.

DOF	Surge (mm)	Sway (mm)	Heave (mm)	Roll (°)	Pitch (°)	Yaw (°)
Surge	**500**	± 80	± 5	± 0.5	± 1	± 6
Sway	± 40	**500**	± 8	± 0.5	± 0.4	± 7
Heave	± 40	± 50	**100**	± 0.75	± 0.5	± 2
Roll	± 40	± 40	± 10	**4.5**	± 1	± 1.5
Pitch	± 20	± 40	± 20	± 0.5	**8.5**	± 2
Yaw	± 40	± 50	± 7	± 0.5	± 1	**21**

Table 5.23: Natural period results compared with Otter (2022) and AQWA.

DOF	Test 1	Test 2	Average	Otter (2022)	AQWA	ΔOtter(%)	ΔAQWA(%)
T_n surge (s)	17.5	17.2	17.3	14.9	16.0	16.4	7.7
T_n sway (s)	19.2	19.2	19.2	16.1	20.3	19.4	5.6
T_n heave (s)	2.8	2.9	2.9	2.8	2.8	2.5	0.9
T_n roll (s)	2.7	2.8	2.7	2.9	2.9	5.9	6.5
T_n pitch (s)	2.6	2.7	2.6	2.9	2.9	9.1	10.3
T_n yaw (s)	13.5	14.2	13.9	10.8	14.2	28.2	2.7

5.4 RAO Results

A number of RAO tests were conducted in the DOB as per Table 3.14. The tests were chosen to evaluate the effect of the peak period, significant wave height and peak enhancement factor on the platform response. Figure 5.41 displays the results of Tests RAO1 - RAO7, which show the effect of changing the peak period for JONSWAP1. For each test, the peak response and correlating frequency were obtained using the MATLAB Signal Analyzer Toolbox, thus Figure 5.41 shows the combination of the peaks for each test. There is a good correlation between AQWA and experimental values for the Surge RAO spectrum. From the decay test results presented in Table 5.23, the RAO response of all motions spikes around their natural frequency. Heave, roll and pitch have natural periods of approximately 3 s, equivalent to 0.33 Hz. AQWA over-predicts the response at the natural frequency for both heave and pitch, while the experimental value surpasses the AQWA response for roll. While the tests don't cover the Surge natural frequency (0.057 Hz), the increase in response towards this value is evident.

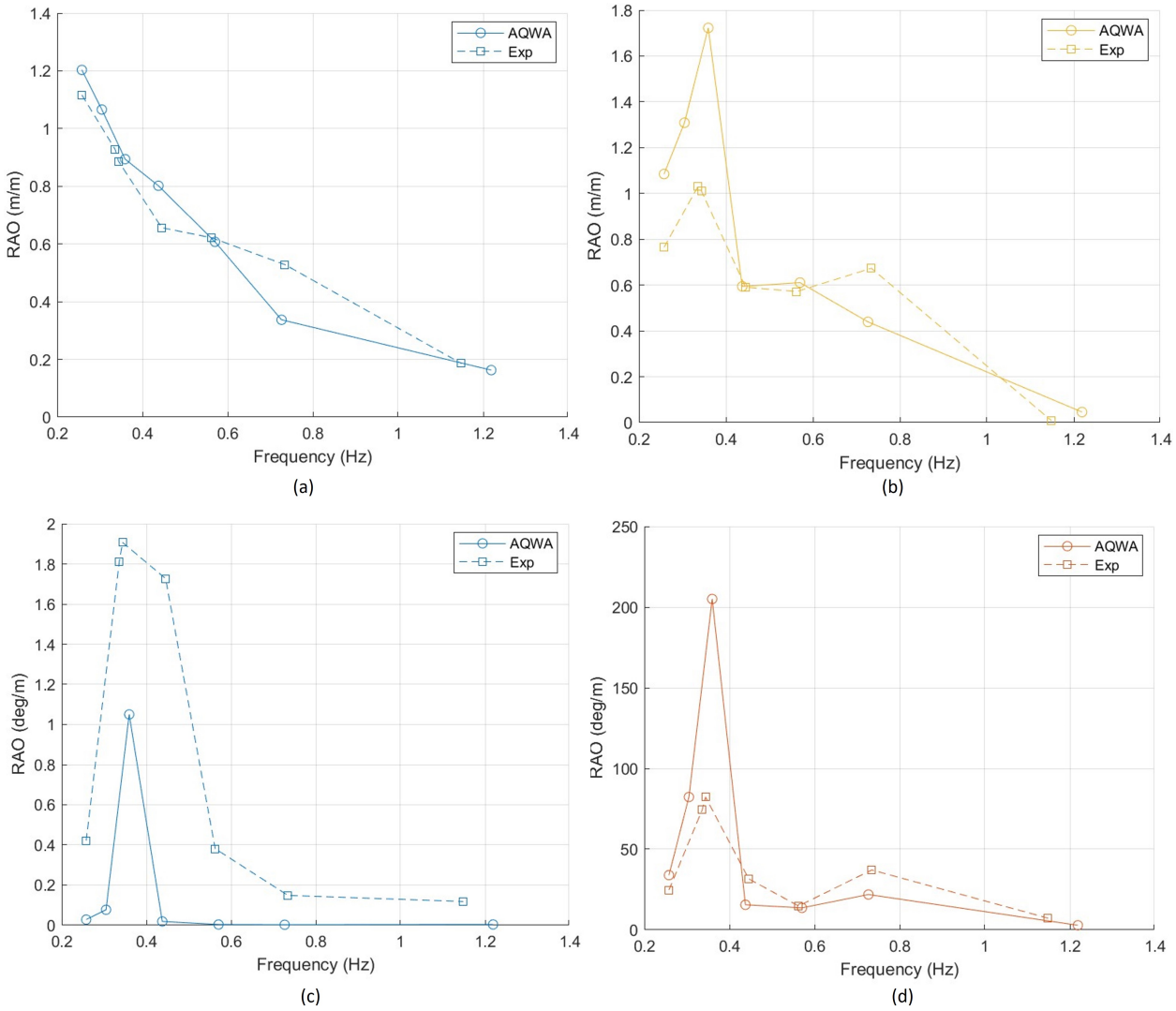
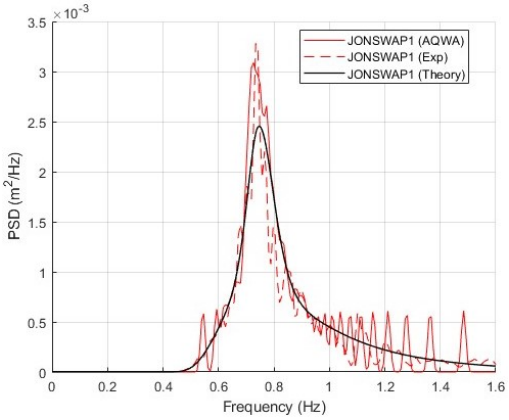


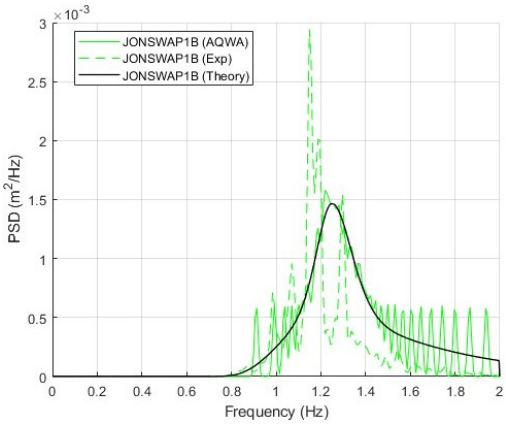
Figure 5.41: RAO1 - RAO7 response for (a) Surge (b) Heave (c) Roll and (d) Pitch .

A comparison of the wave elevation PSD between AQWA, experimental and theoretical values is presented in Figure 5.42. Both AQWA and experimental results are obtained through a wave probe time series of the wave elevation 2 m from the platform, while the theoretical spectra are obtained using the theory provided in equation 2.4. All methods correlate closely for the range of tests, however, AQWA displays a higher peak than the theory throughout. Figure 5.42 (h) has a significant wave height of 0.2 m compared to 0.1 m elsewhere. The error between the experimental and AQWA PSD values of JONSWAP1H is large and is likely due to an error in the wave elevation file obtained from the experiment.

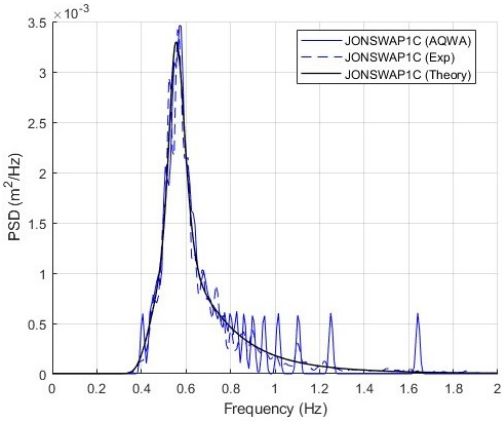
Figure 5.43 contains spectral energy plots for surge, heave, roll and pitch of Tests RAO9 - RAO11. For the surge and heave response, AQWA and experimental values align for JONSWAP2B and 2C, however, for JONSWAP2 the experimental values are approximately 70% lower than AQWA. AQWA generates a significantly reduced response in roll and is excited by a secondary frequency of approximately 0.4 Hz in pitch. This response is not matched by the experimental values. A significant discrepancy in the pitch response is evident from the JONSWAP2C test, conducted with the largest H_s. The experimental under-prediction of JONSWAP1H from Figure 5.42 (h) is not repeated in these tests, as clear increases in spectral energy occur for increasing H_s.



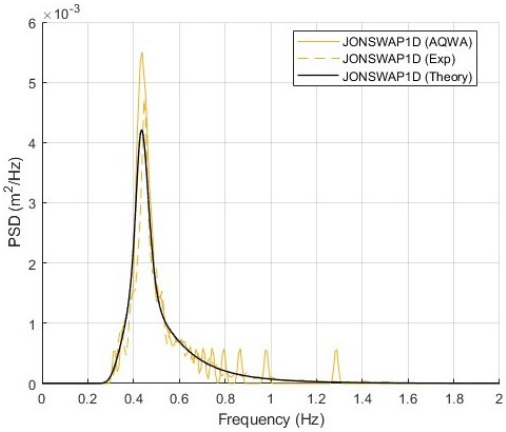
(a) JONSWAP1



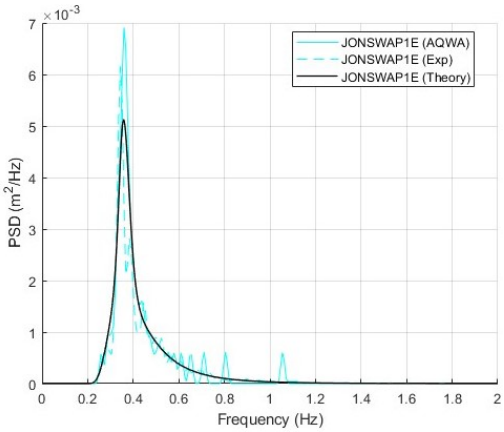
(b) JONSWAP1B



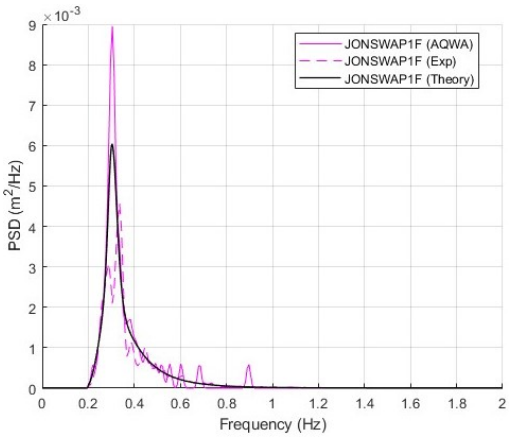
(c) JONSWAP1C



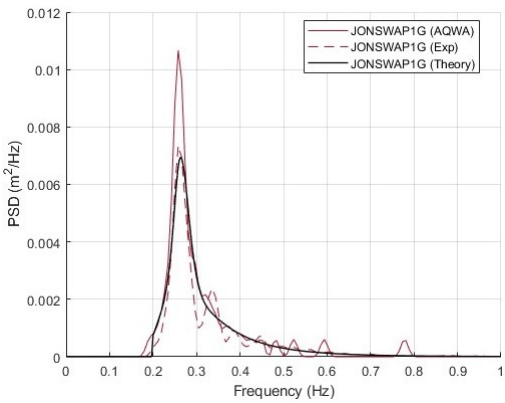
(d) JONSWAP1D



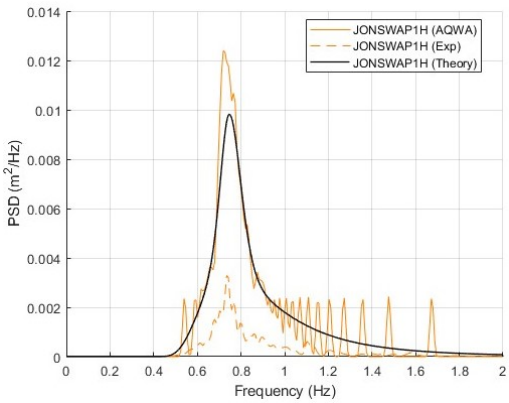
(e) JONSWAP1E



(f) JONSWAP1F

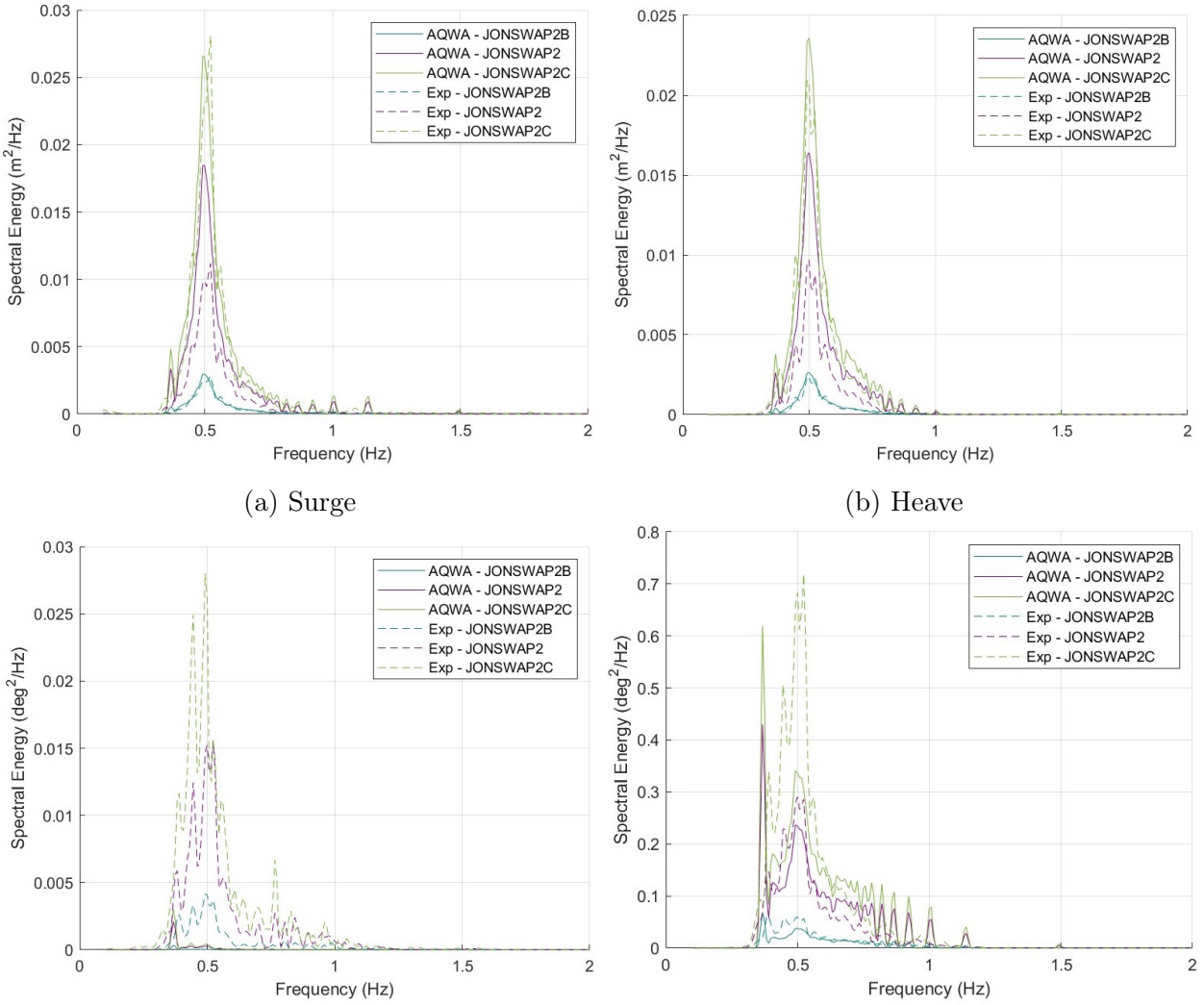


(g) JONSWAP1G



(h) JONSWAP1H

Figure 5.42: Wave Elevation PSD comparison between AQWA, Experimental and Theory for JONSWAP1.



(a) Surge

(b) Heave

(c) Roll

(d) Pitch

Figure 5.43: Spectral energy comparison between AQWA and Experimental JONSWAP2 for a range of H_s.

A final test to determine the influence of the peak enhancement factor on platform response was conducted as per Test RAO9 and RAO12. Figure 5.44 compares the theoretical and experimental effect changing γ has on the PSD of the waves. Theoretical and experimental values track closely and lowering of γ is seen to broaden the power distribution across a wider band of frequencies. Changing γ to 1 for the JONSWAP spectrum makes it similar to a Pierson-Moskowitz spectrum, by removing the peak enhancement which is a primary feature of the JONSWAP spectrum. The effect this has on the spectral energy is presented in Figure 5.45. Again the discrepancy between AQWA and experimental values is evident for JONSWAP2. Aside from this, the JONSWAP2D response shows a slightly reduced peak heave and surge response, with a wider range of energy density throughout. Interestingly, the response of the JONSWAP2D test shows higher peaks for both roll and pitch, despite the smaller peak enhancement factor.

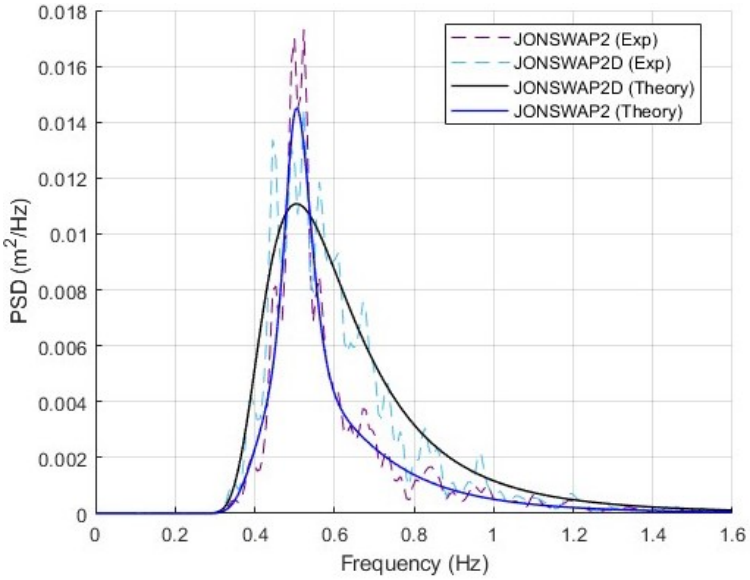
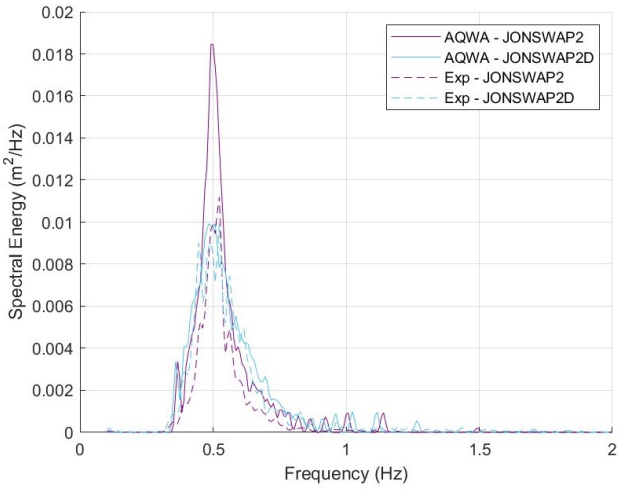
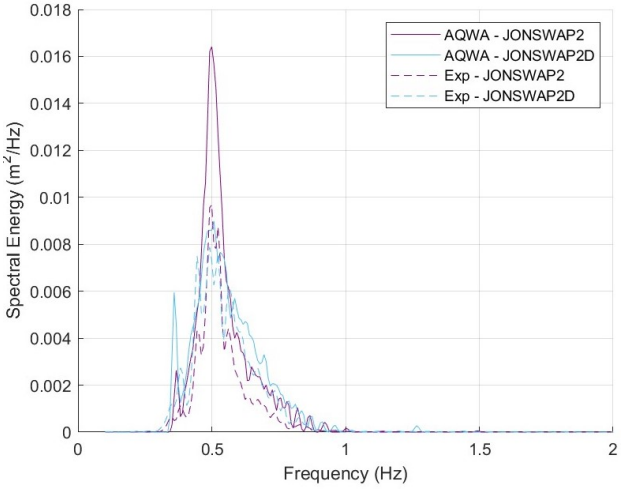


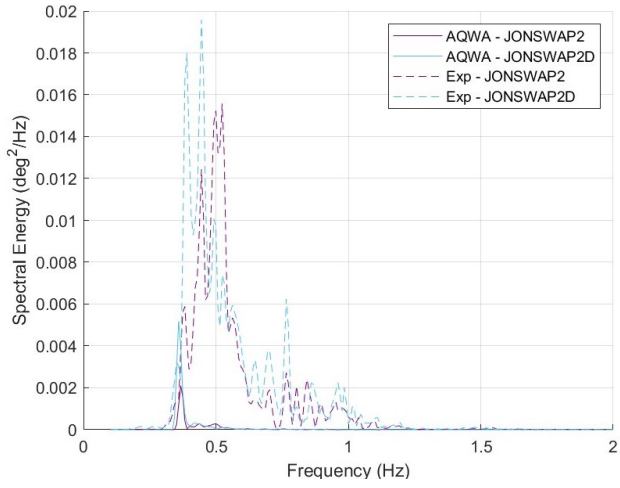
Figure 5.44: Wave PSD response to alteration of γ.



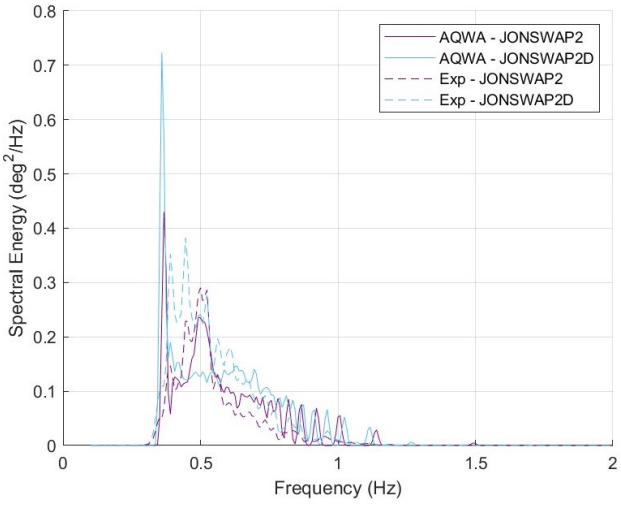
(a) Surge



(b) Heave



(c) Roll



(d) Pitch

Figure 5.45: Spectral energy comparison between AQWA and Experimental JONSWAP2 for a range of γ.

5.5 SIL - Current-Only Results

Initial tests were conducted with winch 1 (1.5 kW) by pulling the platform at a range of torque values and recording the winch line tension. Figure 5.46 highlights the shortcomings of the torque control system. The winch tension matches the desired tension closely in the initial phase, where the platform experiences surge motion, however, when the surge motion stops, the mooring restoring force causes the winch tension to increase and oscillate. Although the oscillation subsides, a steady state error in the tension exists as the torque isn't actively controlling the tension.

After adapting the system to read a force file instead of a torque file, the motor now reacts to the real-time tension in the winch and actively controls the torque to acquire the desired tension as specified by the force input file. The response of the system with the updated feedback loop is presented in Figure 5.47. This test used a proportional gain, K_p of 0.2 and an integral time, T_i of 0.01 s. The PI output was limited to between -0.3 V and 1 V for this test to protect the motor against excessive torque fluctuations. The average tension of the winch line for this test was 3.83 N, giving an error of 0.77 %. Further tuning of the PI controller was required as a time delay of approximately one second was observed between torque application and tension response as seen in Figure 5.48. At five seconds, the torque increases but at an inadequate rate, leading to the delay.

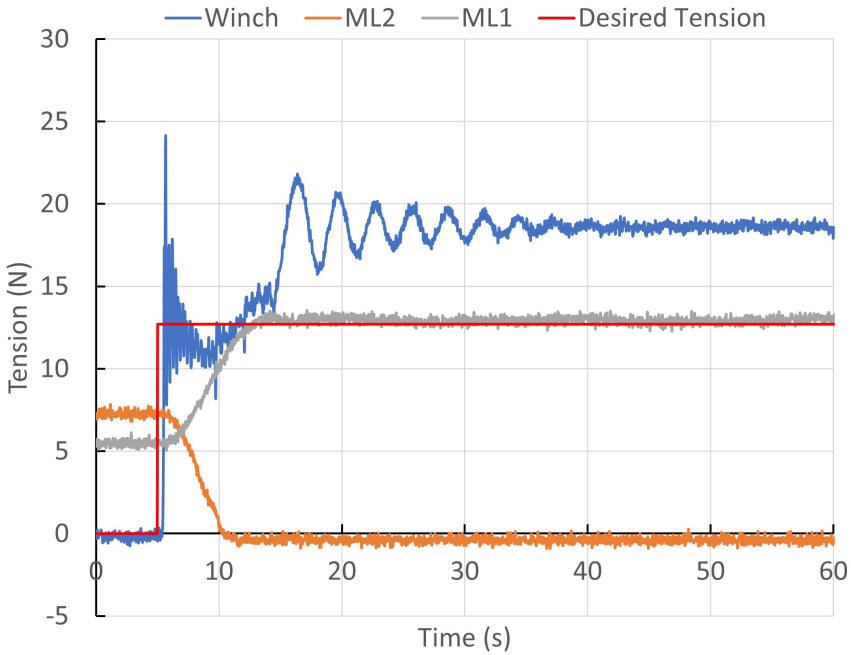


Figure 5.46: Tension response to current D, simulated with winch 1 using torque control mode.

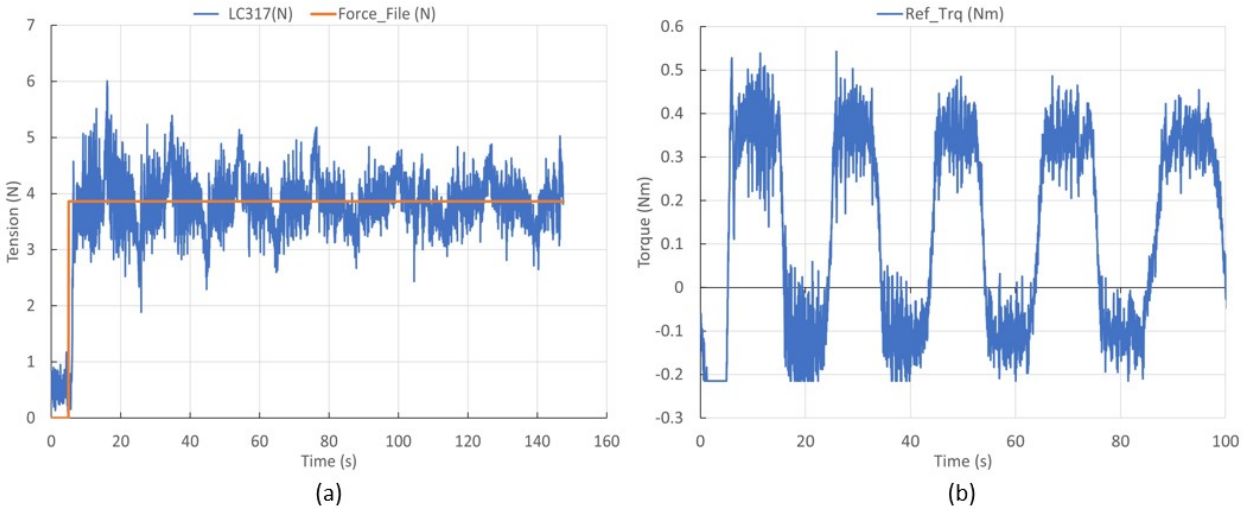


Figure 5.47: (a) Tension and (b) Torque response to current D, simulated with winch 1 using tension control mode.

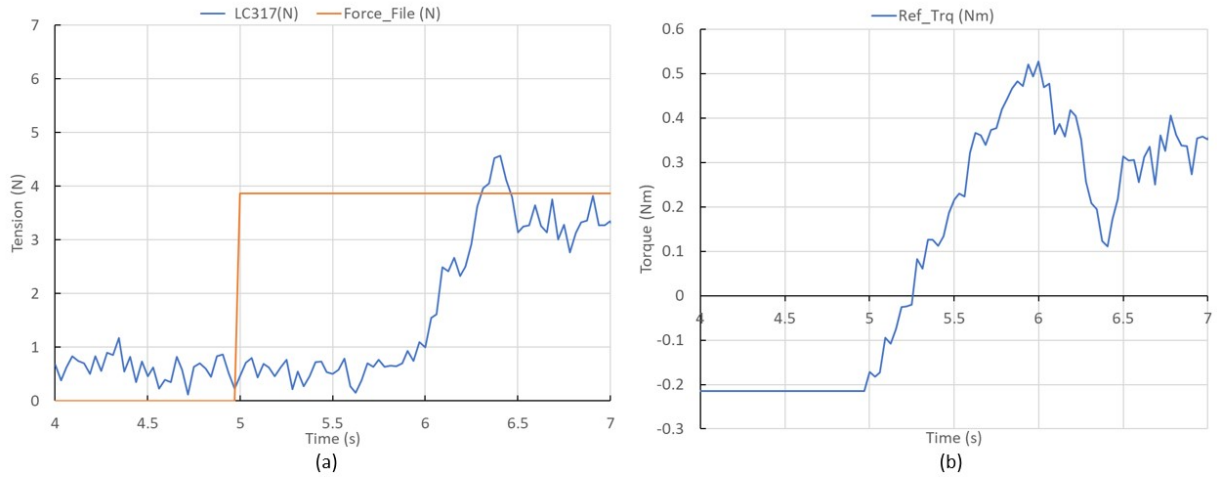


Figure 5.48: (a) Tension and (b) Torque response to current D, highlighting time delay in the system.

Mean tension and standard deviation were two metrics used to measure the accuracy of the current-only tests, C1 - C4. The Coefficient of Variation (CV) is the ratio of the standard deviation to the mean of the dataset. CV values > 1 are high-variance while CV values of < 1 are low-variance. The CV value helps determine the level of dispersion between the demanded and measured tensions. CV Demanded for TSIL is 0 as the demanded tension doesn't change. Current-only tests were conducted using the LabVIEW setup, with TSIL only. Table 5.24 displays the results of the tests, with a low CV for all velocities. CV is seen to decrease as current velocities increase, this is due to the sensitivity of CV for lower velocities due to the relatively small demanded tensions.

Table 5.24: Tests C1 - C4.

Current	Demanded Tension (N)	Measured Tension (N)	CV Measured (-)
A	2.95	2.945	0.121
B	3.86	3.844	0.119
C	7.59	7.589	0.085
D	12.71	12.684	0.056

Figures 5.49 and 5.50 display the dynamic response of the winch. While both results display minimal average errors, the control required for each speed is quite different. Figure 5.49 (a) displays the ML1 tension response to the current. The restoring force of the mooring system is approximately double the demanded tension and the influence it has on the torque control is high. As the platform oscillates in the surge DOF due to the mooring force, the winch control is more aggressive, with shorter periods for the torque control (b). Figure 5.50 (a) displays the results for Test C4, with the mooring line influence reduced compared to Test C1. Figure 5.50 (b) shows the period of torque control increasing as the mooring forces decay after 100 seconds, leading to a smoother and more accurate measured tension. This behaviour explains a higher error in standard deviation from Table 5.24 at lower speeds.

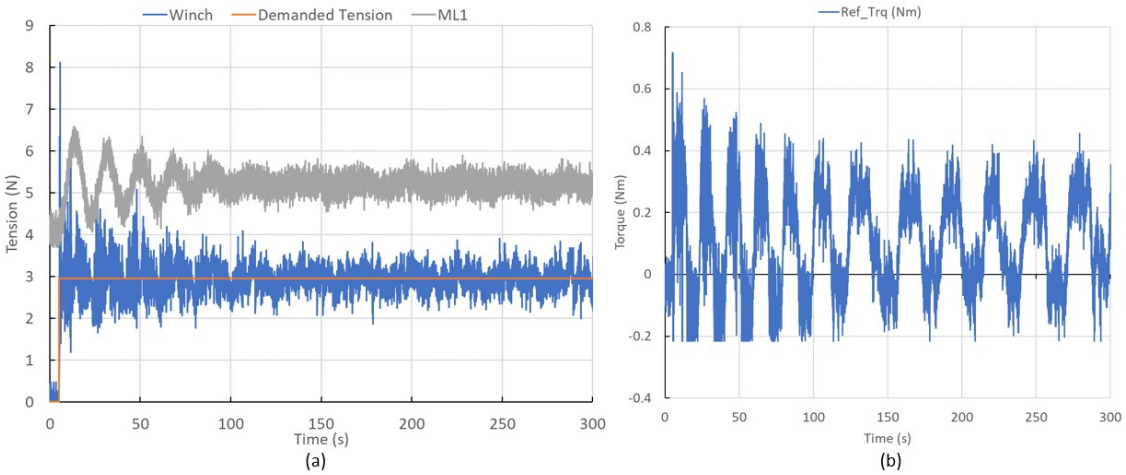


Figure 5.49: (a) Tension and (b) Torque response for Test C1.

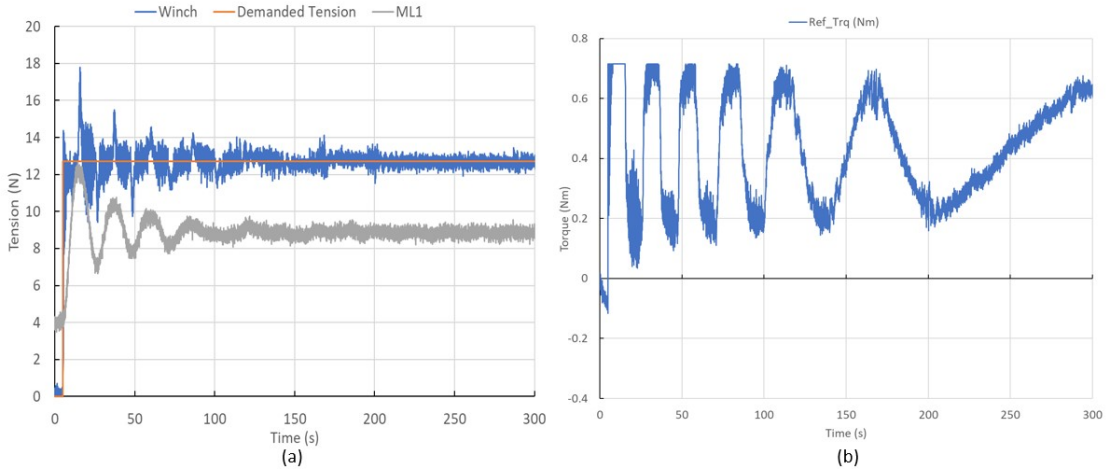


Figure 5.50: (a) Tension and (b) Torque response for Test C4.

For all current-only tests, the mooring system contributes to instability at the beginning of tests but decays after approximately 100 seconds. Due to the constant tension of the current drag, as opposed to wave-current conditions in later tests, the winch was tuned to minimise steady-state error once the mooring system has settled, rather than aggressively reacting to changes in the mooring forces. The proportional gain, K_p was set to 0.3 for C1 and C2, with the value reduced to 0.1 for C3 and C4. A larger gain was chosen for the slower speeds to minimise the influence of the mooring line oscillations on the system. This gain was subsequently reduced for the higher speeds where the influence of the mooring was not as influential. A disadvantage of increasing K_p for the lower speeds is the overshoot experienced. Figure 5.51 (a) highlights the resulting overshoot of the winch tension as a result of the higher K_p. This overshoot is minimised for test C4, however, this slows the winch response to mooring oscillations as highlighted in Figure 5.52 (b).

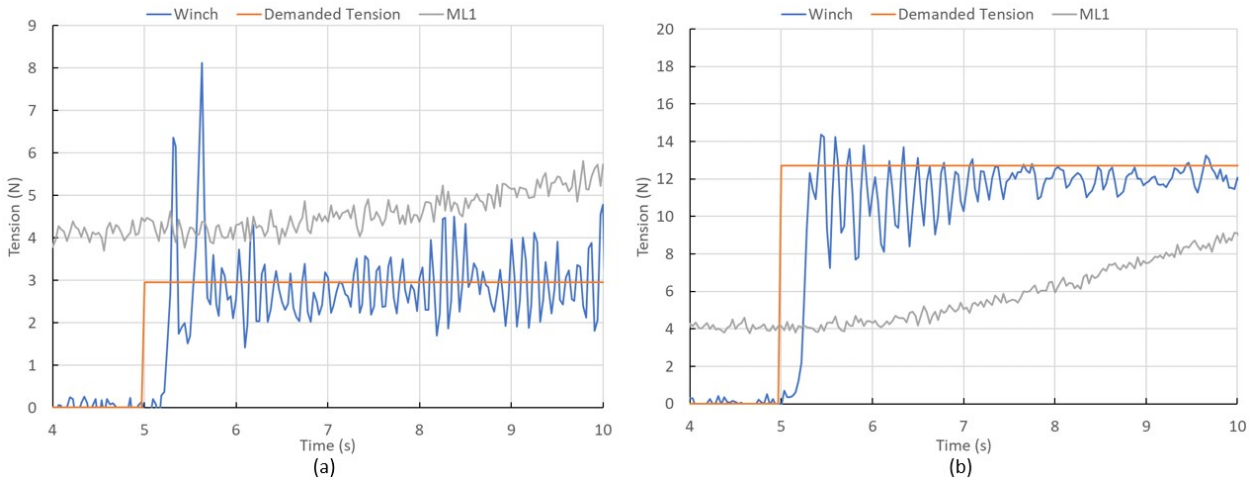


Figure 5.51: (a) Current A and (b) Current D PI reaction.

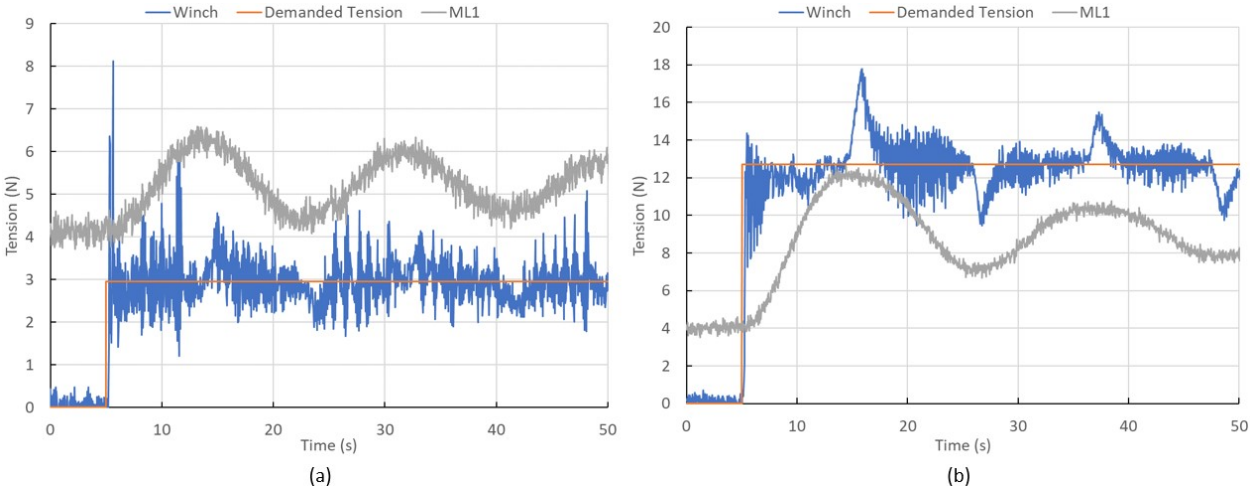


Figure 5.52: (a) Current A and (b) Current D winch response to the mooring.

A comparison of the surge response between experimental tests using the winch and Ansys AQWA are presented in Figure 5.53. Two simulations were conducted in AQWA, "AQWA Current" consisted of applying a physical current against the platform, while "AQWA Winch" used the cable winch feature that maintains constant tension in AQWA. For the cable winch,

a tension equivalent to the demanded tension from Table 5.24 was used for each test. The main comparisons between the results are:

- While AQWA Current over-predicts the damping of the system, AQWA Winch underpredicts it, with both displaying similar oscillations and longer settling times compared to the experimental results.
- Both AQWA simulations have the same settling surge displacement for all speeds except C4, where the Winch matches the experiment displacement well.
- For tests C1 - C3, AQWA underpredicts the surge displacement by between 15-30 %.
- Mooring line length discrepancies between the experiment and AQWA setup could explain the under-prediction of the surge in AQWA for most tests. AQWA was noted to be very sensitive to alterations of mooring line length.

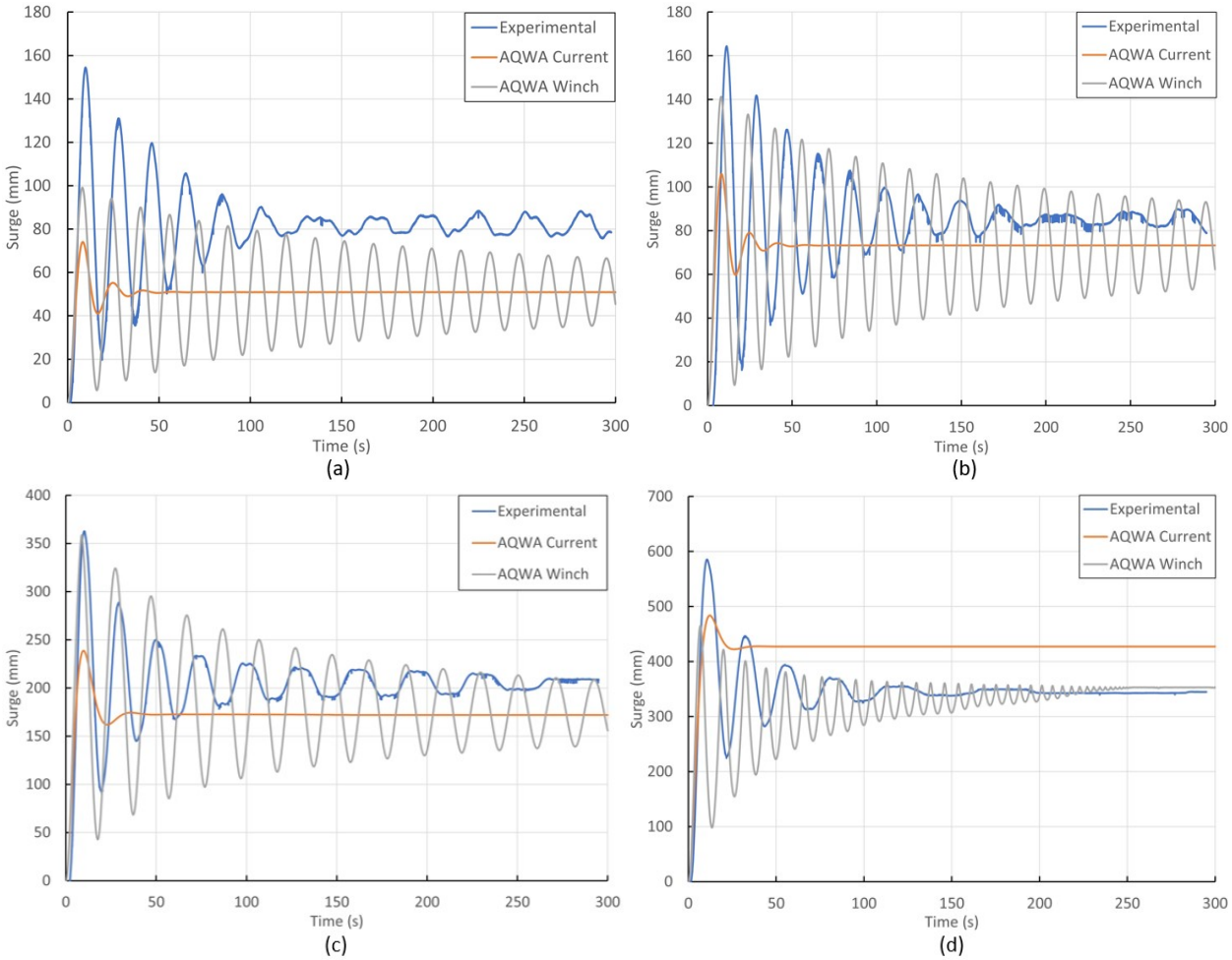


Figure 5.53: Comparison of Experimental and AQWA surge motion (a) C1 (b) C2 (c) C3 (d) C4.

5.6 SIL - Wave and Current Results

As described in section 4.2.4, the JONSWAP spectra have been altered in the experiments to account for the presence of current. The results of these adaptations are presented in

Table 5.25. For opposing waves and currents, higher current velocities lead to increased significant wave height and decreased peak period. Figure 5.54 displays the effect of these alterations on the PSD of the wave spectrum. The JONSWAP spectrum is not altered in AQWA as physical current is present. The amplitude of the peaks between AQWA and experiments agree for Current A but the experimental peak is double that of AQWA at Current C. Interestingly, the AQWA response with current displays a lower peak frequency than the original JONSWAP1 for waves only. For waves and currents directly opposing each other, peak frequency should be increased, as is displayed in the experimental results. Figure 5.55 presents a similar test with JONSWAP2. A closer agreement of the peak PSD between AQWA and experiments is evident for JONSWAP2, however, the AQWA peak frequency remains less than the original JONSWAP without current.

Table 5.25: Altered JONSWAP spectra for the presence of current, subscript I indicates the presence of current.

Wave	Current	H_s (m)	T_p (s)	H_{sI} (m)	T_{pI} (s)
JONSWAP1	A	0.1	1.34	0.116	1.265
JONSWAP1	B	0.1	1.34	0.121	1.243
JONSWAP1	C	0.1	1.34	0.137	1.188
JONSWAP1	D	0.1	1.34	0.160	1.127
JONSWAP2	A	0.25	1.98	0.276	1.907
JONSWAP2	B	0.25	1.98	0.284	1.886
JONSWAP2	C	0.25	1.98	0.306	1.835
JONSWAP2	D	0.25	1.98	0.332	1.780

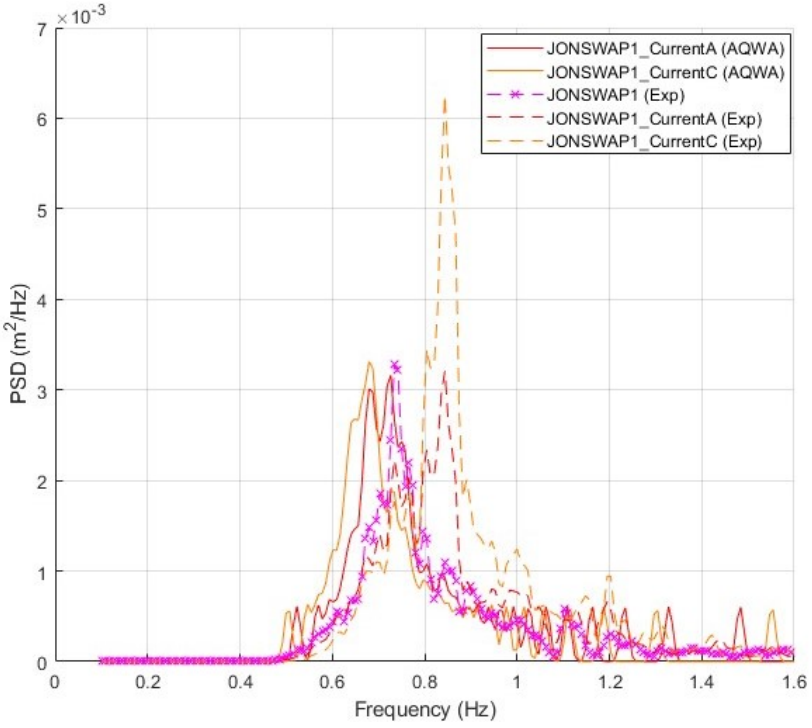


Figure 5.54: PSD of altered and original JONSWAP1 spectra.

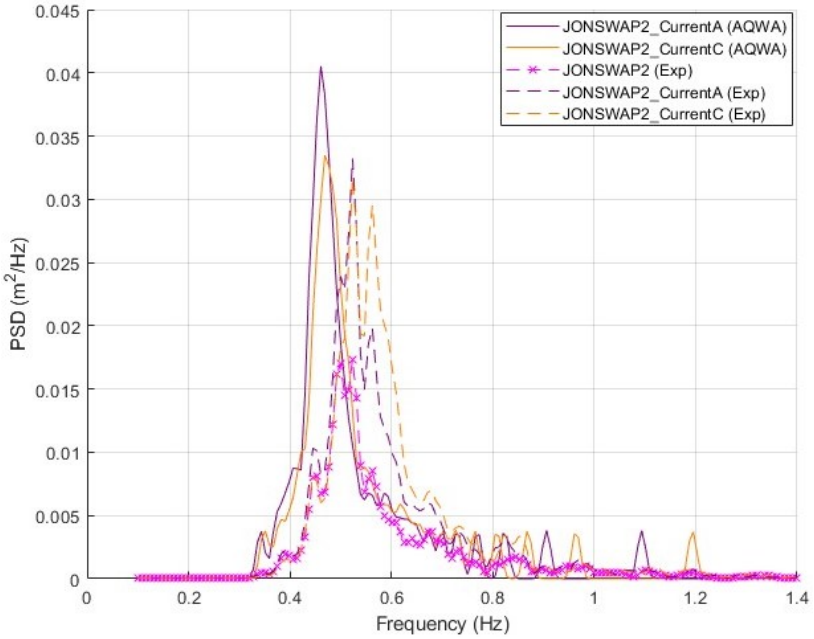
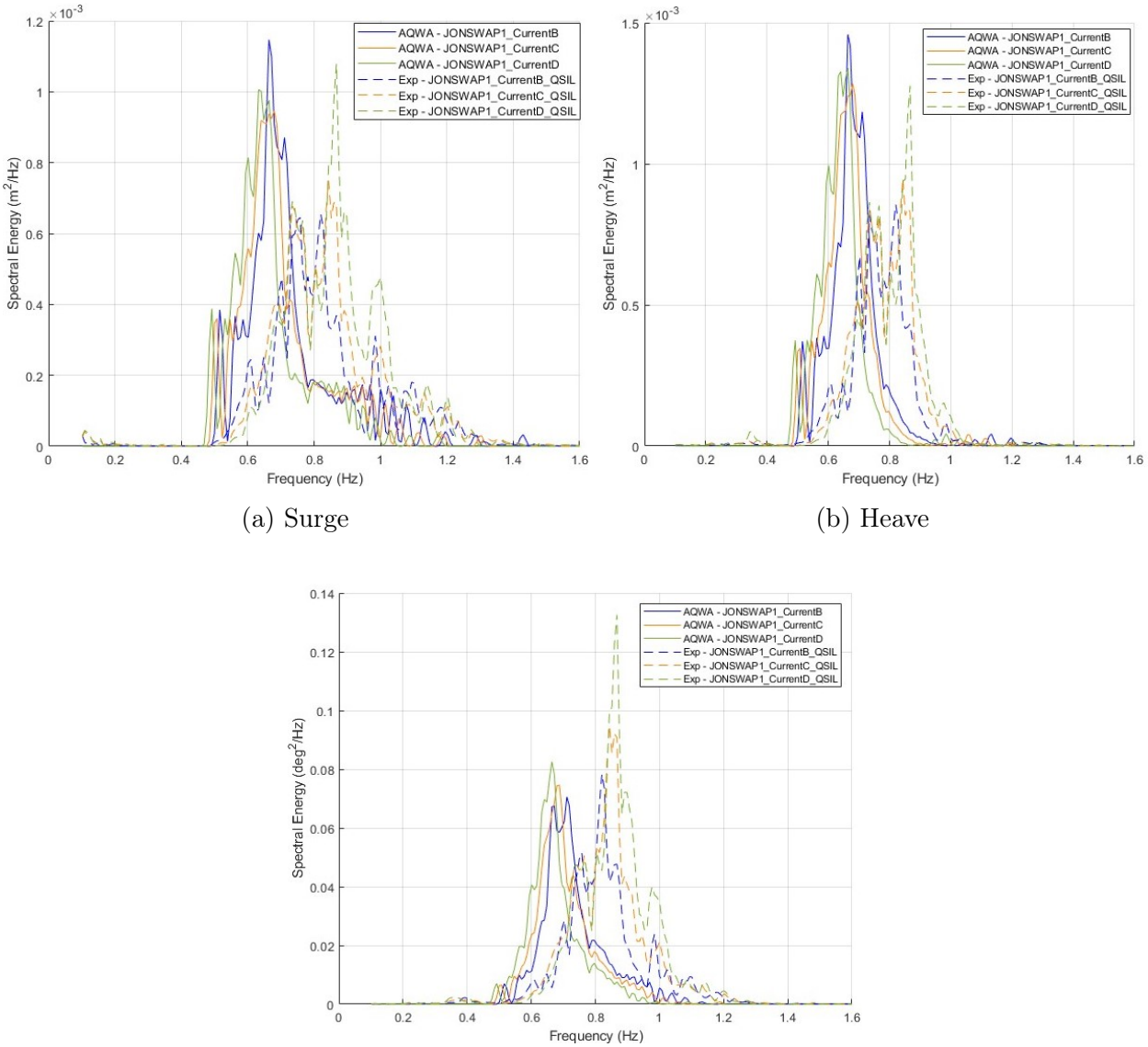


Figure 5.55: PSD of altered and original JONSWAP2 spectra.

Figure 5.56 presents the results from WC1, WC3 and WC4. A comparison between the surge, heave and pitch spectral energy between the AQWA simulations and experimental simulations with QSIL provides the following observations:

- AQWA over-predicts the surge and heave response for current B, while the response for current D agrees with experimental values.
- The pitch response peak energy is accurate for lower velocities, with this accuracy reducing for higher velocities
- Experimental values show a clear increase in peak frequency for an increase in current velocity, as expected from theory. AQWA however, shows the opposite trend, with an increasing current velocity leading to a decreasing peak frequency.
- The discrepancies between the numerical model in AQWA and experimental testing are likely attributed to the numerical model used. As mentioned in Section 3.4, inclusion of wave absorption techniques and a more extensive mesh sensitivity study could address the phase shift and magnitude differences presented in Figure 5.56. It may also improve the wave-current interactions in AQWA, by increasing the natural frequency response as current velocity increases, as expected by theory (Section 2.2.4), thus narrowing the gap between numerical and experimental results.



(a) Surge

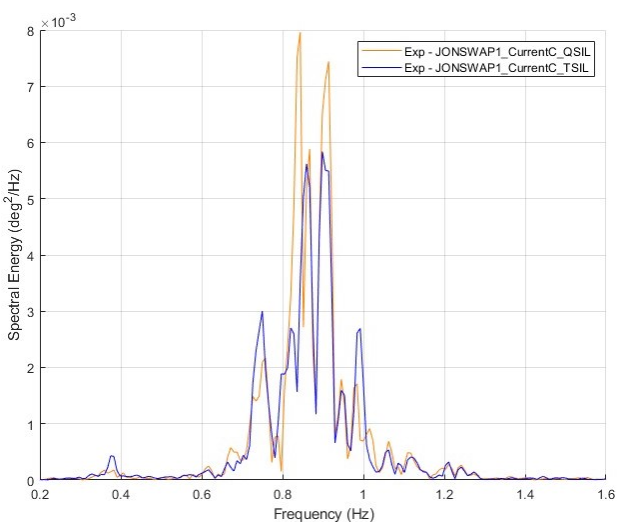
(b) Heave

(c) Pitch

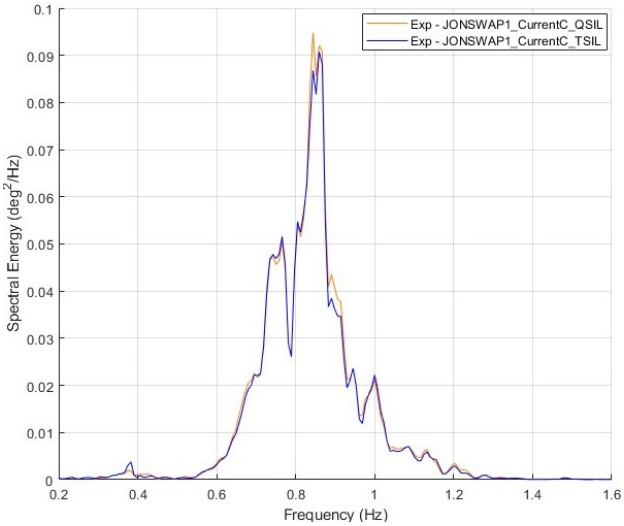
Figure 5.56: Spectral energy comparison between AQWA and Experimental JONSWAP1 with QSIL.

Figures 5.57 and 5.58 compare the TSIL and QSIL methods on platform response for a range of currents and JONSWAP. Tests WC2, WC3, WC5, WC6, WC8, WC9 and WC10 are presented. No TSIL test was conducted for JONSWAP2_CurrentD however the QSIL results are included here for comparison. The differences between TSIL and QSIL are:

- The peak energy of all results is marginally greater with QSIL than TSIL, except JONSWAP2 roll. This demonstrates that control with QSIL results in greater platform dynamics than TSIL. This is likely due to the real-time update of the surge velocity to update the relative velocity between the platform and current flow.
- JONSWAP2 Current A has a lower peak frequency compared to Current C as expected, however unexpectedly, the peak energy is larger for Current A for all DOFs presented. As anticipated Current D has a larger peak energy and frequency than both Current A and C, leading me to believe there is an error in the Current C result.

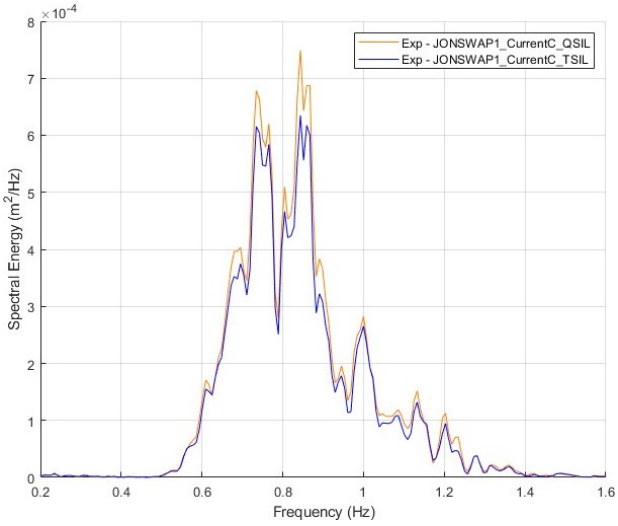


(c) Roll

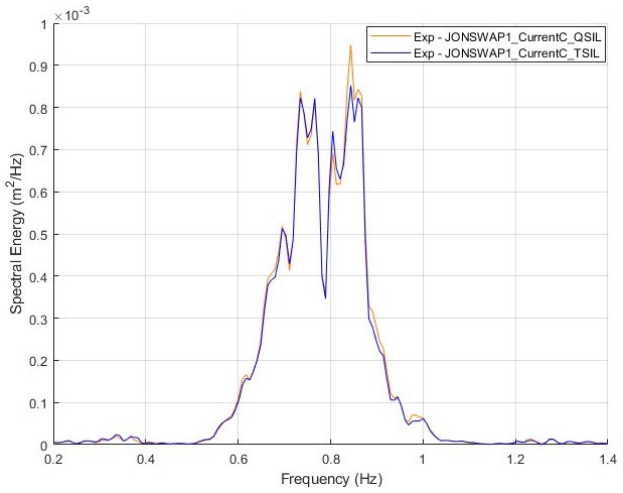


(d) Pitch

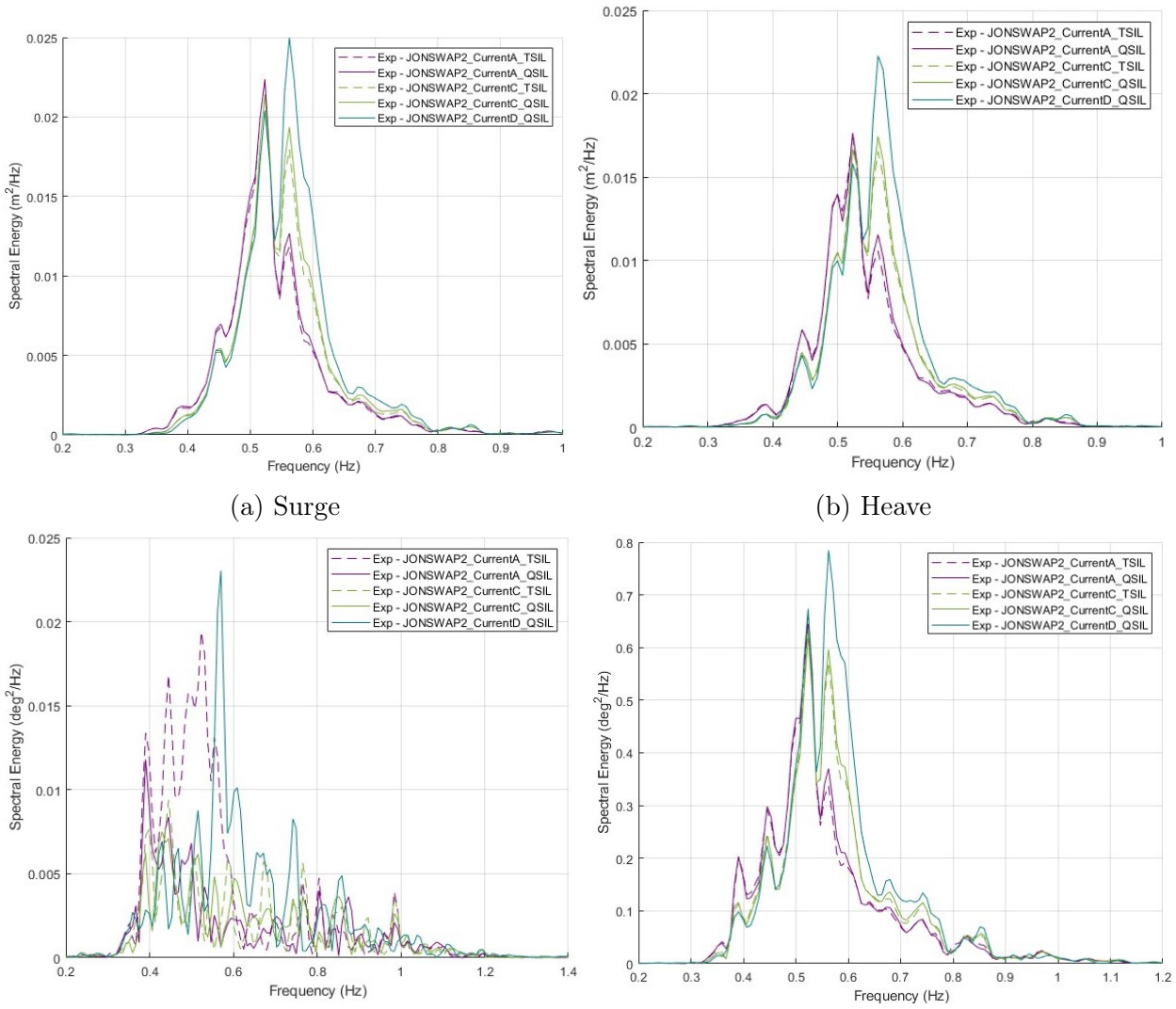
Figure 5.57: Comparison between TSIL and QSIL for JONSWAP1 and Current C.



(a) Surge



(b) Heave



(a) Surge

(b) Heave

(c) Roll

(d) Pitch

Figure 5.58: Comparison between TSIL and QSIL for JONSWAP2 and Currents A and C.

Table 5.26 compares the Coefficient of Variation (CV) of the demanded and measured tension of the winch actuator for both TSIL and QSIL tests. The following observations are made:

- WC2 and WC3 compare JONSWAP1 with Current C. Both CV Demanded and CV Measured increase when QSIL is used.
- WC5 and WC6 compare JONSWAP2 with Current A. The CV Measured for TSIL is seen to increase compared with WC2. The lower demanded tension required for Current A makes the CV more sensitive to fluctuations, likely leading to a higher CV. A large increase in CV for the QSIL test is observed, making the dataset high-variance. The CV Demanded is highly variable due to the nature of the irregular JONSWAP spectrum applied.
- WC8 and WC9 compare JONSWAP2 with Current C. A similar CV Measured is obtained as seen with JONSWAP1 Current C, indicating the lower current velocity is the reason for the high CV Measured for WC5. While the dataset is still high-variance,

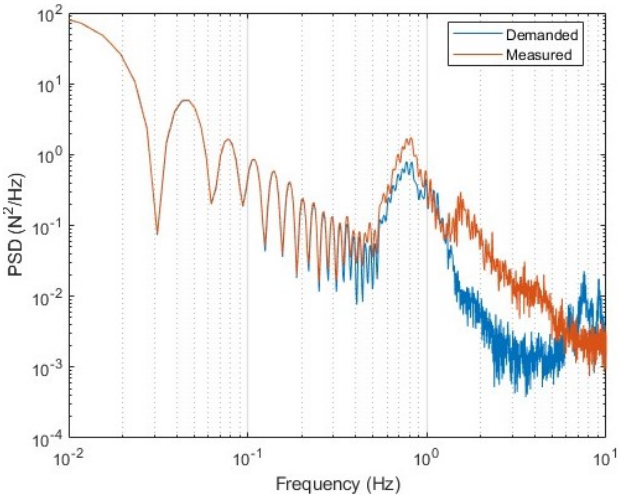
a reduction between WC6 and WC9 indicates the higher current velocities perform better.

- The increase in CV between JONSWAP1 and JONSWAP2 indicates the QSIL system performs better at lower wave heights with shorter periods.
- Δ CV for QSIL is relatively low throughout, indicating the winch system accurately tracks the variability of the demanded tension. A consistent relationship between the demanded and measured tensions is maintained for a range of environmental loads.
- Comparing the TSIL results with current-only tests from Table 5.24, wave loads increase the variability in the system, with the effect reduced for higher current velocities.

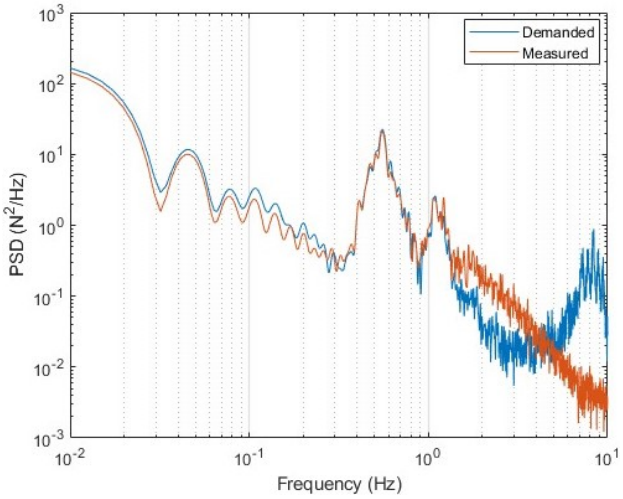
Table 5.26: Coefficient of Variation (CV) of demanded and measured tension for TSIL v QSIL.

Test	Method	CV Demanded (-)	CV Measured (-)	$\Delta CV(-)$
WC2	TSIL	0	0.366	0.366
WC3	QSIL	0.4	0.567	0.147
WC5	TSIL	0	0.809	0.809
WC6	QSIL	1.309	1.336	0.027
WC8	TSIL	0	0.46	0.46
WC9	QSIL	1.051	1.144	0.093

Figure 5.59 displays the power spectral density of the demanded and measured winch tension. Both plots display the winch's ability to capture low-frequency fluctuations accurately while a poor correlation between the demanded and measured tensions above 1 Hz is evident. A closer correlation between the demanded and measured tension is exhibited in (a) for lower frequencies than in (b), this contributes to the higher errors discussed for JONSWAP2 in Table 5.26. Despite the better results for JONSWAP1 in Table 5.26, an over-prediction of the measured tension at the peak period is present. JONSWAP2 does not over-predict at its peak period and underpredicts for lower frequencies. Figure 5.60 compares ML1 tension for QSIL v TSIL and for a range of current velocities. The tension in ML1 is equivalent for QSIL and TSIL methods across all frequencies. As expected, the higher current velocity produces a greater response.

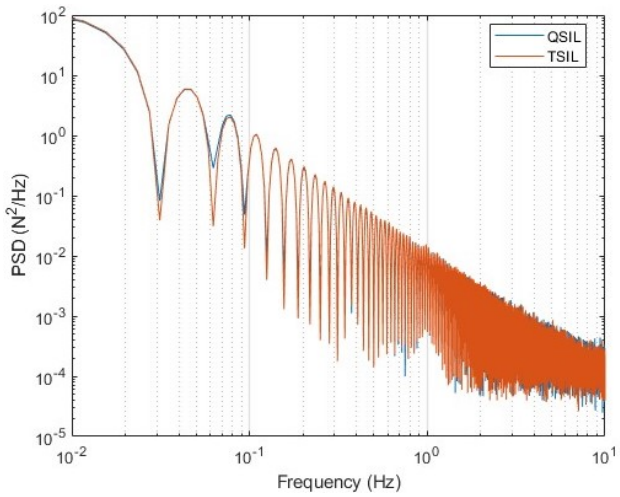


(a) JONSWAP1 Current C

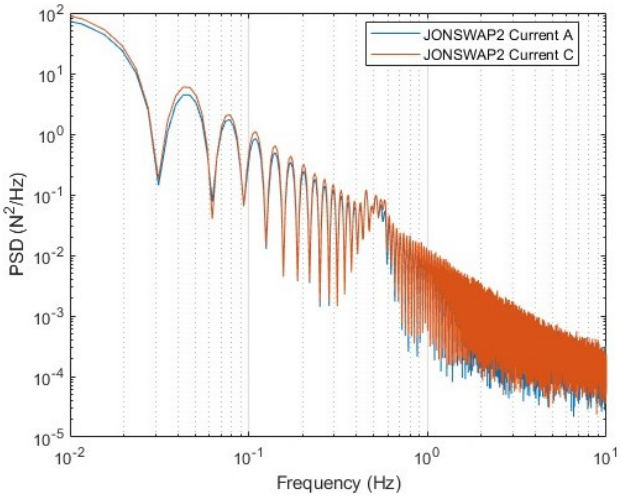


(b) JONSWAP2 Current C

Figure 5.59: Winch tension comparison for QSIL.



(a) JONSWAP1 Current C QSIL v TSIL



(b) JONSWAP2 QSIL Current A v C.

Figure 5.60: Mooring Line 1 tension comparison.

Chapter 6 - Conclusions & Recommendations

6.1 Conclusions

The purpose of this study was to advance the software in the loop system for current simulation in wave tanks initially developed by Otter (2022). Three objectives were outlined to advance the system: Expansion of the hydrodynamic drag coefficient testing to compare multiple platforms and test configurations. The addition of a second winch to enable a range of current incidence angles to be tested. To determine the performance of the system for a wider range of current and wave conditions.

The main findings of the study are as follows:

- Tow testing in the DOB resulted in consistent results for both the semi-sub and OE Buoy. Large uncertainty surrounded the WCF current velocities due to the AquaDopp results. Implementing the velocities of Otter (2022) with the drag forces from the WCF campaign, resulted in a moderate agreement between the C_d obtained in the WCF and DOB. The WCF C_d was higher than that obtained in the DOB for the semi-sub, this is likely attributed to the turbulent flow of the physical current.
- The natural periods from the decay tests in the DOB and AQWA showed a high level of agreement with differences of less than 10.3 % for all degrees of freedom. The repeatability between tests conducted in the DOB was good.
- The RAO results between AQWA and experiments correlated well in the surge axis. For heave, roll and pitch the excitation frequencies correlated, however, discrepancies in the amplitude of excitation were present.
- The wave PSD comparison between theory, AQWA and experiments showed there was no phase shift between the methods, however, AQWA frequently over-predicted the peak power by between 20-55 %. This resulted in a likely source of error for the peak RAO discrepancy.
- Current-only tests of the TSIL system demonstrated a CV of less than 0.13 throughout, with this reducing to 0.06 for the highest current velocity.
- Discrepancies in the current-only surge results between AQWA and experiments are believed to be due to inaccuracies in the simulation mooring line setup, with extreme sensitivity experienced in AQWA to mooring line length.
- The correlation between the spectral energy of TSIL and QSIL was strong, with QSIL resulting in marginally higher peaks.
- Variation in the tension response of the winch increased with the presence of waves. For Current C, *CV Measured* increased by 0.281 with the addition of JONSWAP1.
- Higher current velocities reduced the variation of the winch response. For JONSWAP2, CV was 1.336 with Current A while CV = 1.144 with Current C.

- Winch tension variation is high for QSIL tests due to the irregular JONSWAP spectra, however, the measured tension matched the variation in the demanded tension, signifying the winch accurately adapted to changes in demanded tension for a range of conditions. Although the absolute values of the current drag force obtained may be uncertain due to poor C_d results, the system's ability to dynamically adapt to a demanded tension provides confidence that the system can accurately replicate physical current forces.

- The proposal of a hardware layout and Simulink code for a dual-winch system was achieved during this study. This should aid the implementation and troubleshooting of the second winch.

Overall, the advancement of the software in the loop system has been achieved through the completion of a wider range of wave and current loads. The winch actuator has proved to be a viable alternative method of simulating current loading on platforms in wave tanks in the absence of physical current.

6.2 Recommendations For Future Work

- Physical current loading of the platform to validate the winch actuator with current and wave conditions present. This will validate the winch control and aid in tuning the AQWA model further. A comparison of the wave-current interaction method used in this study with physical wave-current conditions would be beneficial in narrowing the sources of error from this study.

- Implementation of the second winch as per the control system and physical layout as described within, to enable a wider range of current incidence angles.

- Repeated C_d testing of the INNWIND model in the WCF with an improved current velocity measurement device. The effect of porosity screens on the results should also be quantified.

- Further testing of the QSIL system with the inclusion of wind loading using the MPA device developed by Otter et al. (2020). Similar to surge feedback, pitch feedback should be implemented in the Simulink code.

References

Ahmed, I., Rostom, S., and Choudhury, M. S. (2011). Interfacing an interactive mimo process and implementing decoupler to compensate loop interactions.

Ansys, A. (2016). Aqwa user's manual release 17.0. *ANSYS Inc.: Canonsburg, PA, USA*.

Atcheson, M., Garrad, A., Cradden, L., Henderson, A., Matha, D., Nichols, J., Roddier, D., and Sandberg, J. (2016). *Floating offshore wind energy*, volume 10. Springer.

Atlar, M. (2011). Recent upgrading of marine testing facilities at newcastle university. In *AMT'11, the second international conference on advanced model measurement technology for the EU maritime industry*, pages 4–6.

Azcona, J., Bouchotrouch, F., González, M., Garciandía, J., Munduate, X., Kelberlau, F., and Nygaard, T. A. (2014). Aerodynamic thrust modelling in wave tank tests of offshore floating wind turbines using a ducted fan. In *Journal of Physics: Conference Series*, volume 524, page 012089. IOP Publishing.

Azcona, J., Palacio, D., Munduate, X., Gonzalez, L., and Nygaard, T. A. (2017). Impact of mooring lines dynamics on the fatigue and ultimate loads of three offshore floating wind turbines computed with iec 61400-3 guideline. *Wind Energy*, 20(5):797–813.

Bachynski, E. E., Chabaud, V., and Sauder, T. (2015). Real-time hybrid model testing of floating wind turbines: sensitivity to limited actuation. *Energy Procedia*, 80:2–12.

Bachynski, E. E., Thys, M., Sauder, T., Chabaud, V., and Sæther, L. O. (2016). Real-time hybrid model testing of a braceless semi-submersible wind turbine: Part ii—experimental results. In *International Conference on Offshore Mechanics and Arctic Engineering*, volume 49972, page V006T09A040. American Society of Mechanical Engineers.

Barrera, C., Guanche, R., and Losada, I. J. (2019). Experimental modelling of mooring systems for floating marine energy concepts. *Marine Structures*, 63:153–180.

Barrera, C., Guanche, R., Rodríguez, Á., Armesto, J. A., and Losada, I. J. (2020). On the importance of mooring system parametrisation for accurate floating structure designs. *Marine Structures*, 72:102765.

Bayati, I., Belloli, M., and Facchinetti, A. (2017). Wind tunnel 2-dof hybrid/hil tests on the oc5 floating offshore wind turbine. In *International Conference on Offshore Mechanics and Arctic Engineering*, volume 57786, page V010T09A076. American Society of Mechanical Engineers.

Bayati, I., Facchinetti, A., Fontanella, A., Giberti, H., and Belloli, M. (2018). A wind tunnel/hil setup for integrated tests of floating offshore wind turbines. In *Journal of Physics: Conference Series*, volume 1037, page 052025. IOP Publishing.

Belloli, M., Bayati, I., Facchinetti, A., Fontanella, A., Giberti, H., La Mura, F., Taruffi, F., and Zasso, A. (2020). A hybrid methodology for wind tunnel testing of floating offshore wind turbines. *Ocean Engineering*, 210:107592.

Benitz, M. A., Schmidt, D. P., Lackner, M. A., Stewart, G. M., Jonkman, J., and Robertson, A. (2015). Validation of hydrodynamic load models using cfd for the oc4-deepcwind semisubmersible. In *International Conference on Offshore Mechanics and Arctic Engineering*, volume 56574, page V009T09A037. American Society of Mechanical Engineers.

Berthelsen, P. A., Bachynski, E. E., Karimirad, M., and Thys, M. (2016). Real-time hybrid model tests of a braceless semi-submersible wind turbine: part iii—calibration of a numerical model. In *International conference on offshore mechanics and arctic engineering*, volume 49972, page V006T09A047. American Society of Mechanical Engineers.

Berthelsen, P. A., Thys, M., Kamath, A. M., Martin, T., and Bihs, H. S. (2022). Numerical simulation and comparison with experiments of a floating wind turbine using a direct forcing method. In *Trends in Renewable Energies Offshore Proceedings of the 5th International Conference on Renewable Energies Offshore*. Taylor & Francis.

Borisade, F., Koch, C., Lemmer, F., Cheng, P. W., Campagnolo, F., and Matha, D. (2018). Validation of innwind. eu scaled model tests of a semisubmersible floating wind turbine. *International Journal of Offshore and Polar Engineering*, 28(01):54–64. https://doi.org/10.17736/ijope.2018.fv04 [accessed 21 June 2024].

Burton, T., Jenkins, N., Sharpe, D., and Bossanyi, E. (2011). *Wind energy handbook*. John Wiley & Sons, second edition. https://onlinelibrary.wiley.com/doi/book/10.1002/9781119992714 [accessed 06 Feb 2023].

BVG Associates (2023). The online guide to a floating wind farm. https://bvgassociates.com/publications/ [accessed 16 Oct 2023].

BW Ideol (2018). Bw ideol's first floater in operation. https://www.bw-ideol.com/en/floatgendemonstrator [accessed 21 June 2024].

Cai, Q., Chen, D., Yang, N., and Li, W. (2024). A novel semi-spar floating wind turbine platform applied for intermediate water depth. *Sustainability*, 16(4):1663.

Canabes, J. P. G. (2010). Tmr7-experimental methods in marine hydrodynamics time series analysis.

CNBC (2023). The world's largest floating wind farm is now officially open — and helping to power north sea oil operations. https://www.cnbc.com/2023/08/23/the-worlds-largest-floating-wind-farm-is-officially-open [accessed 22 Sep 2023].

Connolly, A., Guyot, M., Le Boulluec, M., Héry, L., and O'Connor, A. (2018). Fully coupled aero-hydro-structural simulation of new floating wind turbine concept. In *International Conference on Offshore Mechanics and Arctic Engineering*, volume 51975, page V001T01A027. American Society of Mechanical Engineers.

DNV (2015). Dnv-os-e301: Position mooring.

Draycott, S., Noble, D., Davey, T., Bruce, T., Ingram, D., Johanning, L., Smith, H., Day, A., and Kaklis, P. (2018). Re-creation of site-specific multi-directional waves with non-collinear current. *Ocean Engineering*, 152:391–403.

Energy Institute (2023). Statistical review of world energy, 72nd edn. https://www.energyinst.org/__data/assets/pdf_file/0004/1055542/EI_Stat_Review_PDF_single_3.pdf [accessed 21 Sep 2023].

Esteban, M. D., Diez, J. J., López, J. S., and Negro, V. (2011). Why offshore wind energy? *Renewable Energy*, 36(2):444–450.

European Commission (2020). An EU strategy to harness the potential of offshore renewable energy for a climate neutral future. https://energy.ec.europa.eu/topics/renewable-energy/offshore-wind-and-ocean-energy_en [accessed 20 Sep 2023].

Goldwind (2023). Goldwind gwh252-16mw offshore wind turbine successfully installed. Technical report, Goldwind. https://www.goldwind.com/en/news/focus-article/?id=884026056133214208 [accessed 29 Sep 2023].

Gordon, A. L. and Cenedese, C. (2023). Ocean current. Technical report, Britannica. https://www.britannica.com/science/ocean-current [accessed 03 Oct 2023].

Hall, M., Buckham, B., and Crawford, C. (2014). Evaluating the importance of mooring line model fidelity in floating offshore wind turbine simulations. *Wind energy*, 17(12):1835–1853.

Hall, M. and Goupee, A. J. (2018). Validation of a hybrid modeling approach to floating wind turbine basin testing. *Wind Energy*, 21(6):391–408.

Henderson, A., Collu, M., and Masciola, M. (2016). Floating offshore wind energy: The next generation of wind energy, chapter overview of floating offshore wind technologies. *Springer*, 15(86):124.

IEA (2023). Iea wind tcp task 30. Technical report. https://iea-wind.org/task30/ [accessed 05 Oct 2023].

Inman, D. J. and Singh, R. C. (2007). *Engineering vibration*, volume 3. Prentice Hall Englewood Cliffs, NJ.

IRENA (2022). Renewable power generation costs in 2022. https://www.irena.org/Publications/2023/Aug/Renewable-Power-Generation-Costs-in-2022 [accessed 22 Sep 2023].

IRENA and GWEC (2023). Enabling frameworks for offshore wind scaleup: Innovations in permitting. https://www.irena.org/Publications/2021/Jul/Offshore-Renewables-An-Action-Agenda-for-Deployment [accessed 20 Sep 2023].

Ishihara, T. and Zhang, S. (2019). Prediction of dynamic response of semi-submersible floating offshore wind turbine using augmented morison's equation with frequency dependent hydrodynamic coefficients. *Renewable energy*, 131:1186–1207.

Journée, J. and Massie, W. (2001). Offshore hydromechanics. *Delft University of Technology*.

JRC (2020). Facts and figures on offshore renewable energy sources in europe.

Kawamura, S., Choe, W., Tanaka, S., and Kino, H. (1997). Development of an ultrahigh speed robot falcon using parallel wire drive systems. *Journal of the Robotics Society of Japan*, 15(1):82–89.

Kvittem, M. I., Berthelsen, P. A., Eliassen, L., and Thys, M. (2018). Calibration of hydrodynamic coefficients for a semi-submersible 10 mw wind turbine. In *International Conference on Offshore Mechanics and Arctic Engineering*, volume 51319, page V010T09A080. American Society of Mechanical Engineers.

Li, Y., Ang, K. H., and Chong, G. C. (2006). Pid control system analysis and design. *IEEE Control Systems Magazine*, 26(1):32–41.

Ma, K.-T., Luo, Y., Kwan, C.-T. T., and Wu, Y. (2019). *Mooring system engineering for offshore structures*. Gulf Professional Publishing.

Manwell, J. F., McGowan, J. G., and Rogers, A. L. (2009). *Wind Energy Explained: Theory, Design and Application*. John Wiley & Sons, second edition.

Matha, D., Schlipf, M., Pereira, R., and Jonkman, J. (2011). Challenges in simulation of aerodynamics, hydrodynamics, and mooring-line dynamics of floating offshore wind turbines. In *ISOPE International Ocean and Polar Engineering Conference*, pages ISOPE–I. ISOPE.

Mortensen, S. M., Laugesen, K., Jensen, J. K., Jessen, K., and Soltani, M. (2018). Experimental verification of the hydro-elastic model of a scaled floating offshore wind turbine. In *2018 IEEE Conference on Control Technology and Applications (CCTA)*, pages 1623–1630. IEEE. https://ieeexplore.ieee.org/abstract/document/8511565 [accessed 21 June 2024].

Mücke, T., Kleinhans, D., and Peinke, J. (2011). Atmospheric turbulence and its influence on the alternating loads on wind turbines. *Wind Energy*, 14(2):301–316. https://doi.org/10.1002/we.422 [accessed 03 Oct 2023].

Noble, D. R., Draycott, S., Sanchez, S. O., Porter, K., Johnstone, C., Finch, S., Judge, F., Desmond, C., Varela, B. S., Mendia, J. L., et al. (2018). Marinet2 d2. 1 test recommendations and gap analysis report.

Offshorewind.biz (2021). World's first floating wind farm best performer in uk | offshore wind. https://www.offshorewind.biz/2021/03/23/worlds-first-floating-wind-farm-bestperformer-in-uk/ [accessed 22 Sep 2023].

Otter, A. (2022). Combined wave, wind, and current simulation in laboratory basins with floating offshore wind turbines.

Otter, A., Flannery, B., Murphy, J., and Desmond, C. (2022a). Current simulation with software in the loop for floating offshore wind turbines. In *Journal of Physics: Conference Series*, volume 2265, page 042028. IOP Publishing.

Otter, A., Murphy, J., and Desmond, C. (2020). Emulating aerodynamic forces and moments for hybrid testing of floating wind turbine models. In *Journal of Physics: Conference Series*, volume 1618, page 032022. IOP Publishing.

Otter, A., Murphy, J., Pakrashi, V., Robertson, A., and Desmond, C. (2022b). A review of modelling techniques for floating offshore wind turbines. volume 25, pages 831–857. Wiley Online Library.

Pires, O., Azcona, J., Vittori, F., Bayati, I., Gueydon, S., Fontanella, A., Liu, Y., De Ridder, E., Belloli, M., and Van Wingerden, J. (2020). Inclusion of rotor moments in scaled wave tank test of a floating wind turbine using sil hybrid method. In *Journal of Physics: Conference Series*, volume 1618, page 032048. IOP Publishing.

Ramachandran, G., Robertson, A., Jonkman, J., and Masciola, M. D. (2013). Investigation of response amplitude operators for floating offshore wind turbines. In *ISOPE International Ocean and Polar Engineering Conference*, pages ISOPE–I. ISOPE.

Reig, M. A., Pegalajar-Jurado, A., Mendikoa, I., Petuya, V., and Bredmose, H. (2023). Accelerated second-order hydrodynamic load calculation on semi-submersible floaters. *Marine Structures*, 90:103430.

Robertson, A. N., Gueydon, S., Bachynski, E., Wang, L., Jonkman, J., Alarcon, D., Amet, E., Beardsell, A., Bonnet, P., Boudet, B., et al. (2020). Oc6 phase i: Investigating the underprediction of low-frequency hydrodynamic loads and responses of a floating wind turbine. In *Journal of Physics: Conference Series*, volume 1618, page 032033. IOP Publishing.

Ryerson, C. C. (2011). Ice protection of offshore platforms. *Cold Regions Science and Technology*, 65(1):97–110. Anti-Icing and De-Icing Techniques.

Sandner, F., Wie, Y., Matha, D., Grela, E., Azcona, J., Munduate, X., Voutsinas, S., and Natarajan, A. (2015). Innwind. eu deliverable d4. 3.3-innovative concepts for floating structures.

Sauder, T., Chabaud, V., Thys, M., Bachynski, E. E., and Sæther, L. O. (2016). Real-time hybrid model testing of a braceless semi-submersible wind turbine: Part i—the hybrid approach. In *International Conference on Offshore Mechanics and Arctic Engineering*, volume 49972, page V006T09A039. American Society of Mechanical Engineers.

Schneider Electric (2022). Lexium 28a and bch2 servo drive system, user guide. https://www.se.com/in/en/download/document/EIO0000002305/ [accessed 22 Apr 2024].

Seborg, D. E., Edgar, T. F., Mellichamp, D. A., and Doyle III, F. J. (2016). *Process dynamics and control*. John Wiley & Sons.

Shafiee, M. (2023). Failure analysis of spar buoy floating offshore wind turbine systems. *Innovative Infrastructure Solutions*, 8(1):28.

Strahler, A. H. (2008). *Modern physical geography*. John Wiley & Sons.

Subbulakshmi, A., Verma, M., Keerthana, M., Sasmal, S., Harikrishna, P., and Kapuria, S. (2022). Recent advances in experimental and numerical methods for dynamic analysis of floating offshore wind turbines—an integrated review. *Renewable and Sustainable Energy Reviews*, 164:112525.

Thys, M., Chabaud, V., Sauder, T., Eliassen, L., Sæther, L. O., and Magnussen, Ø. B. (2018). Real-time hybrid model testing of a semi-submersible 10mw floating wind turbine and advances in the test method. In *International Conference on Offshore Mechanics and Arctic Engineering*, volume 51975, page V001T01A013. American Society of Mechanical Engineers.

Thys, M., Souza, C., Sauder, T., Fonseca, N., Berthelsen, P. A., Engebretsen, E., and Haslum, H. (2021). Experimental investigation of the coupling between aero-and hydrodynamical loads on a 12 mw semi-submersible floating wind turbine. In *International Conference on Offshore Mechanics and Arctic Engineering*, volume 85192, page V009T09A030. American Society of Mechanical Engineers.

Urbán, A. M. and Guanche, R. (2019). Wind turbine aerodynamics scale-modeling for floating offshore wind platform testing. *Journal of Wind Engineering and Industrial Aerodynamics*, 186:49–57.

Vryhof, A. (2015). Vryhof manual: The guide to anchoring.

Wendt, F. F., Andersen, M. T., Robertson, A. N., and Jonkman, J. M. (2016). Verification and validation of the new dynamic mooring modules available in fast v8. In *ISOPE International Ocean and Polar Engineering Conference*, pages ISOPE–I. ISOPE.

WindFloat (2023). World's first semi-submersible floating offshore wind farm. Technical report, WindFloat Atlantic. https://www.windfloat-atlantic.com/ [accessed 03 Oct 2023].

Appendix A

MATLAB Code

```
%{
Description: This file is based on the ReadWrite sample file which demonstrates how variables on a dSPACE platform
             can be read and written from MATLAB using the dSPACE XIL API MAPort server.
             The file is adapted to be used for real-time Software in the Loop
             simulations for wind and current.

             Adapt lines 49-59 of this file according to your dSPACE platform.

             Make sure that the dSPACE platform that is used for this demo
             is registered with ControlDesk, AutomationDesk or the Platform Management API.

             Also note in the call to the method Configure of the MAPort, the second
             parameter is set to 'false'. This means that the specified simulation application
             will not be downloaded unless there is no application loaded on the platform.
             If the specified application is already running, no further action will be taken.
             If any other application is running on the platform, an exception will be thrown.

Tip/Remarks: Objects of some XIL API types (e.g., MAPort, Capture) must be disposed at the end
             of the function. We strongly recommend to use exception handling for this purpose
             to make sure that Dispose is called even in the case of an error.

Version:     3.0

Date:        November 2018

             dSPACE GmbH shall not be liable for errors contained herein or
             direct, indirect, special, incidental, or consequential damages
             in connection with the furnishing, performance, or use of this
             file.
             Brand names or product names are trademarks or registered
             trademarks of their respective companies or organizations.

Copyright 2018, dSPACE GmbH. All rights reserved.

Adapted for use by Cillian Frawley for a Research Masters SIL project, March 2024.
%}

NET.addAssembly('ASAM.XIL.Interfaces, Version=2.1.0.0, Culture=neutral, PublicKeyToken=bf471dff114ae984');
NET.addAssembly(['ASAM.XIL.Implementation.TestbenchFactory, Version=2.1.0.0, Culture=neutral,...' ...
    ' PublicKeyToken=fc9d65855b27d387']);

import ASAM.XIL.Implementation.TestbenchFactory.Testbench.*;
import ASAM.XIL.Interfaces.Testbench.*;
import ASAM.XIL.Interfaces.Testbench.Common.Error.*;
import ASAM.XIL.Interfaces.Testbench.Common.ValueContainer.*;
import ASAM.XIL.Interfaces.Testbench.MAPort.*;
import ASAM.XIL.Interfaces.Testbench.MAPort.Enum.*;

% The following lines must be adapted to the dSPACE platform used
%--------------------------------------------------------------------------------------------------
% Set IsMPApplication to true if you are using a multiprocessor platform
isMPApplication = false;
% Use an MAPort configuration file that is suitable for your platform and simulation application
% See the folder Common\PortConfigurations for some predefined configuration files
maPortConfigFile = ['C:\Users\QTM\Documents\dSPACE\XIL API .NET\2021-A\MAPort\Common\PortConfigurations...' ...
    '\MAPortConfigDS1104_cillian_current_singlewinch.xml'];

% Set the name of the task here (specified in the application's TRC file)
% Note: the default task name is "HostService" for PHS bus systems, "Periodic Task 1" for VEOS
task = 'HostService';
%--------------------------------------------------------------------------------------------------

```

```
masterTaskPrefix = '';
slaveTaskPrefix = '';
masterVariablesPrefix = 'Model Root/';
slaveVariablesPrefix = 'Model Root/';

try
    %-----------------------------------------------------------------------------------------------
    % Create a TestbenchFactory object; the TestbenchFactory is needed to
    % create the vendor-specific Testbench
    %-----------------------------------------------------------------------------------------------
    myTestbenchFactory = TestbenchFactory();

    %-----------------------------------------------------------------------------------------------
    % Create a dSPACE Testbench object; the Testbench object is the central object to access
    % factory objects for the creation of all kinds of Testbench-specific objects
    %-----------------------------------------------------------------------------------------------
    myTestbench = myTestbenchFactory.CreateVendorSpecificTestbench('dSPACE GmbH', 'XIL API', '2021-A');

    %-----------------------------------------------------------------------------------------------
    % We need an MAPortFactory to create an MAPort and also a ValueFactory to create ValueContainer
    % objects
    %-----------------------------------------------------------------------------------------------
    myMAPortFactory = myTestbench.MAPortFactory;
    myValueFactory = myTestbench.ValueFactory;

    %-----------------------------------------------------------------------------------------------
    % For multiprocessor platforms different tasknames and variable names have to be used.
    % Some variables are part of the subappliaction "masterAppl", some belong to the
    % subapplication "slaveAppl"
    %-----------------------------------------------------------------------------------------------
    if (isMPApplication)
        masterTaskPrefix = 'masterAppl/';
        slaveTaskPrefix = 'slaveAppl/';
        masterVariablesPrefix = 'masterappl/Model Root/master/CentralLightEcu/';
        slaveVariablesPrefix = 'slaveappl/Model Root/slave/FrontRearLightEcu/';
    end

    masterTask = [masterTaskPrefix, task];
    slaveTask = [slaveTaskPrefix, task];

    %-----------------------------------------------------------------------------------------------
    % Create and configure an MAPort object and start the simulation
    %-----------------------------------------------------------------------------------------------
    fprintf('Creating MAPort...\n');
    % Create an MAPort object using the MAPortFactory
    demoMAPort = myMAPortFactory.CreateMAPort('DemoMAPort');
    fprintf('...done\n');
    % Load the MAPort configuration
    maPortConfig = demoMAPort.LoadConfiguration(maPortConfigFile);
    % Apply the MAPort configuration
    fprintf('Configuring MAPort...\n');
    demoMAPort.Configure(maPortConfig, false);
    fprintf('...done\n');
    if (demoMAPort.State ~= MAPortState.eSIMULATION_RUNNING)
        % Start the simulation
        fprintf('Starting simulation...\n');
        demoMAPort.StartSimulation();
        fprintf('...done\n');
    end

    % Create variables for the simulation
    u = [masterVariablesPrefix, 'u/Value']; % platform surge
    U = [masterVariablesPrefix, 'U/Value']; % current velocity
    %pitch = [masterVariablesPrefix, 'pitch/Value']; % platform pitch
    %V_wind = [masterVariablesPrefix, 'V_wind/Value']; % wind speed (fullscale)
    %load 'windspeed.mat' % Wind speed file
```

```
   % V=V(1:10:end);
    %load 'current_ts.mat'
   % n=numel(V);
   % n=numel(cs);
     n=7400;

    QCM('connect','192.168.254.1','frameinfo','6D') % QCM is a MATLAB plugin
    % for Qualisys Track Manager, it connects to the Qualisys host computer and
    % streams motion tracking data in real-time to MATLAB
    the3dlabels=QCM('3dlabels');
    the6dlabels=QCM('6doflabels');
    [frameinfo, trajectories] = QCM;

    X = zeros(1,n);
    Qualisys_u_out = zeros(1,n);
    %RY = zeros (1,n);

    x_s=trajectories(1,1)/1000;
    %ry_s=trajectories(1,5);

    X(1,1)=x_s;
    %RY(1,1)=ry_s;
    % Loop to update motion tracking for each time-step, it uses surge motion
    % of the tracked object to calculate its velocity "u", and pitch motion
    % for angular velocity "ry". "V" is the wind speed at hub height of the turbine (at full scale)
    for i=2:n

        [frameinfo, trajectories] = QCM;
%         v=cs(i) % current velocity from time series
        X(i)=trajectories(1,1)/1000;
        uc=(X(i)-X(i-1))./0.03125; % surge velocity
        %RY(i)=trajectories(1,5);
       % ry=(RY(i)-RY(i-1))./0.03125 % pitch velocity

        %dc1=V(i) % wind speed at hub height
        pause((1/3.5)/sqrt(50))



    %--------------------------------------------------------------------------
    % Read and Write the value of the variables
    %--------------------------------------------------------------------------

     demoMAPort.Write(u,  myValueFactory.CreateFloatValue(uc));
%    demoMAPort.Write(U,  myValueFactory.CreateFloatValue(v));
   % demoMAPort.Write(pitch,  myValueFactory.CreateFloatValue(ry));
   % demoMAPort.Write(V_wind,  myValueFactory.CreateFloatValue(dc1));

    end
    % to stop winch and propellers at end of simulation
    demoMAPort.Write(u,  myValueFactory.CreateFloatValue(0));
    %demoMAPort.Write(pitch,  myValueFactory.CreateFloatValue(0));
    %demoMAPort.Write(V_wind,  myValueFactory.CreateFloatValue(0));
%     demoMAPort.Write(U,  myValueFactory.CreateFloatValue(0));

    fprintf('\nDemo successfully finished!\n');

    %--------------------------------------------------------------------------
    % Attention: make sure to dispose the MAPort object in any case to free system resources like
    % allocated memory and also resources and services on the platform, and
    % disconnect from QTM to prevent MATLAB from crashing.
    %--------------------------------------------------------------------------
    demoMAPort.Dispose();
    QCM('disconnect')
catch e
    if (exist('demoMAPort', 'var'))
```

```
195                 % make sure to dispose the MAPort object in case of an error
196         demoMAPort.Dispose();
197     end
198 
199     if (isa(e, 'NET.NetException'))
200         if (isa(e.ExceptionObject, 'ASAM.XIL.Interfaces.Testbench.Common.Error.TestbenchPortException'))
201             %-----------------------------------------------------------------------------------------------
202             % Display the XIL API exception information to get the cause of an error
203             %-----------------------------------------------------------------------------------------------
204             fprintf('XIL API exception occurred:\n');
205             fprintf('Code: %d\n', e.ExceptionObject.Code);
206             fprintf('CodeDescription: %s\n', char(e.ExceptionObject.CodeDescription));
207             fprintf('VendorCode: %d\n', e.ExceptionObject.VendorCode);
208             fprintf('VendorCodeDescription: %s\n', char(e.ExceptionObject.VendorCodeDescription));
209         else
210             fprintf('.NET exception occurredd:\n');
211             fprintf('Message: %s\n', char(e.message));
212         end
213     end
214     rethrow(e);
215 end
```

Appendix B

LabVIEW Code

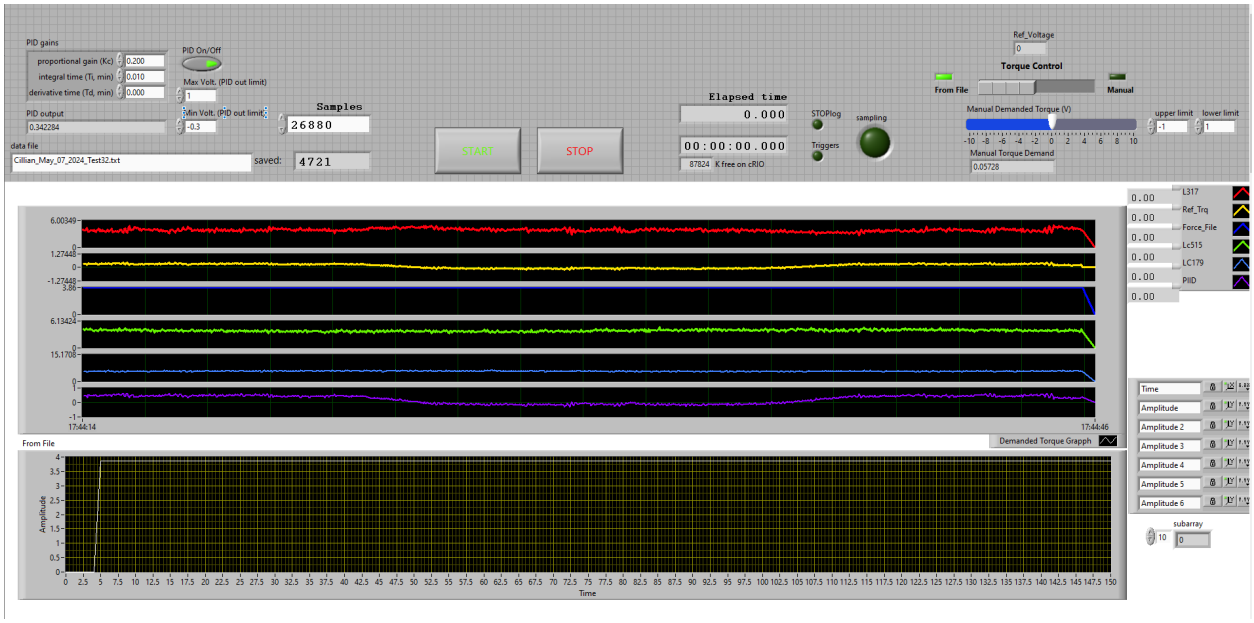


Figure B.1: GUI for the LabVIEW code.

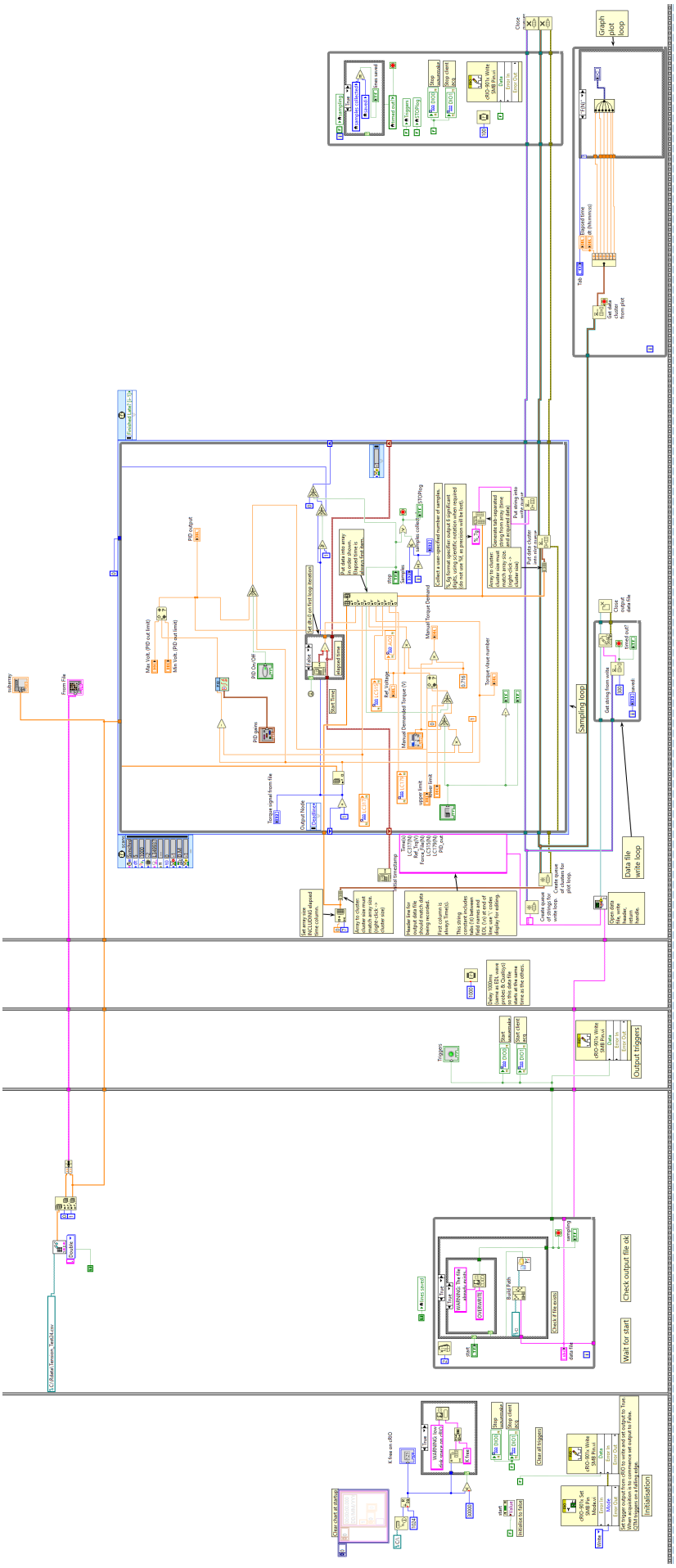


Figure B.2: LabVIEW code for TSIL single winch system.